EXPERIMENTAL AND THEORETICAL STUDY OF QUARTZ AND InP PIEZOELECTRIC MEMS RESONATORS

EXPERIMENTAL AND THEORETICAL STUDY OF QUARTZ AND InP PIEZOELECTRIC MEMS RESONATORS

By

ABHISHAIK RAMPAL, B.ENG.

B.Eng.(McMaster University) 2004

A Thesis

Submitted to the School of Graduate Studies in

Partial Fulfilment of the Requirements

for the Degree Masters of Applied Science

McMaster University

MASTER OF APPLIED SCIENCE (2010) McMaster University
(Engineering Physics) Hamilton, Ontario

TITLE: Experimental and theoretical study of quartz and InP piezoelectric MEMS resonators
AUTHOR: Abhishaik Rampal
SUPERVISOR: Dr. R. N. Kleiman
NUMBER OF PAGES: x, 103

Abstract

MEMS resonators, cantilevers and bridges, using the piezoelectric effect to drive and detect the fundamental resonance mode are studied. Two types of MEMS resonators are investigated in detail: a conventional quartz tuning fork (a two terminal device) and an InP bridge (a three terminal device). While the former is fabricated commercially from an insulating piezoelectric material the latter is fabricated via the controlled growth of a III-V semiconductor material with a non-zero piezoelectric coefficient. To utilize piezoelectricity based on a III-V semiconductor, an $In_{0.85}Ga_{0.15}P/InP$ heterojunction was fabricated resulting in a depletion width which can be controlled using Schottky contacts. The result of this design is a piezoelectric device, in principle allowing for (dc) tuning of the magnitude of the resonant (ac) deflection and current. The type of deformation of interest is flexural and based on this a general theory relating the bending moment produced due to the piezoelectric stress is presented. Using this bending moment a general expression for the expected deflection and charge is derived analytically. For the quartz case the general expression, which has not been previously derived, is compared to the results of experiments and finite element simulations with good agreement. For the case of InP devices a resonance was not detected. This is attributed to the small piezoelectric coefficient of InP, the stiff bridge design that was chosen and large parasitic effects combining to make it difficult to observe the resonance. The fundamental mechanical noise of the quartz tuning fork was measured and is due to thermal fluctuations at the measurement temperature (~300K) associated with the dissipation in the mechanical system and can be related to the effective resistance of the resonator in the equivalent electrical circuit. Additionally, contributions to the package or dielectric capacitance using two and three terminal setups were studied. The three terminal configuration results in a lower package or dielectric capacitance than for the two terminal configuration.

Acknowledgements

There are several people who have been influential throughout my work on this project. I would like to thank, first and foremost, Dr. Rafael N. Kleiman, my supervisor, who has not only provided the resources to make this research possible but has also provided helpful guidance and insightful ideas to further this work. I am very appreciative of the staff of Center for Emerging Device Technology (CEDT) - Dr. Brad J. Robinson, Dr. Doug Bruce, Dr. Zhilin Peng and Doris V. Stevanovic for their patience while training me and for their thoughts and feedback on barriers which arose throughout this research. Thank you to my committee members, Dr. Paul. E. Jessop and Dr. Andy. P. Knights, for agreeing to be a part of this project. Last but definitely not least thanks to my parents and twin sister for their constant support, motivation and being the foundation on which I can be me.

Contents

List of Figures

List of Tables

Chapter 1

Introduction

1.1 MEMS

Micro-Electro Mechanical Systems (MEMS), as the name suggests, are devices in the micron scale using either electricity or electronics (or both) and having some kind of moving part or parts. The MEMS concept, however, has grown to encompass many other types of domains like thermal, magnetic, fluidic and optical devices, with or without moving parts [1]. In practice, MEMS share several common features:

1. MEMS are both the sensors and actuator part of the system. As sensors, they gather information from the environment through measuring mechanical, thermal, biological, chemical, optical and magnetic phenomena. The "brain" which could be electronics, chemistry, optics etc processes this information and direct the actuators to respond by moving, positioning etc thereby interacting with the environment for some desired outcome or purpose

2. MEMS are "systems", in that system issues like packaging, system partitioning into components, calibration, signal to noise ratio, stability and reliability all need to be addressed

3. MEMS devices involve paradigm shifts from macro ways of doing things, by more than simply reducing the size scale. For examples ink-jet heads allow high-quality color printing at very low cost, Digital Micromirror Device (DMD) found in digital projectors allow for light weight home and business projection application, inertial sensors allow for reliable sensing thereby triggering airbag release only when needed

1.2 Material for MEMS Fabrication

Conventional MEMS devices are fabricated from silicon, silicon dioxide, silicon nitride, poly-silicon etc.

Silicon is used because: it is abundant, inexpensive and can be produced and processed controllably with repetitive standard of high purity and perfection, thin films like silicon dioxide, silicon nitride, poly-silicon can be deposited, patterned, etched which are highly amenable to miniaturization and most importantly batch fabrication techniques akin to the those used in integrated circuit (IC) industry can be used. This last point allows for silicon based MEMS to be made cheaply and integrate the sensory/actuation component with the electronic circuitry or "brain". Additionally, silicon's young modulus [2], 1.9×10^{11} Pa, is comparable to steel [2], 2.1×10^{11}Pa, and has a tensile yield strength [2], 6.0×10^{9} Pa, which is three times higher than steel making it a good mechanical material. The ability to grow high purity crystals allows for fabrication of extremely high Q resonators thereby increasing sensitivity of resonator applications. Silicon, however, does have

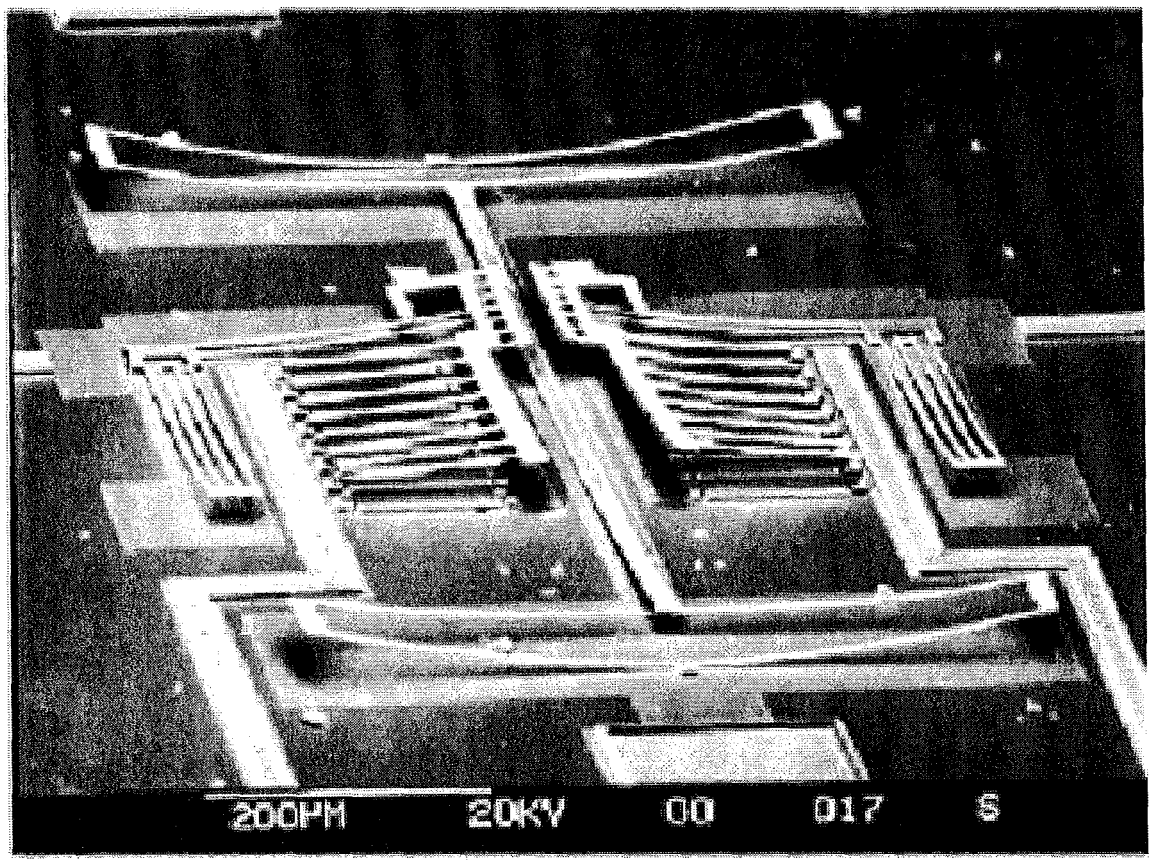

Figure 1.1: Silicon strained MEMS resonator[3]

disadvantages mainly lack of piezoelectricity, no band gap engineering capability and is optically inactive due to its indirect band gap property. Additionally, the films grown on silicon can induce high strain causing unwanted effects like shape distortions, figure 1.1 [3], in mechanical structures.

III-Vs not only share similar advantages to silicon, like comparable young's modulus, availability of high purity crystal etc, but have additional properties like being optically and piezoelectrically active making it a favorable material for various sensor based applications. III-Vs also have the unique property of forming compatible ternary and quaternary compounds by alloying which allows for variable optical and piezoelectric properties. Additionally, using lattice matched techniques the ternary and quaternary alloys can be grown on III-V substrates, using epitaxial techniques like MOCVD and MBE, without causing too much strain. This has the advantage that mechanical structures, after fabrication, do not have unwanted shape distortions. Various micromachining techniques such as: selective etch stops for heterostructures and homostructures, sacrificial layer techniques, high yield strength solid state bonding and dry and wet etching for isotropic and anisotropic shaping have been developed. III-Vs, however, does have disadvantages mainly: high manufacturing costs, relatively new MEMS technology and most importantly lack of availability of insulating high-quality oxides and nitrides for reproducible and protective passivating layers. Therefore the powerful MOS technology in silicon has no counterpart in III-V technology.

1.3 Piezoelectric Effect

Piezoelectricity was discovered by brothers Pierre and Jacques Curie in 1880 [4]. However, this did not happen randomly. In India and Ceylon the mysterious behavior of tourmalins was well-known. It was noticed if tourmalins were put into hot ash, at one side they attracted ash particles while at the opposite side they were rejected. After some time the effect of attraction and rejection inverted. At the beginning of the 18th century traders brought the tourmalin crystals to Europe. In 1747, Linne called the tourmalin crystals lapis electricus [5]. In the following century, researchers attempted to find a connection between the mechanical pressure effect and the electricity. Becquerel was aware of the fact, that such an effect could be expected with crystals. In 1877, Lord Kelvin established the correlation between pyroelectricity and piezoelectricity [5]. It was verified that the pyroelectric charge of the tourmalin is ascribed to the formation of piezoelectric surface charge caused by the elastic crystal deformation under temperature changes. The brothers Pierre and Jacques Curie discovered the direct piezoelectric effect in tourmalin crystals. They recognized that a mechanical deformation in certain directions causes opposite electrical surface charges at opposite crystal faces being proportional to the mechanical deformation. This effect, also found in quartz and other crystals without symmetry center, has been called piezoelectric effect (Greek: piezein = press) [5]. The inverse piezoelectric effect predicted by Lippmann [6] based on thermodynamic considerations were confirmed experimentally by the Curie brothers.

Common naturally occurring piezoelectric materials are α-quartz, bone, silk, dentin etc. Man-made piezoelectric materials include Gallium Orthophosphate, Langasite, ceramics such as: Barrium Titanate ($BaTiO_3$), Lead Titanate ($PbTiO_3$), Lead Ziconate Titanate (PZT) etc. A common property all these materials, than piezoelectricity, is their high resistivities; ranging from $1.0 \times 10^9 - 1.0 \times 10^{16} \Omega$-cm. Infact, having high resistivity is almost a requirement for detectable piezoelectricity. Application of piezoelectricity in MEMS range from micro-pumps for biomedical applications, energy harvesting through motion, switches used in RF applications, gyroscopes etc.

1.4 Thesis Overview

In this work MEMS resonators are of interest and piezoelectricity is used to drive and detect this resonance. The thesis is separated into two parts: the first part is concerned with the design, theoretical and experimental results of a conventional quartz resonator – quartz tuning fork, and the second part is concerned with design, fabrication, theoretical and experimental results of an InP resonator. In both these materials the piezoelectric effect is harnessed.

Chapter 2

Theory

The theoretical concepts common to both quartz and InP piezoelectric resonators is presented. The concepts are: structural, piezoelectric, electrical resonant circuit and quality factor.

2.1 Structural

There are various ways by which an object can deform – longitudinal, flexural, thickness shear, face shear as depicted in figure 2.1 [7]. For beams, beams is defined as structures whose thickness has the smallest dimension, width is at least ten times larger and length is at least hundred times larger, the dominant types of deformation are longitudinal and flexural. In this research work the focus is on driving and detecting flexural vibrations of cantilevers and bridges.

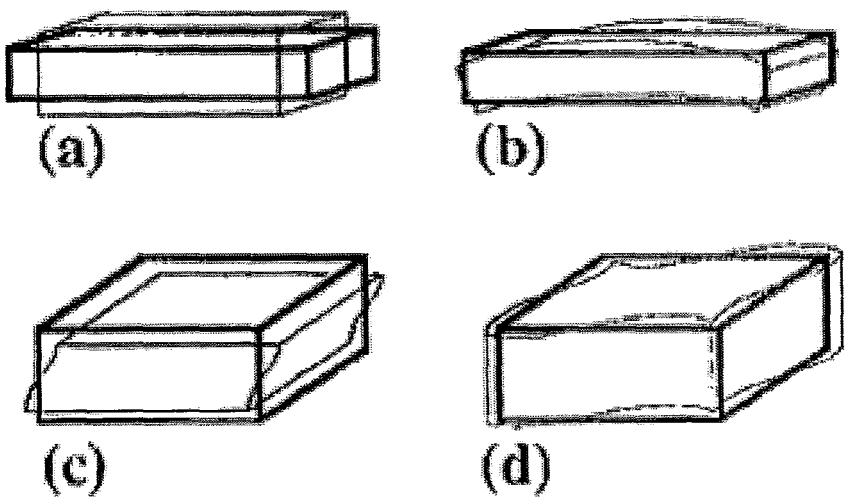

Figure 2.1: Types of deformation: (a) longitudinal, (b) flexural, (c) thickness shear and (d) face shear[7]

2.1.1 Flexural Bending

For the simplistic case of a member in pure bending subjected to equal and opposite bending moments the internal forces in any cross section of a member is equivalent to the applied moment as illustrated in figure ?? [8]. In order to calculate the deformation of the beam the strain, or equivalently the stress, due to a couple must be determined. Using the methods of statics relations are derived which satisfy the stresses exerted on any cross-section of a prismatic member in pure bending. Denoting σ_x the normal stress, due to a normal force, at a given point of the cross section, τ_{xy} and τ_{xz} the components of the shearing stress, an expression is derived showing the system of the elementary internal forces exerted on the section is equivalent to the couple M, figure 2.3 [8]. From statics a couple, M, consists of two equal and opposite forces. The sum of the components of these forces in any direction is therefore equal to zero. Additionally, the moment of the couple is the same about any axis perpendicular to its plane, and is zero about any axis contained in that plane. Selecting arbitrarily the *z-axis*, figure 2.3 [8] equations (2.1)-(2.3) expressing the equivalence of the elementary internal forces and of the couple M by writing that the sums of the components and of the moments of the elementary forces are equal to the corresponding components and moment of the couple M (ignoring the shearing stress):

$$x - components : \int \sigma_x dA = 0 \tag{2.1}$$

$$moment\ about\ y\ axis : \int z\sigma_x dA = 0 \tag{2.2}$$

$$moment\ about\ z\ axis : \int -y\sigma_x dA = M \tag{2.3}$$

The minus sign in equation (2.3) is due to the fact that a tensile stress leads to a negative moment of the normal forces $\sigma_x dA$ about the *z axis*. Equation (2.2) is trivial if the prismatic member is symmetric with respect to the plane containing the couple M, and if the y-axis is chosen in that plane.The distribution of the normal forces on the section will be symmetric about the y-axis.

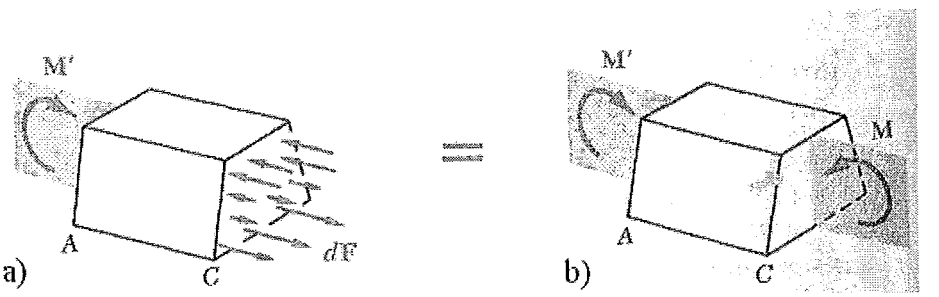

Figure 2.2: Member subjected to equal and opposite couples: (a)internal force at a cross-section, (b)equal and opposite couples[8]

To determine the deflection of a beam the following is required: (a) relationship between the deflection of the beam and moment, (b) the mode shapes of the beam and (c) the principle of virtual work equated to the strain energy.

Equation (2.4) [8] is a 2^{nd} order differential equation where $\xi\,(y)$ is the deflection along y-axis and I, Y is the inertia and Young's modulus of the beam.

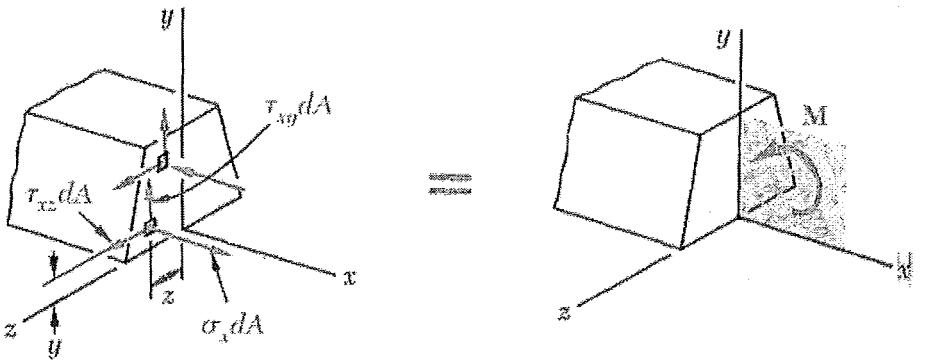

Figure 2.3: Normal and shearing stress in a prismatic member due to a couple[8]

$$\frac{d^2\xi(y)}{dy^2} = \frac{M(y)}{YI} \tag{2.4}$$

Equation (2.5) [9] is the general equation for the modes of a prismatic member. The constants C_1, C_2, C_3 and C_4 are solved for various boundary conditions distinguishing between the cantilever and bridge case.

$$\begin{aligned} X_i &= C_1(cos(k_i y) + cosh(k_i y)) + C_2(cos(k_i y) - cosh(k_i y)) \\ &\quad + C_3(sin(k_i y) + sinh(k_i y)) + C_4(sin(k_i y) - sinh(k_i y)) \end{aligned} \tag{2.5}$$

The virtual work, equation (2.6) [9], is defined in terms of internal moment, M, and virtual slope, $\delta\phi$. Using the definition of virtual displacement, $\delta\xi(y)$, and virtual slope the relationship between the two is $\delta\phi = \frac{\partial(\delta\xi(y))}{\partial y}$. Therefore, virtual work in terms of deflection is equation (2.7).

$$\delta W = M\delta\phi \tag{2.6}$$

$$\delta W = M\frac{\partial(\delta\xi(y))}{\partial y} \tag{2.7}$$

Strain Energy of a beam, equation (2.8) [9], is expressed in terms of an initial deflection, v_o, where the initial deflection is a combination of the mode shapes of a prismatic member, equation (2.9) [9]. Here X_i is the normal functions pertaining to the mode shapes equation (2.5) and b_i is the constant scale factor, i.e. contribution from each mode, to be determined. Combining the two, the strain energy within a prismatic member in the deflected position is equation (2.10).

$$U_o = \frac{YI}{2}\int\left(v_o''\right)^2 dy \tag{2.8}$$

$$v_o = \xi(y) = b_1X_1 + b_2X_2 + b_3X_3 + ... = \sum b_iX_i \tag{2.9}$$

$$U_o = \frac{YI}{2}\sum b_i^2\int\left(X_i''\right)^2 dy$$

$$U_o = \frac{YI}{2} \sum b_i^2 k_i^4 \int (X_i)^2 \, dy \tag{2.10}$$

Similarly virtual work can be expressed in terms of equation (2.9) yielding equation (2.11). Setting virtual work equation (2.11) equal to the incremental strain energy equation (2.10) yields equation (2.12) for deflection. This equation consists of two terms: constant which is proportional to the moment and summation which is the product of the mode shape and its derivative or curvature evaluated at some $y = y_1$ independent of the evaluation of $\xi(y)$. The two types of prismatic members solved are cantilevers and bridges.

$$\frac{\partial(\delta\xi(y))}{\partial y} = \frac{\partial(v_o)}{\partial y} = \frac{\partial(\delta b_i X_i)}{\partial y} = \frac{\delta b_i \partial X_i}{\partial y}$$

$$W = M \frac{\delta b_i \partial X_i}{\partial y} \tag{2.11}$$

$$M \delta b_i \frac{\partial X_i}{\partial y} = \frac{\partial U_o \delta b_i}{\partial b_i}$$

$$M \delta b_i \frac{\partial X_i}{\partial y} = \frac{\partial U_o \delta b_i}{\partial b_i} = \frac{\partial \left(\frac{YI}{2} \sum b_i^2 k_i^4 \int (X_i)^2 \, dy \right) \delta b_i}{\partial b_i}$$

$$M \frac{\partial X_i}{\partial y} = YI \sum b_i k_i^4 \int (X_i)^2 \, dy$$

$$b_i = \frac{M}{YI \sum k_i^4 \int (X_i)^2 \, dy} \left(\frac{\partial X_i}{\partial y} \right)$$

$$\xi(y) = \sum b_i X_i = \frac{M}{YI} \sum \frac{X_i}{k_i^4 \int (X_i)^2 \, dy} \left(\frac{\partial X_i}{\partial y} \right)$$

$$\xi(y) = \frac{M}{YI} \sum \frac{X_i}{k_i^4 L} \left(\frac{\partial X_i}{\partial y} \right)$$

$$\xi(y) = \frac{ML^3}{YI} \sum \frac{X_i}{(k_i L)^4} \left(\frac{\partial X_i}{\partial y} \right)_{y=y_1} \tag{2.12}$$

2.1.1.1 Cantilevers

The mode shapes of a cantilever are determined using equation (2.5) for the appropriate boundary conditions equation (2.13)-(2.16)[9]. These boundary conditions describe the deformation and strain at $y = 0$ is zero, curvature and shear force at $y = L$ are also zero. The first two conditions yield, $C_1 = 0$ and $C_3 = 0$, reducing equation (2.5) to equation (2.17).

$$X_{y=0} = 0 \tag{2.13}$$

$$\left(\frac{dX}{dy}\right)_{y=0} = 0 \tag{2.14}$$

$$\left(\frac{d^2X}{dy^2}\right)_{y=L} = 0 \tag{2.15}$$

$$\left(\frac{d^3X}{dy^3}\right)_{y=L} = 0 \tag{2.16}$$

$$X_i = C_2\left(cos\left(k_i y\right) - cosh\left(k_i y\right)\right) + C_4\left(sin\left(k_i y\right) - sinh\left(k_i y\right)\right) \tag{2.17}$$

Applying the third and fourth condition yields:

$$C_2\left(cos\left(k_i L\right) + cosh\left(k_i L\right)\right) + C_4\left(sin\left(k_i L\right) + sinh\left(k_i L\right)\right) = 0$$

$$C_2\left(sin\left(k_i L\right) - sinh\left(k_i L\right)\right) - C_4\left(cos\left(k_i L\right) + cosh\left(k_i L\right)\right) = 0$$

The resonance frequencies, equation (2.19)[9], are determined by taking the determinant of the above equations yielding a transcendental equation, equation (2.18). The first ten roots of this equation are given in table (2.1). Additionally, solving for the constants C_2 & C_4 results in the general equation describing the mode shapes of a cantilever, equation (2.20). The mode shapes associated with first three roots are given in figure (2.4).

$$cosh\left(k_i L\right) cos\left(k_i L\right) = -1 \tag{2.18}$$

$$f_r = \frac{1}{2\pi}\left(k_i L\right)^2 \frac{t}{L^2}\sqrt{\frac{Y}{12\rho}} \tag{2.19}$$

$$X_i = \left(cos\left(k_i y\right) - cosh\left(k_i y\right) - \alpha_i\left(sin\left(k_i y\right) - sinh\left(k_i y\right)\right)\right) \tag{2.20}$$

where

$$\alpha_i = \frac{cosh\left(k_i L\right) + cos\left(k_i L\right)}{sinh\left(k_i L\right) + sin\left(k_i L\right)}$$

Using equations (2.20) and (2.12) equation (2.21) is the general expression for the deflection of a cantilever beam. The maximum deflection for the fundamental mode occurs at $y = L$. This is solved using equations (2.12) and (2.20) yielding equation (2.22) as shown below:

$$\xi\left(y\right) = \frac{ML^3}{YI}\sum \frac{X_i}{\left(k_i L\right)^4}\left(\frac{\partial X_i}{\partial y}\right)_{y=y_1}$$

$$\frac{\partial X_i}{\partial y} = \frac{\partial\left(cos\left(k_i y\right) - cosh\left(k_i y\right) - \alpha_i\left(sin\left(k_i y\right) - sinh\left(k_i y\right)\right)\right)}{\partial y}$$

i	k_iL
1	1.875104069
2	4.69409133
3	7.85475748
4	10.99554073
5	14.13716839
6	17.27875953
7	20.42035225
8	23.56194490
9	26.70353756
10	29.84513021

Table 2.1: Roots of equation(2.18)

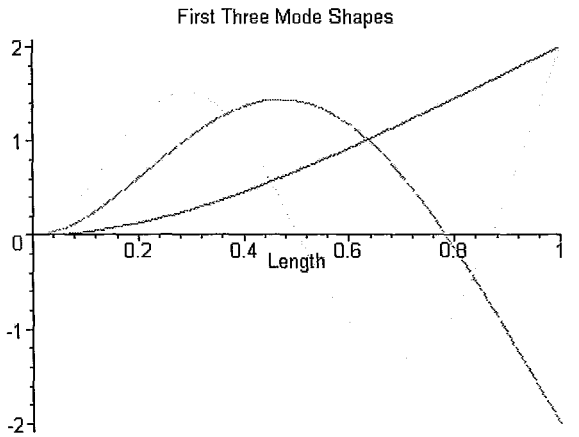

Figure 2.4: Cantilever's first three modes

$$\frac{\partial X_i}{\partial y} = k_i \left(-sin\left(k_i y\right) - sinh\left(k_i y\right) - \alpha_i \left(cos\left(k_i y\right) - cosh\left(k_i y\right)\right)\right)$$

$$\xi\left(y\right) = \frac{ML^3}{YI} \sum \frac{X_i}{\left(k_i L\right)^4} k_i \left(-sin\left(k_i y_1\right) - sinh\left(k_i y_1\right) - \alpha_i \left(cos\left(k_i y_1\right) - cosh\left(k_i y_1\right)\right)\right)$$

$$\xi\left(y\right) = \frac{ML^2}{YI} \sum \frac{X_i}{\left(k_i L\right)^4} \left(k_i L\right) \left(-sin\left(k_i y_1\right) - sinh\left(k_i y_1\right) - \alpha_i \left(cos\left(k_i y_1\right) - cosh\left(k_i y_1\right)\right)\right)$$

$$\xi\left(y\right) = \frac{ML^2}{YI} \sum \frac{X_i}{\left(k_i L\right)^3} \left(-sin\left(k_i y_1\right) - sinh\left(k_i y_1\right) - \alpha_i \left(cos\left(k_i y_1\right) - cosh\left(k_i y_1\right)\right)\right)$$

$$\begin{aligned} \xi\left(y\right) \quad = \quad & \frac{ML^2}{YI} \sum_{i=1}^{\infty} \left[\frac{\left(cos\left(k_i y\right) - cosh\left(k_i y\right) - \alpha_i \left(sin\left(k_i y\right) - sinh\left(k_i y\right)\right)\right)}{\left(k_i L\right)^3} \right. \\ & \left. \frac{\left(-sin\left(k_i y_1\right) - sinh\left(k_i y_1\right) - \alpha_i \left(cos\left(k_i y_1\right) - cosh\left(k_i y_1\right)\right)\right)}{\left(k_i L\right)^3} \right] \end{aligned} \tag{2.21}$$

$$\xi\left(L\right) = \frac{ML^2}{YI} \sum_{i=1}^{\infty} \frac{4}{\left(k_i L\right)^3} \left(\frac{sin\left(k_i L\right) sinh\left(k_i L\right)}{\left(sinh\left(k_i L\right) + sin\left(k_i L\right)\right)^2} \left[sin\left(k_i L\right) cosh\left(k_i L\right) - sinh\left(k_i L\right) cos\left(k_i L\right)\right] \right) \tag{2.22}$$

2.1.1.2 Bridge

Following the same process as for the cantilever, the appropriate boundary conditions for the bridge are equations (2.23)-(2.26)[9]. These boundary conditions describe the deformation and strain at $y = 0$ and $y = L$ is zero. The first two conditions yield, $C_1 = 0$ and $C_3 = 0$, reducing equation (2.5) to equation (2.27).

$$X_{y=0} = 0 \tag{2.23}$$

$$\left(\frac{dX}{dy}\right)_{y=0} = 0 \tag{2.24}$$

$$X_{y=L} = 0 \tag{2.25}$$

$$\left(\frac{dX}{dy}\right)_{y=L} = 0 \tag{2.26}$$

$$X_i = C_2 \left(cos\left(k_i y\right) - cosh\left(k_i y\right)\right) + C_4 \left(sin\left(k_i y\right) - sinh\left(k_i y\right)\right) \tag{2.27}$$

Applying the third and fourth condition yield:

$$C_2 \left(cos\left(k_i L\right) - cosh\left(k_i L\right)\right) + C_4 \left(sin\left(k_i L\right) - sinh\left(k_i L\right)\right) = 0$$

i	k_iL
1	4.730040745
2	7.853204624
3	10.99560784
4	14.13716549
5	17.27875966
6	20.42035225
7	23.56194490
8	26.70353756
9	29.84513021
10	32.98672286

Table 2.2: Roots of equation (2.28)

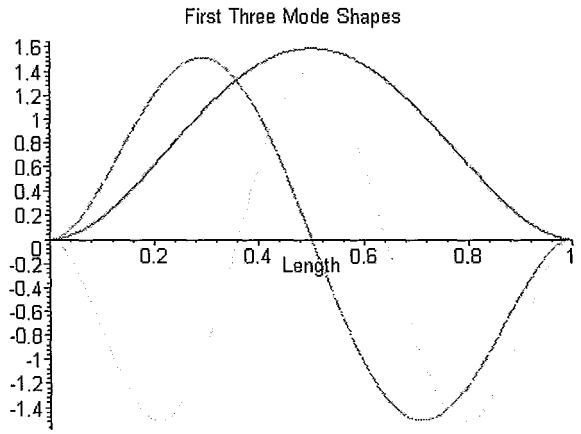

Figure 2.5: Bridge's first three modes

$$C_2\left(sin\left(k_iL\right)+sinh\left(k_iL\right)\right)-C_4\left(-cos\left(k_iL\right)+cosh\left(k_iL\right)\right)=0$$

The resonance frequencies, equation (2.19), are determined by taking the determinant of the above equations yielding a transcendental equation equation (2.28). The first ten roots are given in table (2.2). Additionally, solving for the constants C_2 & C_4 results in the general equation describing the mode shapes of a bridge, equation (2.29). The mode shapes associated with first three roots are given in figure (2.5).

$$cosh\left(k_iL\right)cos\left(k_iL\right)=1 \tag{2.28}$$

$$X_i=\left(cosh\left(k_iy\right)-cos\left(k_iy\right)-\alpha_i\left(sinh\left(k_iy\right)-sin\left(k_iy\right)\right)\right) \tag{2.29}$$

where

$$\alpha_i=\frac{cosh\left(k_iL\right)-cos\left(k_iL\right)}{sinh\left(k_iL\right)-sin\left(k_iL\right)}$$

Using equations (2.12) and (2.29) equation (2.30) is the general expression for the deflection of a bridge. For the fundamental mode maximum deflection, equation (2.31), occurs at $y=L/2$ where the slope term is evaluated at $y_1=L/4$, i.e. at maximum curvature or maximum strain.

$$\xi(y) = \frac{ML^2}{YI}\sum_{i=1}^{\infty}\left[\frac{(cosh(k_iy) - cos(k_iy) - \alpha_i(sinh(k_iy) - sin(k_iy)))}{(k_iL)^3}\right.$$
$$\left.\frac{(sinh(k_iy_1) + sin(k_iy_1) - \alpha_i(cosh(k_iy_1) - cos(k_iy_1)))}{(k_iL)^3}\right] \quad (2.30)$$

$$\xi\left(\frac{L}{2}\right) = \frac{ML^2}{YI}\sum_{i=1}^{\infty}\frac{\left[\left(cosh\left(\frac{k_iL}{2}\right) - cos\left(\frac{k_iL}{2}\right) - \alpha_i\left(sinh\left(\frac{k_iL}{2}\right) - sin\left(\frac{k_iL}{2}\right)\right)\right)\right.}{(k_iL)^3}$$
$$\left.\frac{\left(sinh\left(\frac{k_iL}{4}\right) + sin\left(\frac{k_iL}{4}\right) - \alpha_i\left(cosh\left(\frac{k_iL}{4}\right) - cos\left(\frac{k_iL}{4}\right)\right)\right)}{(k_iL)^3}\right] \quad (2.31)$$

2.2 Piezoelectric

The piezoelectric effect is found with crystal structures lacking a symmetry center regarding the positive and negative ions of the crystal lattice. Thus, the condition for the occurrence of the piezoelectric effect is the existence of polar axes within the crystal structure. Polar means, that there is an electrical dipole moment in the axis directions caused by the distribution of the electrical charge in the chemical bond. From the outer point of view, the crystal is electrically neutral. A deformation along the polar axis, by applying an electric field or a mechanical force, causes an additional electrical polarization to form along this axis. The electrical polarization is caused by the displacement of the positive and negative ions of the crystal lattice against each other resulting in an electrical charge on the appropriate crystal surfaces either along or perpendicular to the polar axis and thus in an outside electrical polarization voltage. An important property of materials exhibiting a measurable piezoelectric effect is their high resistivity. Usually this is to be expected because the piezoelectric charge is small.

2.2.1 Mathematical Description

Mathematically piezoelectricity can be described by the strain matrix formulation equation (2.32) or stress matrix formulation equation (2.33); where σ_p/σ_q are the stress terms, ϵ_p/ϵ_q are the strain terms, d_{iq}/d_{pk} is the piezoelectric coefficient, e_{iq}/e_{pk} is the piezoelectric modulus, D_i is the electric displacement, ϵ^{ϵ}_{ik} is the permittivity at constant strain, ϵ^{σ}_{ik} is the permittivity at constant stress, Y^E_{pq} is the modulus of elasticity and s^E_{pq} is the elastic compliance coefficient. The elastic compliance coefficient is the inverse of the modulus of elasticity. The piezoelectric coefficient and elastic compliance have the following relationship: $d_{iq} = \sum_p e_{ip}S^E_{pq}$ and stress and strain have the following relationship: $\sigma_p = \sum_p Y^E_{pq}\epsilon_q$

$$\begin{bmatrix} \epsilon_p \\ D_i \end{bmatrix} = \begin{bmatrix} S^E_{pq} & d_{pk} \\ d_{iq} & \epsilon^{\sigma}_{ik} \end{bmatrix}\begin{bmatrix} \sigma_q \\ E_k \end{bmatrix} \quad (2.32)$$

$$\begin{bmatrix} \sigma_p \\ D_i \end{bmatrix} = \begin{bmatrix} Y^E_{pq} & e_{pk} \\ e_{iq} & \epsilon^{\epsilon}_{ik} \end{bmatrix}\begin{bmatrix} \epsilon_q \\ E_k \end{bmatrix} \quad (2.33)$$

The terms above, for brevity, are given in tensor notation where p and q are between 1&6 and i and k are between 1&3. The associated axial relation to: (a)p and q numbers are: 1, 2, 3, 4, 5, 6 related to x, y, z, yz, xz and xy and (b)i and k numbers are: 1, 2, 3 related to x, y and z. This yields the following matrix for each of the components:

Strain Matrix:

$$\epsilon_p = \begin{bmatrix} \epsilon_1 \\ \epsilon_2 \\ \epsilon_3 \\ \epsilon_4 \\ \epsilon_5 \\ \epsilon_6 \end{bmatrix} = \begin{bmatrix} \epsilon_x \\ \epsilon_y \\ \epsilon_z \\ \epsilon_{yz} \\ \epsilon_{xz} \\ \epsilon_{xy} \end{bmatrix}$$

Stress Matrix:

$$\sigma_p = \begin{bmatrix} \sigma_1 \\ \sigma_2 \\ \sigma_3 \\ \sigma_4 \\ \sigma_5 \\ \sigma_6 \end{bmatrix} = \begin{bmatrix} \sigma_x \\ \sigma_y \\ \sigma_z \\ \sigma_{yz} \\ \sigma_{xz} \\ \sigma_{xy} \end{bmatrix} \frac{N}{m^2}$$

Elastic Compliance Matrix:

$$s_{pq}^E = \begin{bmatrix} s_{11} & s_{12} & s_{13} & s_{14} & s_{15} & s_{16} \\ s_{21} & s_{22} & s_{23} & s_{24} & s_{25} & s_{26} \\ s_{31} & s_{32} & s_{33} & s_{34} & s_{35} & s_{36} \\ s_{41} & s_{42} & s_{43} & s_{44} & s_{45} & s_{46} \\ s_{51} & s_{52} & s_{53} & s_{54} & s_{55} & s_{56} \\ s_{61} & s_{62} & s_{63} & s_{64} & s_{65} & s_{66} \end{bmatrix} \frac{m^2}{N}$$

Modulus of Elasticity:

$$Y_{pq}^E = \begin{bmatrix} Y_{11} & Y_{12} & Y_{13} & Y_{14} & Y_{15} & Y_{16} \\ Y_{21} & Y_{22} & Y_{23} & Y_{24} & Y_{25} & Y_{26} \\ Y_{31} & Y_{32} & Y_{33} & Y_{34} & Y_{35} & Y_{36} \\ Y_{41} & Y_{42} & Y_{43} & Y_{44} & Y_{45} & Y_{46} \\ Y_{51} & Y_{52} & Y_{53} & Y_{54} & Y_{55} & Y_{56} \\ Y_{61} & Y_{62} & Y_{63} & Y_{64} & Y_{65} & Y_{66} \end{bmatrix} \frac{N}{m^2}$$

Piezoelectric Coefficient Matrix:

$$d_{iq} = \begin{bmatrix} d_{11} & d_{12} & d_{13} \\ d_{21} & d_{22} & d_{23} \\ d_{31} & d_{32} & d_{33} \\ d_{41} & d_{42} & d_{43} \\ d_{51} & d_{52} & d_{53} \\ d_{61} & d_{62} & d_{63} \end{bmatrix} \frac{C}{N}$$

Piezoelectric Constant Matrix:

$$e_{iq} = \begin{bmatrix} e_{11} & e_{12} & e_{13} \\ e_{21} & e_{22} & e_{23} \\ e_{31} & e_{32} & e_{33} \\ e_{41} & e_{42} & e_{43} \\ e_{51} & e_{52} & e_{53} \\ e_{61} & e_{62} & e_{63} \end{bmatrix} \frac{C}{m^2}$$

Permittivity Matrix:

$$\epsilon_{iq}^{E} = \begin{bmatrix} \epsilon_{11} & \epsilon_{12} & \epsilon_{13} \\ \epsilon_{21} & \epsilon_{22} & \epsilon_{23} \\ \epsilon_{31} & \epsilon_{32} & \epsilon_{33} \end{bmatrix}$$

The matrices above are properties of material. The possible vibration modes and suitable electrode configuration for piezoelectric activation are determined by either piezoelectric coefficient matrix or piezoelectric constant matrix. An applied field will cause a strain/stress in a particular direction resulting in a charge proportional to the amount of deflection. Mathematically, for an applied electric field the matrix in equation (2.32) reduces to equations (2.34) and (2.35). The former is the strain produced due to the applied electric field and the latter is the electric displacement due to the piezoelectric strain produced from the applied field, or the inverse piezoelectric effect, and the dielectric. These strains/stress produce moments, calculated using equation (2.3), which can be used to determine the deflection of the cantilever or bridge using equations (2.21) or (2.30). Additionally the piezoelectric charge, equation (2.36), can be derived using the electric displacement. Therefore, an applied field drives the device while the resulting charge from the deflection is detected.

$$\epsilon_p = d_{pk} E_k \tag{2.34}$$

$$D_i = d_{ip}\sigma_p + \epsilon_{ik} E_k$$

$$D_i = d_{ip}\sum_p Y_{pq}^{E} e_q + \epsilon_{ik} E_k \tag{2.35}$$

$$Q = \iint D_i didj \tag{2.36}$$

Using the longitudinal piezoelectric coefficients flexural vibrations/deflection is achieved. This is done by creating either a monomorph or a bimorph structure.

2.2.2 Monomorph

A monomorph consists of an active piezoelectric layer and a passive elastic layer, figure (2.6) [5]. In this figure the piezoelectric strain component is along the $x - direction$. The movement of the piezoelectric component resulting from its expansion or compression is restricted by the passive elastic component. As a result an internal piezoelectric moment arises deforming the monomorph as shown in figure (2.7) [5]. As is seen in the figure, the total deflection in the $z - direction$ is much larger than the deformation of the piezoelectric component in $x - direction$ and the applied electric field is opposite in direction to the polarization.

The resulting deflection hence the detected piezoelectric charge is dependent on the thickness of the piezoelectric and elastic layer. In order to increase deflection, the passive elastic component can be replaced by a second active piezoelectric component. This structure is called a bimorph.

2.2.3 Bimorph

A bimorph consists of two active piezoelectric components. These layers can either be polarized in the same or opposite directions. If the polarization of both layers are identical the field applied must be in the opposite direction in order to induce extension on one component and compression in the other, thereby creating a bending moment. This type of electrical configuration is called parallel connection, figure (2.8)(a) [5]. However, if the polarization is in the opposite direction the applied field can be in the same direction, figure (2.8)(b) [5]. This type of configuration is called series connection. The advantage of the series connection is no contact needs to be made with the internal

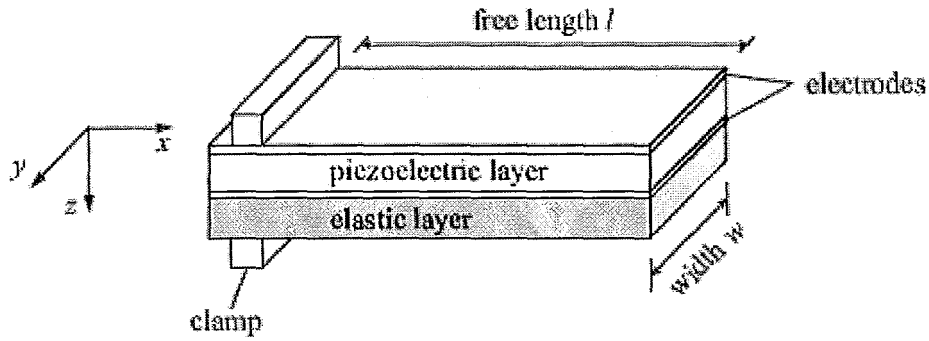

Figure 2.6: Layer sequence of a monomorph[5]

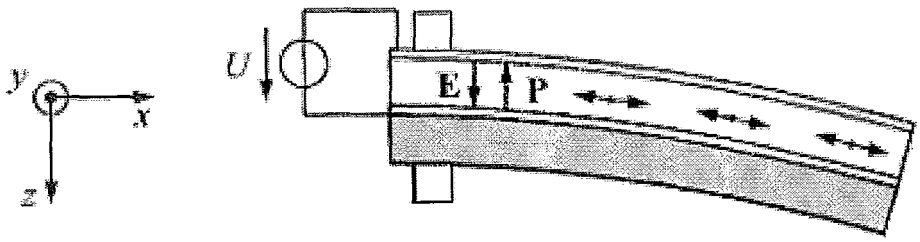

Figure 2.7: Deflection of monomorph due to an applied field (**E**). **E** and **P** are aligned anti-parallelly[5]

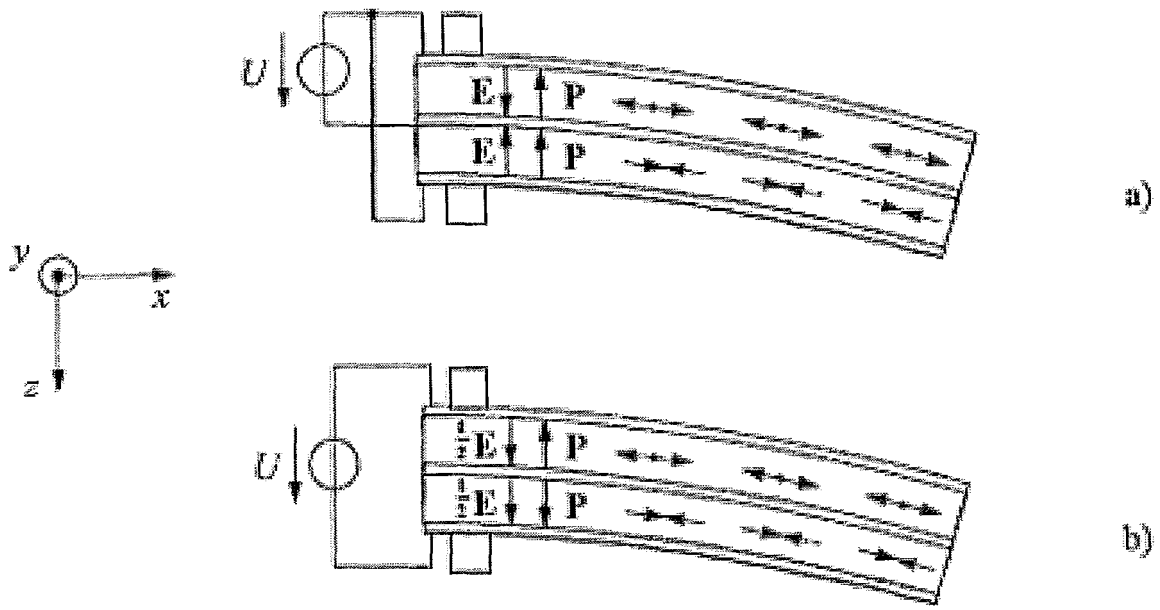

Figure 2.8: Deflection of bimorph subjected to a field - (a) parallel bimorph, (b) serial bimorph[5]

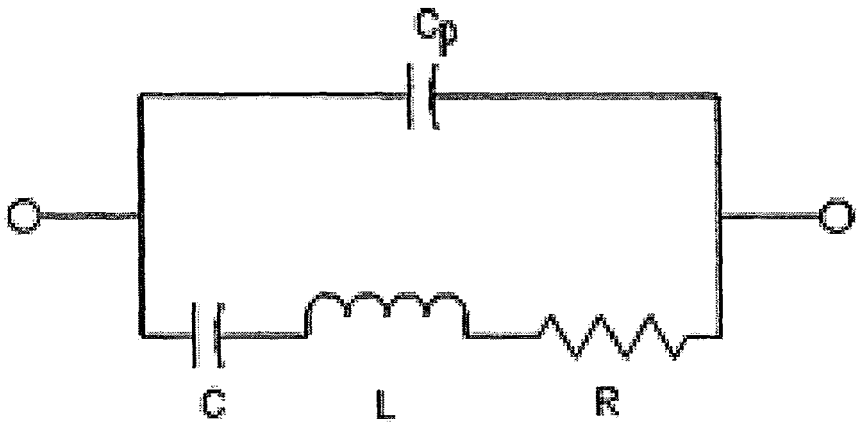

Figure 2.9: Piezoelectric resonator circuit. RLC are the motional components at resonance and C_p is the package or dielectric capacitance

electrode. However, within one single layer the value of the electric field is almost half as large as with the parallel bimorph.

The above two are examples of a two terminal device, i.e. one terminal is used to drive the device while the other is used to detect the resulting charge. For the parallel bimorph one could split the two drive electrodes into a drive and detect turning it into a three terminal device. The difference between two and three terminal configuration will be discussed in the later sections.

2.3 Electrical Resonator Circuit

The equivalent circuit of an electrical resonator is the familiar RLC circuit. However, from equation (2.35) there are two components to the total detected charge: piezoelectric and dielectric. The equivalent circuit for such a system is two capacitors in parallel. The resonator part, RLC, will be on one arm and the dielectric capacitance or package capacitance in the other arm as illustrated in figure (2.9).

The equivalent impedance and its magnitude for this circuit is given by equation (2.37) and (2.38), where $w = 2\pi f$, $X_C = 1/wC$, $X_L = wL$ and $X_{C_p} = 1/wC_p$.

$$Z = \left(\frac{1}{R + j\left(wL - 1/wC\right)} + jwC_p \right)^{-1}$$

$$Z = \left(\frac{1 + jwC_pR - w^2LC_p + C_p/C}{R + j\left(wL - 1/wC\right)} \right)^{-1}$$

$$Z = \left(\frac{R + j\left(wL - 1/wC\right)}{1 + jwC_pR - w^2LC_p + C_p/C} \right) \tag{2.37}$$

$$Z^2 = \left(\frac{\left(RX_{C_p}\right)^2 + \left(\left(X_L - X_C\right)X_{C_p}\right)^2}{R^2 + \left(X_L - X_C - X_{C_p}\right)^2} \right) \tag{2.38}$$

The resonant and anti-resonant frequencies can also be derived from equation (2.37) by finding equivalent real and imaginary impedances and setting the imaginary part to zero. This yields the following equation:

$$Z = \left(\frac{R + j\left(-wR^2C_p + wL - w^3L^2C_p + {}^{(2wLC_p)}/_{C} - {}^{1}/_{wC} - {}^{C_p}/_{(wC)^2}\right)}{1 - 2w^2LC_p + {}^{(2C_p)}/_{C} + w^4L^2C_p^2 - 2w^2LC_p^2/C + C_p^2/C + (wRC_p)^2} \right)$$

Setting the imaginary part to zero yields:

$$w^2LC^2 - C - w^4L^2C_pC^2 + 2w^2LCC_p - C_p - w^2R^2C_pC^2 = 0$$

The last term in this equation is assumed to be negligible as compared to other terms in the equation. This assumption is only valid in the regime where R is low. Omitting this term and calculating the roots of the equation gives the resonant and anti-resonant frequencies – equations (2.39) and (2.40). Substituting these equations into equation (2.37) the resonance and anti-resonance impedance is given by equations (2.41) and (2.42). The impedance at resonance is assumed to be approximately equal to R, in the regime where R is much lower than the impedance of the package capacitance.

$$w_r = \sqrt{\frac{1}{LC}} \tag{2.39}$$

$$w_A = \sqrt{\frac{1}{LC} + \frac{1}{LC_p}} \tag{2.40}$$

$$Z_R = \frac{R}{\left(1 - wRC_p^2\right)} \sim R \tag{2.41}$$

$$Z_A = \frac{1}{w_A^2C_p^2R} \tag{2.42}$$

Figure (2.10) illustrates the total impedance of the circuit as a function of frequency as given by equation (2.38). The resonant and anti-resonant point represents the lowest and highest impedance and their values are given by equations (2.41) and (2.42). The frequency at these points are given by equations (2.39) and (2.40). The tails of this figure are the values of the dielectric or package capacitance, i.e. at frequencies other than the resonance/anti-resonance regime the impedance of the package capacitance dominates.

The graphs of the real and complex part of equation (2.37) are illustrated in figures (2.11) and (2.12). The anti-resonant point in figure (2.11) is the point of the highest impedance and the slope in the tails is due to the package capacitance. In figure (2.12) the two gray dots represent the resonant and anti-resonant points. These values are zero. At frequencies below the resonant frequency and above the anti-resonant frequency the package capacitance dominates and is called the capacitive regime. At frequency values between the resonance and anti-resonance the inductance dominates, i.e. the inductive regime.

The phase of the circuit is given by equation (2.43) and is derived from equation (2.37). At resonance and anti-resonance the phase is zero, as is illustrated in figure (2.13), meaning the circuit is purely resistive.

$$\theta = \tan^{-1}\left(\frac{-wR^2C_p + wL - w^3L^2C_p + {}^{(2wLC_p)}/_{C} - {}^{1}/_{wC} - {}^{C_p}/_{(wC)^2}}{R} \right) \tag{2.43}$$

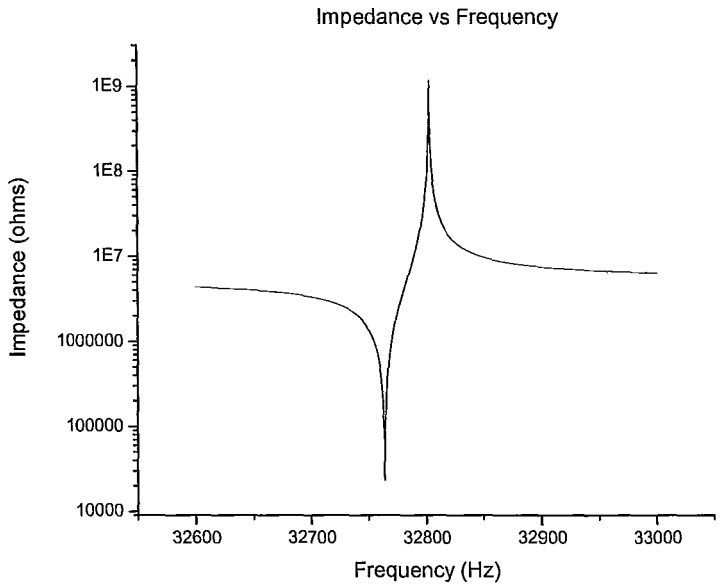

Figure 2.10: Impedance vs Frequency. Lowest impedance is at resonance and highest impedance is at anti-resonance. The impedance off resonance is dominated by the package capacitance.

2.4 Q-value

The Q value or the quality factor of a mechanical resonator is defined as the ratio of the energy stored per cycle to the energy dissipated per cycle[10]. Mathematically Q value is derived from the free oscillation equation for an oscillator as follows [11]

$$m\ddot{x} + b\dot{x} + kx = 0$$

The solution to this equation is $x(t) = x_o exp(-\delta t) cos(wt + \phi)$; where $\delta = \frac{b}{2m}$, $w^2 = \frac{k}{m} - \delta$, $\tau^* = \delta^{-1}$, $Q_{mech} = \frac{w\tau^*}{2}$, $\theta = \frac{\pi}{Q}$, $x_o$and φ are determined by the oscillator's initial conditions.

Similar equations and expressions for δ, τ^*, θ and Q_{mech} may be written for a lumped-element circuit. Taking a simplistic approach to derive the above values, i.e. a mechanical oscillator can be thought of as an electrical oscillator:

$$L\ddot{q} + R\dot{q} + \frac{q}{C} = 0$$

The solution to this equation is $Q(t) = Q_o exp(-\delta t) cos(wt + \phi)$; where $\delta = \frac{b}{2L}$, $w^2 = \frac{1}{LC} - \delta^2$, $\tau^* = \delta^{-1}$, $Q_{elec} = \frac{w\tau^*}{2}$, $\theta = \frac{\pi}{Q}$, Q_o and φ are determined by the oscillator's initial conditions. For systems with small dissipation, i.e. δ small, $Q_{elec} = \frac{1}{w_r RC}$; which is the familiar result for an electrical resonator quality factor. Equating mechanical Q_{mech} to electrical Q_{elec} the mechanical damping term is determined as a function of the resistance R, $b = \frac{mR}{L}$. Experimentally the Q-value can be determined by calculating the ratio of the resonant frequency to its spread, i.e. $-3dB$, equation (2.44)

$$Q = \frac{f_r}{\triangle f_{-3dB}} \tag{2.44}$$

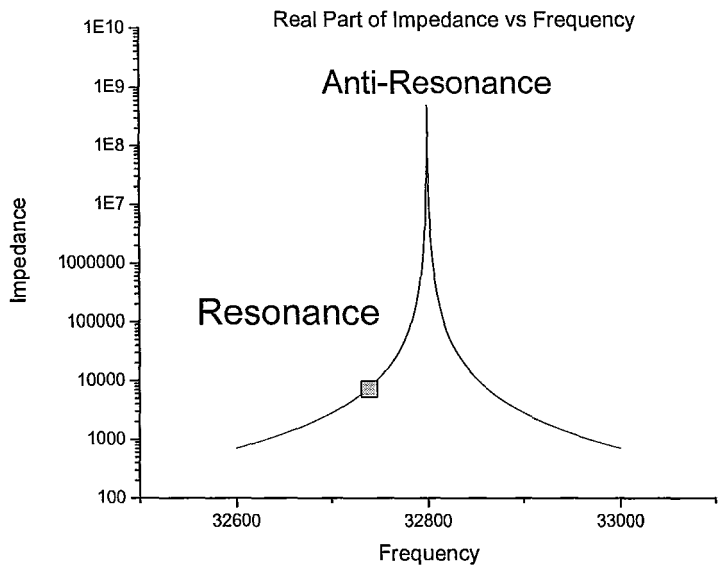

Figure 2.11: Plot of real component of equation (2.37)

Q	Value
Low	$0 - 10^3$
Medium	$10^3 - 10^5$
High	$> 10^5$

Table 2.3: Classification of Q

From an application point of view, dissipation within a resonator: limits its sensitivity to external applied forces (signal), broadens its natural linewidth and determines the minimum intrinsic power at which the device must operate. Therefore medium Qs are desired for most applications. Table (2.3) is the classification of Qs and their associated values. In applications like: low phase noise oscillators such as those required in time keeping [12][13], in highly selective filters [14] for signal processing and in resonant sensors where resonance frequency shifts are tracked due to external perturbations [15][16], Q-value is the performance limiting aspect. In such applications, High Qs are desired.

The mechanisms that limit the Q-value of mechanical resonators are characterized as being intrinsic and extrinsic. Intrinsic means processes that are fundamental to the material. These occur because deformations in mechanical vibrations are accompanied by processes that are not thermodynamically reversible. These processes are responsible for dissipation of the oscillation energy[11]. Extrinsic mechanisms are energy losses resulting from technological and design factors. Intrinsic mechanisms include:

1. Thermoelastic Dissipation: caused by vibratory volume changes producing spatially inhomogeneous temperature changes. These resulting temperature gradients induce heat flow, which is accompanied by an entropy increase and a conversion of vibration energy into thermal energy

2. Dissipation due to phonon-phonon interactions: caused by interactions between acoustic waves, as a result of resonant vibrations, and thermal phonons. If the acoustic wavelength is consid-

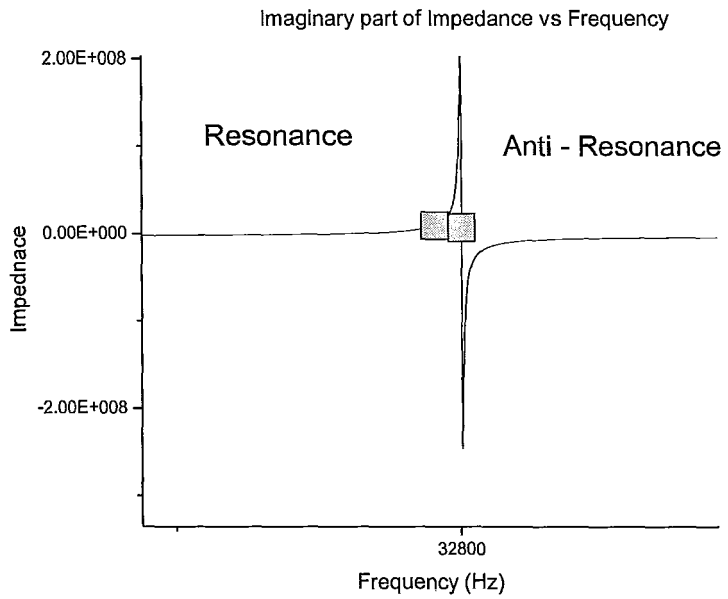

Figure 2.12: Plot of imaginary component of equation (2.37). At resonance and anti-resonance the imaginary components are zero.

erably larger than the mean free path of the phonons, one can consider the acoustic waves as locally changing the phonon frequencies thereby perturbing the phonon distribution function away from its equilibrium Planck form. This process of the phonon gas restoring to thermal equilibrium is accompanied by dissipation of the acoustic-wave energy

3. Dissipation due to lattice defects: are characterized as internal friction mechanisms. These internal friction mechanisms produce a phase lag between the stress and strain relaxation times causing dissipation of energy. Lattice defects include: point defects, dislocations, interfaces etc

Extrinsic mechanisms include:

1. Losses due to gas damping: Mechanical resonator oscillating in a gaseous medium creates sound waves that carry its power away. For high Qs low pressures are required

2. Surface losses: caused due to the inhomogeneity of the surface properties from that of the bulk. These inhomogeneities produce many relaxation processes causing an upset of the thermodynamic balance from the bulk. Restoring this balance is accompanied by irreversible processes that give rise to the dissipation of elastic energy. The cause for surface losses are predominantly machining, causing surface defects such as microcracks, dislocations etc, and interactions of surface with the environment causing the production of two layers of crystal surface with the top layer being polycrystalline

3. Clamping losses: cause dissipation of energy from an oscillating resonator to the clamp. This energy dissipation occurs due to acoustic coupling to the clamps. Therefore, to achieve high-Qs resonators must be designed to minimize this energy loss

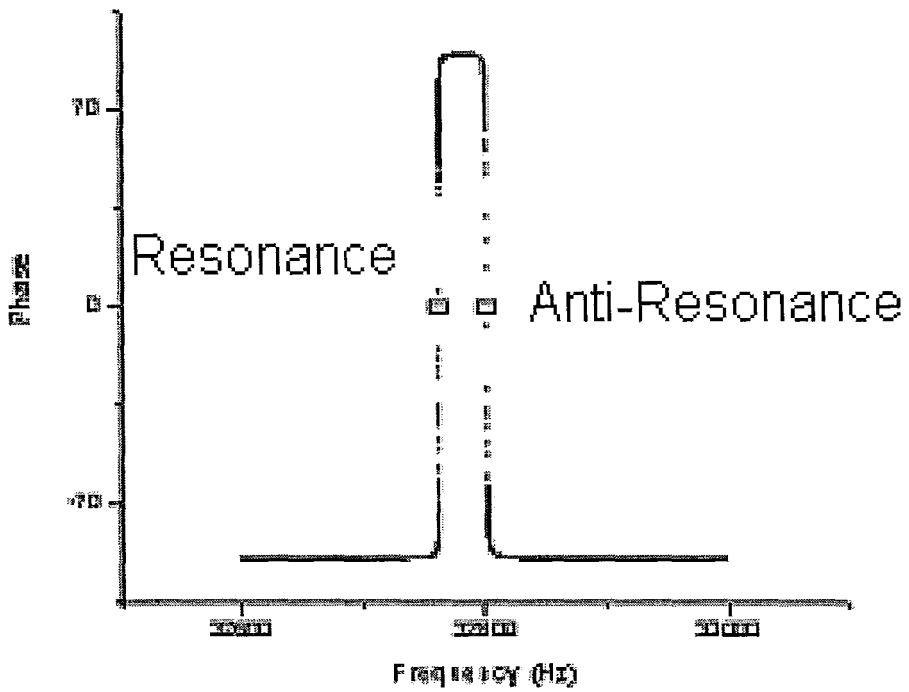

Figure 2.13: Phase vs Frequency. The phase is zero at resonance and anti-resonance

Chapter 3

Quartz Tuning Fork

The piezoelectric properties of quartz were first investigated by the Curie brothers in the 1800s. The use of this property, in quartz, came to prominence during World War I when Langevin used piezoelectrically excited quartz plates to generate and receive sound waves in water for use in submarine detection[10]. The primary use of quartz as a frequency controlling element was developed and later patented by Cady in 1920[10]. This circuit consisted of a three-stage amplifier with the quartz resonator in the feedback path. During World War II quartz resonators in military communications became standard. In 1940 the armed forces projected a requirement of 100,000 quartz crystals, but during the war this increased to 30 million resulting in a cash program costing over $1 billion[10]. Various types of quartz resonators like discs, tuning forks, bars etc are made and find applications in micro-balances, thin film thickness monitors and watches. Additionally, high purity crystalline quartz, having Qs as high as 2.5e6[17] and more, is also available. Owing to the high Qs, lately there has been an increased interest in quartz tuning forks for microscopy applications such as atomic force microscopy[18, 19, 20] and scanning probe microscopy[21, 22].

This section begins with a discussion on the piezoelectric properties of quartz. Using the piezoelectric constant matrix the design, theoretical and experimental results of three different sizes, table (3.1), of a conventional quartz resonator, quartz tuning fork (QTF), is investigated. These QTFs were bought from digikey and their part numbers are: Digi_Key 300-1001-ND, Digi_Key 300-1002-ND and Digi_Key 300-1003-ND for large, medium and small respectively.

3.1 Piezoelectric property of quartz

Crystalline quartz or alpha, $\alpha-$quartz is composed of two elements, silicon and oxygen. As discussed in the theory section α-quartz belongs to the class of crystals lacking a symmetry center between the positive and negative ions of the crystal lattice. For a better understanding, the structure cell of α-quartz is depicted in figure (3.1)[5]. It consists of negative charged O^- ions, positive charged Si^+ ions and has three two-fold polar rotation axes X_1, X_2 and X_3 in the drawing plane and a three-fold rotation axis Z perpendicular to the drawing plane. This is the familiar trigonal, point group 3m of crystals.

	Length (m)	Width (m)	Height (m)
Large Fork	3.62×10^{-3}	5.80×10^{-4}	2.80×10^{-4}
Medium Fork	3.12×10^{-3}	3.60×10^{-4}	2.40×10^{-4}
Small Fork	2.48×10^{-3}	2.40×10^{-4}	1.20×10^{-4}

Table 3.1: QTF Dimensions

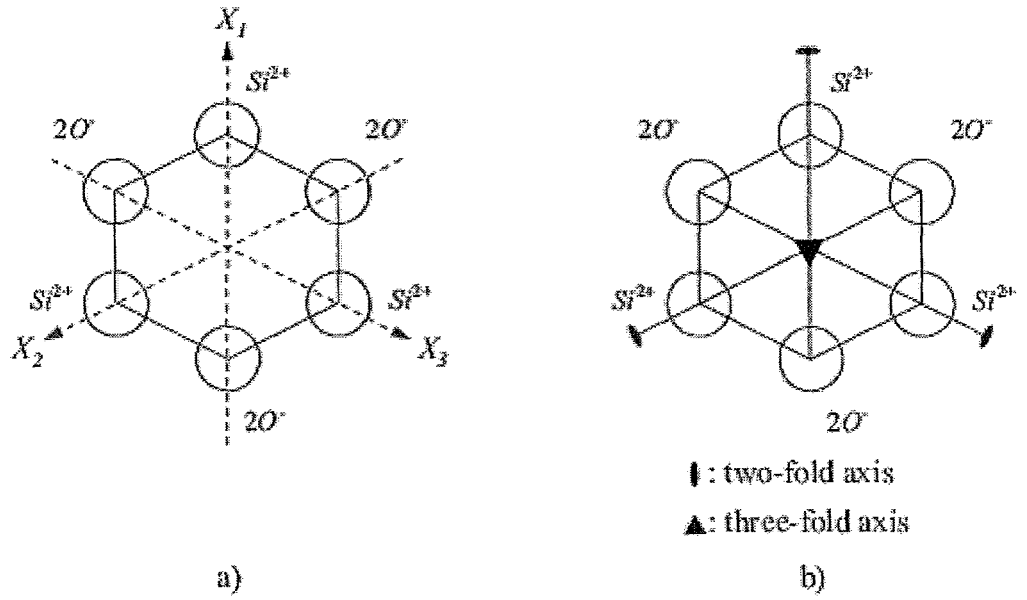

Figure 3.1: Simplified structure cell of quartz: (a) arrangement of Si^+-ions and O^--ions with main crystal axis; (b) two- and three- fold axis[5]

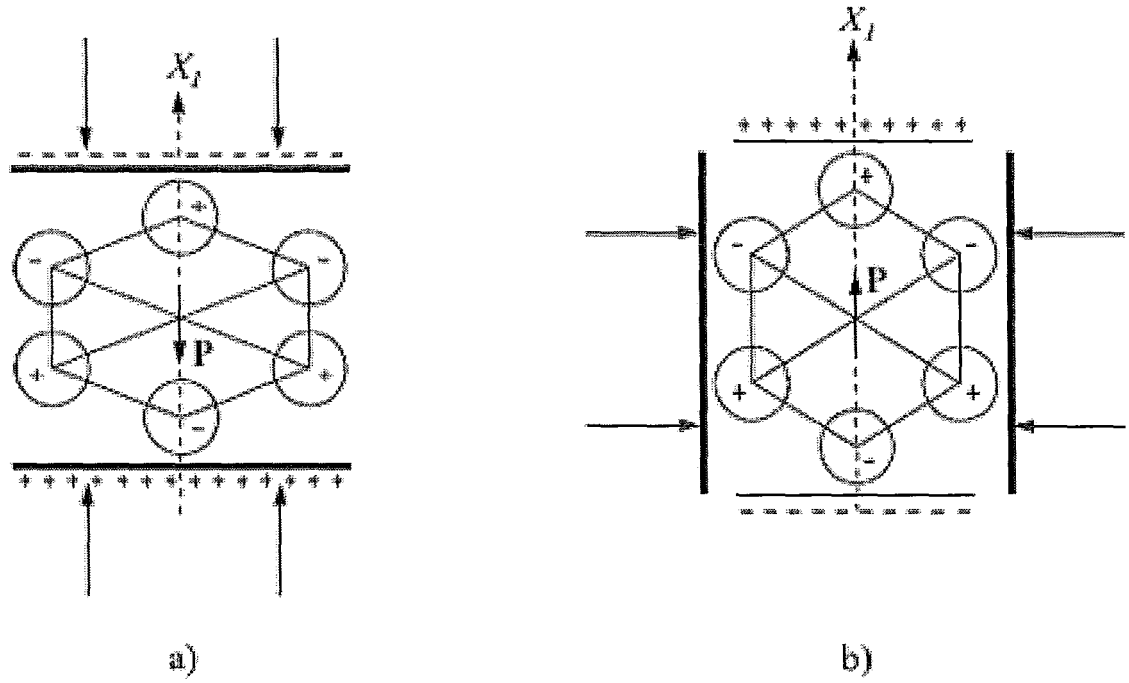

Figure 3.2: Direct piezoelectric effect within a structure cell of quartz: (a) longitudinal piezoelectric effect; (b) transversal piezoelectric effect[5]

A deformation of the quartz structure along the polar X_1-axis causes the formation of an

electrical polarization. This electrical polarization is caused by the displacement of the positive and negative ions of the crystal lattice against each other, figure(3.2), resulting in an electrical charge on the appropriate crystal surfaces perpendicular to the X_1-axis and thus in an outside electrical polarization voltage. An exposure to compression and tensile stresses acting perpendicularly to the X_1-axis results in an additional electrical polarization with opposite sign in X_1-axis direction, figure(3.2).

Quartz tuning forks are made from α-quartz that is cut $35^0 15'$ from the Z axis, called AT-cut[10]. They have the advantage of frequency stability from $-65^0 C$ to $100^0 C$ [10].

The coefficients for α-quartz are:

Modulus of Elasticity[10]:

$$Y_{pq}^E = \begin{bmatrix} 86.74 & 6.97 & 11.90 & -17.91 & 0 & 0 \\ 6.97 & 86.74 & 11.90 & -17.91 & 0 & 0 \\ 11.90 & 11.90 & 107.2 & 0 & 0 & 0 \\ -17.91 & 17.91 & 0 & 57.93 & 0 & 0 \\ 0 & 0 & 0 & 0 & 57.93 & -17.91 \\ 0 & 0 & 0 & 0 & -17.91 & 39.89 \end{bmatrix} GPa$$

Piezoelectric coefficient matrix[10]:

$$d_{iq} = \begin{bmatrix} -2.27 & 0 & 0 \\ 2.27 & 0 & 0 \\ 0 & 0 & 0 \\ -0.67 & 0 & 0 \\ 0 & 2.27 & 0 \\ 0 & 4.54 & 0 \end{bmatrix} \frac{pC}{N}$$

Piezoelectric constant matrix[10]:

$$e_{iq} = \begin{bmatrix} -0.173 & 0 & 0 \\ 0.173 & 0 & 0 \\ 0 & 0 & 0 \\ 0.040 & 0 & 0 \\ 0 & -0.040 & 0 \\ 0 & 0.173 & 0 \end{bmatrix} \frac{C}{m^2}$$

Permittivity matrix[10]:

$$\epsilon_{iq}^E = \begin{bmatrix} 4.5 & 0 & 0 \\ 0 & 4.5 & 0 \\ 0 & 0 & 4.6 \end{bmatrix}$$

3.2 Design

As shown in figure (3.3) a quartz tuning fork is composed of two arms or tines and a base. The tines can be considered as cantilevers. The tines of the tuning fork are parallel bimorphs, i.e. homogenized polarization across the tines. Figure (3.4) indicates that flexural vibrations of the arms occur in the XY-plane. This flexural vibration is achieved using the electrode pattern illustrated in figure (3.5)(a)[23]. The electrode pattern is on both the front and back sides of the tines. Also, the electrodes are placed such that each tine has a field generated opposite to the other tine. When a positive voltage is applied to electrode A and a negative voltage to electrode B an electric field is generated across the x-direction, figure (3.5)(b). Using the above piezoelectric strain matrix an x-directed field will result in an extension or compression strain in the x-direction equation (3.1) and y-direction equation (3.2) and a shear strain in the yz plane equation (3.3). In this case, the

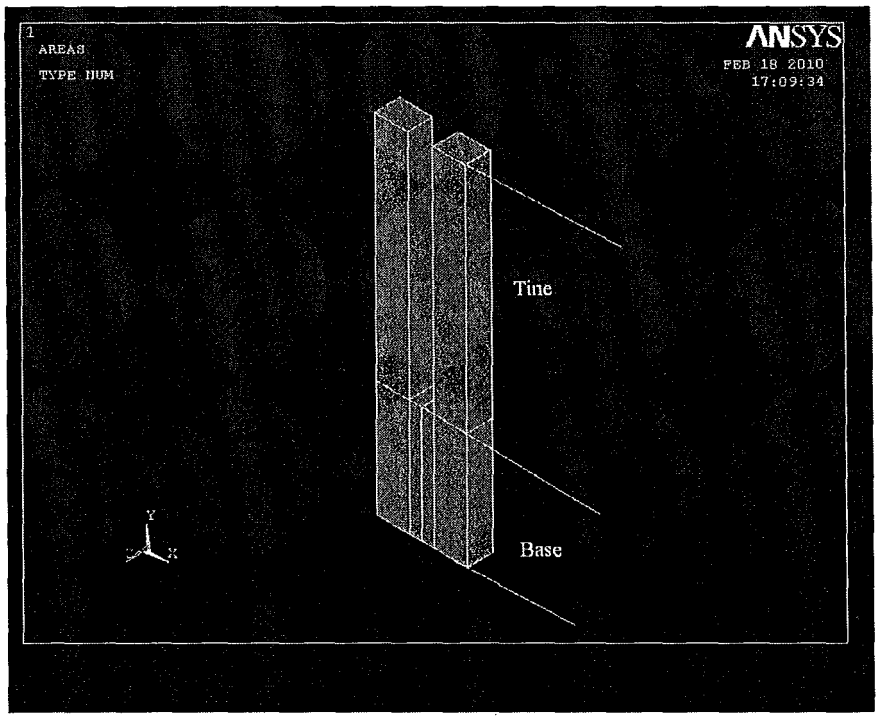

Figure 3.3: Schematic of a quartz tuning fork showing the base and tines

deformation along the x-direction can be ignored because the dimension along the y-direction is an order of magnitude greater than the x-direction and will therefore experience the greatest strain. The shear can also be ignored because the coefficient of shear strain is 0.23 times lower than the x and y strain. As seen in figure (3.5)(b), the right half of the tine has a field opposite to that of the left half of the tine resulting in bending because the right half will be in compression/extension while the left half will be in extension/compression. Switching the direction of the applied potential will result in bending in the opposite directions.

$$\epsilon_p = d_{iq} E_q$$

$$\begin{bmatrix} \epsilon_x \\ \epsilon_y \\ \epsilon_z \\ \epsilon_{yz} \\ \epsilon_{xz} \\ \epsilon_{xy} \end{bmatrix} = 1.0 \times 10^{-12} \begin{bmatrix} -2.27 & 0 & 0 \\ 2.27 & 0 & 0 \\ 0 & 0 & 0 \\ -0.67 & 0 & 0 \\ 0 & 2.27 & 0 \\ 0 & 4.54 & 0 \end{bmatrix} \begin{bmatrix} E_x \\ 0 \\ 0 \end{bmatrix}$$

$$\epsilon_x = -2.27 \times 10^{-12} E_x \tag{3.1}$$

$$\epsilon_y = 2.27 \times 10^{-12} E_x \tag{3.2}$$

$$\epsilon_{yz} = -0.67 \times 10^{-12} E_x \tag{3.3}$$

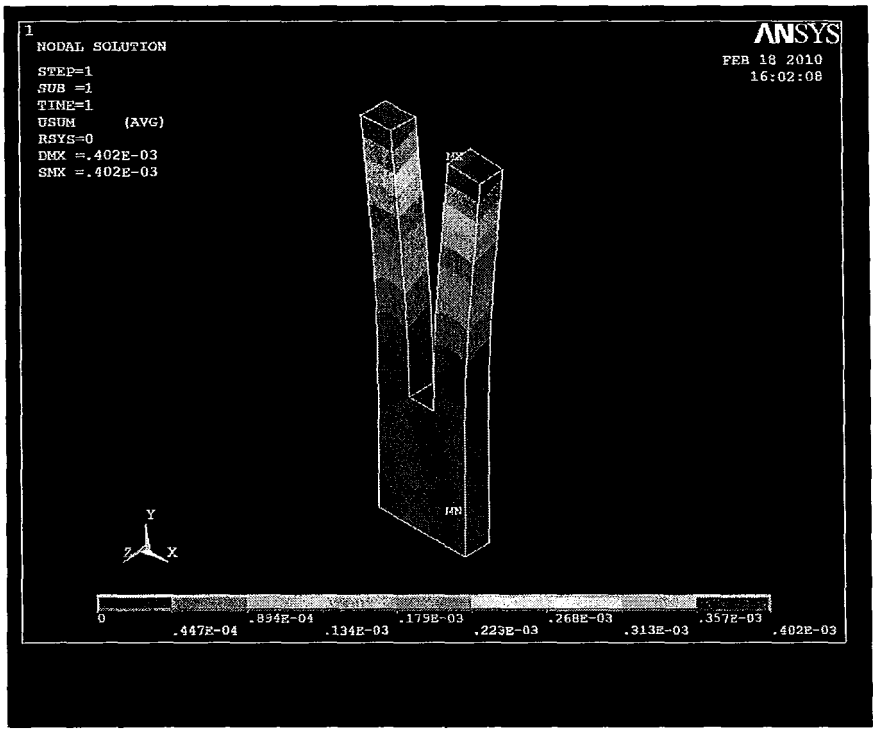

Figure 3.4: Flexural vibrations in XY plane

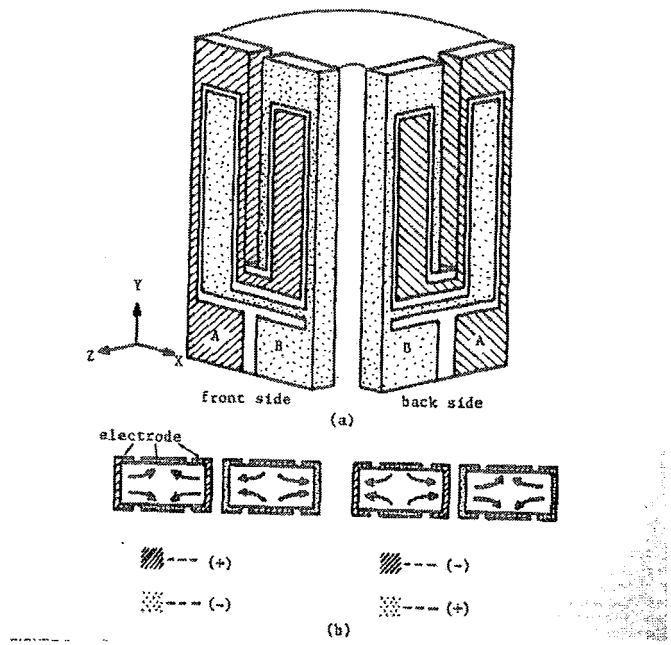

Figure 3.5: (a) Electrode pattern on both sides of a QTF for flexural vibration; (b) x directed electric field generated on the section of the tuning fork arm when voltage is supplied to electrodes[23]

The stress distribution in the XY-plane is shown in figure (3.6). As is seen all the stress is

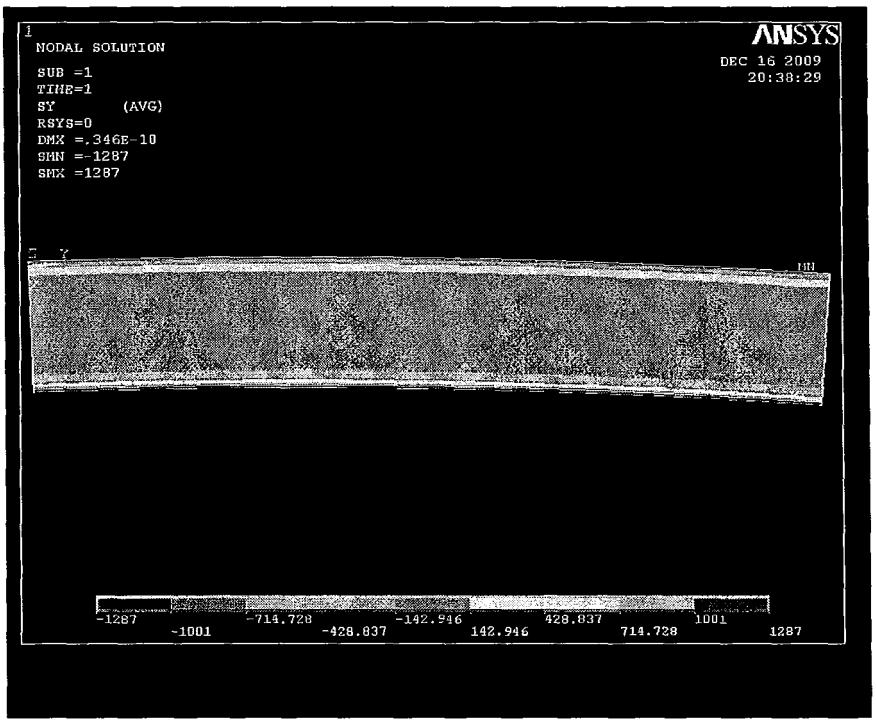

Figure 3.6: Stress distribution across XY-plane going from compressive(top) to extensional(bottom)

at the ends of the beam going from compressive to extensional and most of the beam experiences zero stress . This is expected because the corners of the beam experience maximum field.

With regards to the Q-value, a medium to high value is expected because: considering the intrinsic mechanisms low defect single crystal α-quartz is readily available with infrared Qs of 2 million[1] and greater[17] and considering the extrinsic mechanisms contributions from: (a) gas pressure can be neglected by placing the device in a vacuum, (b) surface losses, although hard to quantify, should not be the dominant factor because these devices are in the milli-meter range therefore the bulk properties should be dominant and (c) the clamping losses will be negligible because the tines are moving in equal and opposite directions, figure (3.4), resulting in the cancelling of reactionary forces at the base. This leads to negligible energy dissipation to occur due to negligible acoustic coupling.

3.3 Theoretical Result

From the previous section an electric field in the x-direction produces a longitudinal strain in the y-direction. Using equations (2.12)&(2.36) the tip deflection and piezoelectric charge can be derived. The overview of the derivation, given in figure (3.7), is as follows: an applied voltage creates an x-directed field which produces a y-directed strain due to the piezoelectric effect. The resulting strain produces a y-directed stress. The stress creates a bending moment in the z-direction, due to the fixed support, resulting in a deflection in the x-direction. For calculating the charge the y-directed strain due to the applied field results in a dipole producing an electric displacement in the x-direction which can be integrated to calculate the piezoelectric charge. In the following derivations a single tine is

[1] Infrared Q is a term used for infrared absorption at various infrared frequencies used to measure hydrogen content. Hydrogen is the largest impurity found in Quartz causing dislocations. A high Q means low hydrogen content.

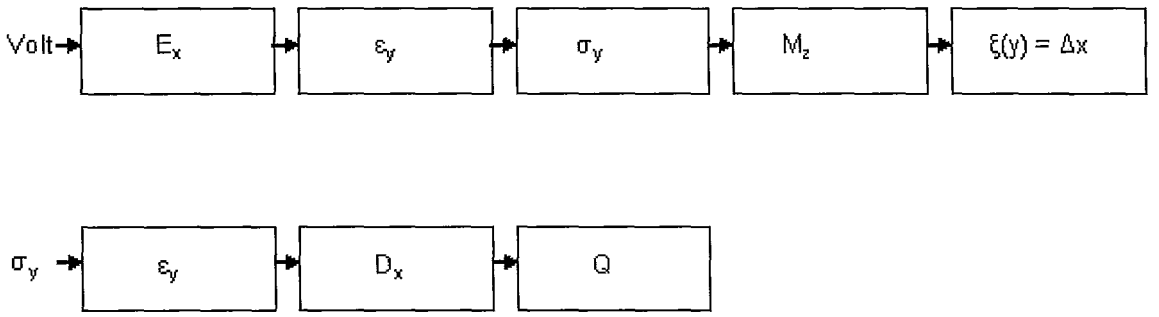

Figure 3.7: Overview of calculation of tip-deflection(top) and piezoelectric charge(bottom)

considered because of symmetry. Figure (3.8) is the geometry of a single tine and the associated coordinate system. Here the x-axis is the width, W_o - total width and W- half width, y-axis is the length, L, and z-axis is the height H, of the beam. The electrode is assumed to be on the full length and width of the tine, which is different from the real case figure(3.5)(a).

3.3.1 Deflection

The potential due to the electrode configuration is given by equation (3.4)[24] and the electric field is given by equation (3.5). Using the strain equation (2.34) the stress is given by equation (3.6). This is the normal stress pertaining to a normal force figure (2.3).

$$V(x,y) = \frac{4V_o}{\pi} \sum_{n=odd} \frac{1}{n} \frac{\cosh\left(\frac{n\pi x}{H}\right)}{\cosh\left(\frac{n\pi W}{H}\right)} \sin\left(\frac{n\pi z}{H}\right) \tag{3.4}$$

$$E_x(x,z) = -\frac{\partial V}{\partial x} = -4V_o \sum_{n=odd} \left[\frac{\sinh\left(\frac{n\pi x}{H}\right) \sin\left(\frac{n\pi z}{H}\right)}{H \cosh\left(\frac{n\pi W}{H}\right)} \right] \tag{3.5}$$

$$\sigma_y = d_{21} Y E_x(x,z) \tag{3.6}$$

The moment is calculated using equation (2.3). Equation (3.7) is the moment for the tine. In the derivation the moment is multiplied by two because the integration for x is from $-W...W$

$$M_z = \int_0^H \int_0^W 2\sigma_y x dx dz$$

$$M_z = \int_0^H \int_0^W 2d_{21} Y E_x x dx dz$$

$$M_z = d_{21} Y \int_0^H \int_0^W 2x \left(-4V_o \sum_{n=odd} \left[\frac{\sinh\left(\frac{n\pi x}{H}\right) \sin\left(\frac{n\pi z}{H}\right)}{H \cosh\left(\frac{n\pi W}{H}\right)} \right] \right) dx dz \tag{3.7}$$

Equation (3.7) consists of a constant and an integration term. Solving for the integration part, equation (3.8), of the moment equation yields equation (3.9) and the moment is given by equation (3.10). The latter equation is a constant multiplied by a a summation term which is a function of the geometrical parameters W/H. Figure (3.9) is a plot of this summation term vs W/H for the three different sizes of the QTF and table (3.2) is a summary of the moment for the different sizes of QTF. Large and small QTF approximately have the same value for $\sum_{n=odd} C_n$ but the medium QTF differs by 36.84%.

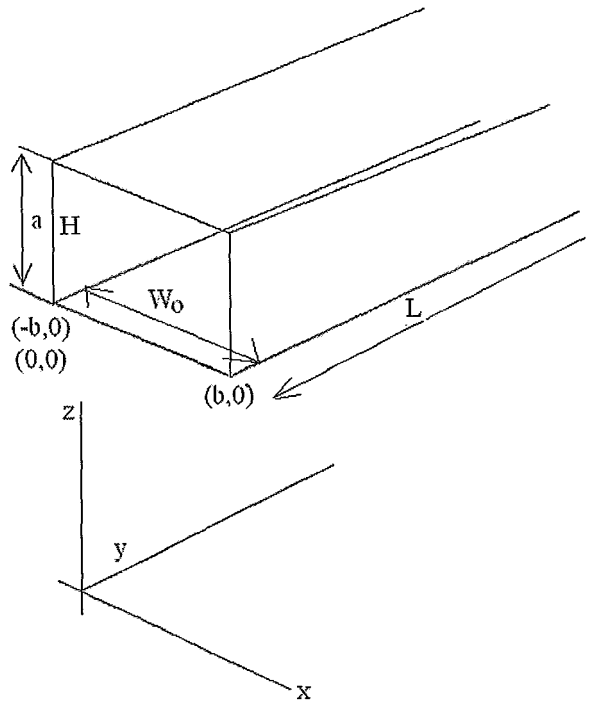

Figure 3.8: Geometry and associated coordinate system of a single tine

$$\int_0^H \int_0^W 2E_x x dx dz = 4V_o H \sum_{n=odd} \frac{\left(n\pi W e^{\left(\frac{2n\pi W}{H}\right)} + n\pi W - He^{\left(\frac{2n\pi W}{H}\right)} + H\right) e^{\left(-\frac{n\pi W}{H}\right)} \left(\cos\left(n\pi\right) - 1\right)}{\cosh\left(\frac{n\pi W}{H}\right)\left(n^3\pi^3\right)} \tag{3.8}$$

$$\int_0^H \int_0^W 2E_x x dx dz = 4V_o H \sum_{n=odd} \frac{\left(n\pi W e^{\left(\frac{2n\pi W}{H}\right)} - He^{\left(\frac{2n\pi W}{H}\right)} + n\pi W + H\right) e^{\left(-\frac{n\pi W}{H}\right)} \left(\cos\left(n\pi\right) - 1\right)}{\cosh\left(\frac{n\pi W}{H}\right)\left(n^3\pi^3\right)}$$

$$\int_0^H \int_0^W 2E_x x dx dz = 4V_o H \sum_{n=odd} \frac{\left(e^{\left(\frac{2n\pi W}{H}\right)}\left(n\pi W - H\right) + \left(n\pi W + H\right)\right) e^{\left(-\frac{n\pi W}{H}\right)} \left(\cos\left(n\pi\right) - 1\right)}{\cosh\left(\frac{n\pi W}{H}\right)\left(n^3\pi^3\right)}$$

$$\int_0^H \int_0^W 2E_x x dx dz = 4V_o H \sum_{n=odd} \frac{\left(e^{\left(\frac{2n\pi W}{H}\right)} H\left(n\pi\frac{W}{H} - 1\right) + H\left(n\pi\frac{W}{H} + 1\right)\right) e^{\left(-\frac{n\pi W}{H}\right)} \left(\cos\left(n\pi\right) - 1\right)}{\cosh\left(\frac{n\pi W}{H}\right)\left(n^3\pi^3\right)}$$

$$\int_0^H \int_0^W 2E_x x dx dz = 4V_o H^2 \sum_{n=odd} \frac{\left(e^{\left(\frac{2n\pi W}{H}\right)}\left(n\pi\frac{W}{H} - 1\right) + \left(n\pi\frac{W}{H} + 1\right)\right) e^{\left(-\frac{n\pi W}{H}\right)} \left(\cos\left(n\pi\right) - 1\right)}{\cosh\left(\frac{n\pi W}{H}\right)\left(n^3\pi^3\right)}$$

$$\int_0^H \int_0^W 2E_x x dx dz = 4V_o H^2 \sum_{n=odd} C_n \tag{3.9}$$

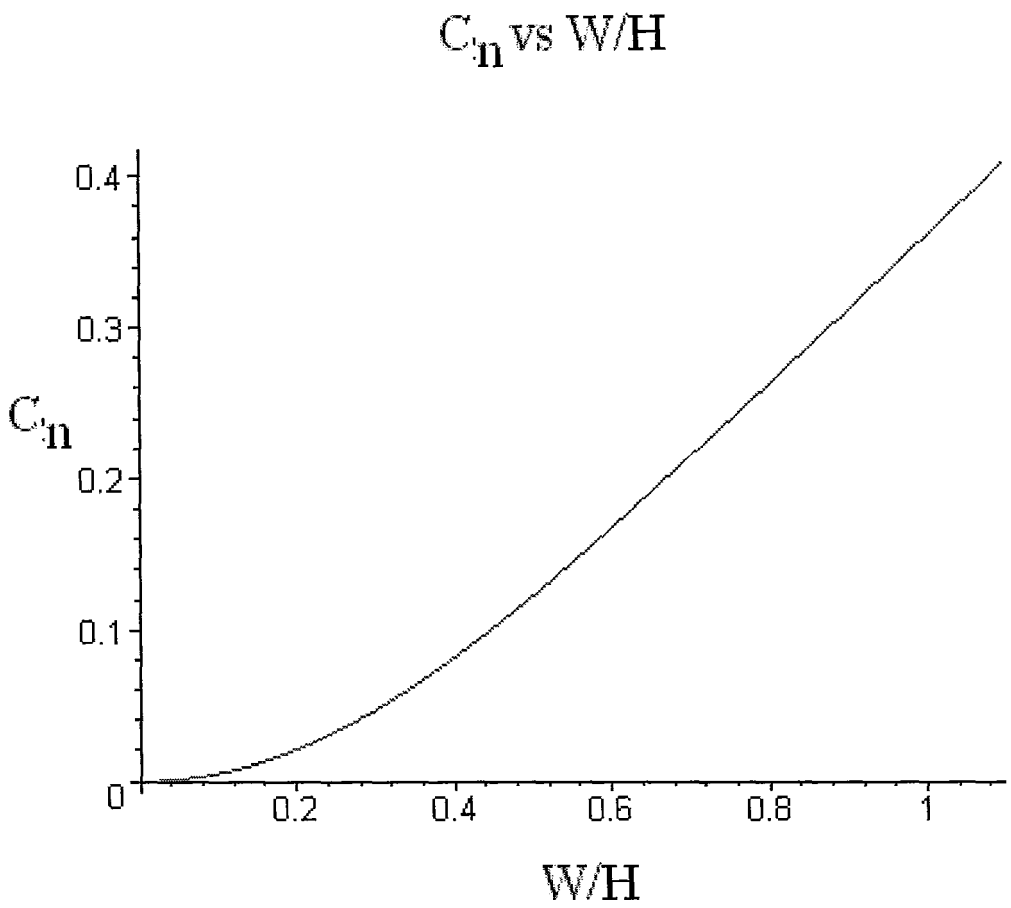

Figure 3.9: Plot of $\sum_{n=odd} C_n$ vs $\frac{W}{H}$ equation (3.10) for the three different sizes of the QTF.

	W (m)	H (m)	$\frac{W}{H}$	$\sum_{n=odd} C_n$	M_z
Large	2.9e-4	2.8e-4	1.04	0.3815147062	$2.069824105e-8V_o$
Medium	1.8e-4	2.4e-4	0.64	0.2408569532	$9.600365469e-9V_o$
Small	1.2e-4	1.2e-4	1.00	0.3637899148	$3.625093743e-9V_o$

Table 3.2: Moment for large, medium and small QTF

$$M_z = 4d_{21}YV_oH^2 \sum_{n=odd} C_n = 4e_{21}V_oH^2 \sum_{n=odd} C_n \tag{3.10}$$

The tip displacement can be determined using two approaches:

1. assuming the beam bends in a parabolic shape
2. using the mode shapes of a cantilever subjected to a constant moment

3.3.1.1 Parabolic Shape

The equation for parabolic deflection is $\xi(y) = \xi_0 \left(\frac{y}{L}\right)^2$; where ξ_0 is the tip deflection. The maximum deflection, as mentioned in the theory section, occurs at $y = L$. Using the 2nd order differential equation for beam bending the tip displacement is given by equation (3.11) and the equation (3.12) is the general expression for deflection along the tine.

$$\frac{1}{\rho} = \frac{M}{YI} = \frac{\partial^2 \xi}{\partial y^2} = \frac{2\xi_0}{L^2}$$

$$\frac{\partial^2 \xi}{\partial y^2} = \frac{2\xi_0}{L^2}$$

$$\frac{M}{YI} = \frac{2\xi_0}{L^2}$$

$$\xi_0 = \frac{ML^2}{2YI}$$

$$\xi_0 = 4e_{21}V_oH^2 \frac{L^2}{2YI} \sum_{n=odd} C_n$$

$$\xi_0 = 4e_{21}V_oH^2 \frac{L^2}{2Y\left(\frac{1}{12}(H)(2W)^3\right)} \sum_{n=odd} C_n$$

$$\xi_0 = \frac{3e_{21}HV_oL^2}{YW^3} \sum_{n=odd} C_n \tag{3.11}$$

$$\xi(y) = \frac{3e_{21}HV_oy^2}{YW^3} \sum_{n=odd} C_n \tag{3.12}$$

3.3.1.2 Mode shapes of a cantilever subjected to a constant moment

Two approaches are adopted (both approaches give the same result):

1. The parabolic deflection is decomposed into normal modes
2. Using virtual work formulation for moment, as in the theory section

Decomposing to normal modes

Starting with the general expression for the parabolic deflection, equation (3.13), equation (2.9) and equation (2.20) is used to determine the contribution of each mode, equation (3.14), to the tip deflection.

$$\xi(y) = \frac{My^2}{2YI} \tag{3.13}$$

Decomposing to normal modes:

$$\xi(y) = \sum_{i=1}^{\infty} b_i X_i$$

$$\frac{My^2}{2YI} = \sum_{i=1}^{\infty} b_i X_i$$

$$X_i = (cos(k_i y) - cosh(k_i y) - \alpha_i (sin(k_i y) - sinh(k_i y)))$$

$$\int_0^L \frac{My^2}{2YI} X_j dy = \int_0^L \sum_{i=1}^{\infty} b_i X_i X_j dy$$

$$\int_0^L \frac{My^2}{2YI} X_j dy = \sum_{i=1}^{\infty} b_i \int_0^L X_i X_j dy;\ \mathrm{i} = \mathrm{j}$$

$$\int_0^L \frac{My^2}{2YI} X_j dy = b_i L$$

$$b_i = \int_0^L \frac{My^2}{2YIL} X_j dy$$

Solving the integral

$$b_i = \frac{M}{2YIL} \int_0^L y^2 (\cos(k_i y) - \cosh(k_i y) - \alpha_i (\sin(k_i y) - \sinh(k_i y)))\, dy$$

$$\begin{aligned} b_i = \frac{-ML^3}{2YIL} \Bigg[& \frac{(k_i L)^2 (\sinh(k_i L) - \sin(k_i L) - \alpha_i \cos(k_i L) - \alpha_i \cosh(k_i L))}{(k_i L)^3} \\ & \frac{+(2k_i L)(\alpha_i \sin(k_i L) + \alpha_i \sinh(k_i L) - \cos(k_i L) - \cosh(k_i L))}{(k_i L)^3} \\ & \frac{+2(\sin(k_i L) + \sinh(k_i L) + \alpha_i \cos(k_i L) - \alpha_i \cosh(k_i L))}{(k_i L)^3} \Bigg] \end{aligned}$$

$$\begin{aligned} b_i = \frac{-ML^2}{2YI} \Bigg[& \frac{(k_i L)^2 (\sinh(k_i L) - \sin(k_i L) - \alpha_i \cos(k_i L) - \alpha_i \cosh(k_i L))}{(k_i L)^3} \\ & \frac{+(2k_i L)(\alpha_i \sin(k_i L) + \alpha_i \sinh(k_i L) - \cos(k_i L) - \cosh(k_i L))}{(k_i L)^3} \\ & \frac{+2(\sin(k_i L) + \sinh(k_i L) + \alpha_i \cos(k_i L) - \alpha_i \cosh(k_i L))}{(k_i L)^3} \Bigg] \end{aligned}$$

The bracket term in the above equation can be reduced using by substituting in for $\alpha_i = \frac{cosh(k_i L)+cos(k_i L)}{sinh(k_i L)+sin(k_i L)}$ and using equation (2.18), yielding the following expression for b_i:

$$b_i = \frac{-ML^2}{2YI} \left(\frac{4\sin(k_i L)\sinh(k_i L)}{(\sinh(k_i L) + \sin(k_i L))(k_i L)^3} \right)$$

i	k_iL	Sum
1	1.875104069	.4453858680
2	4.69409133	.3938696986e-1
3	7.85475748	.8247545876e-2
4	10.99554073	.3009018002e-2
5	14.13716839	.1415702726e-2
6	17.27875953	.7753938212e-3
7	20.42035225	.4697537992e-3
8	23.56194490	.3057923260e-3
9	26.70353756	.2100649514e-3
10	29.84513021	.1504664095e-3

Table 3.3: Sum part of equation (3.14) evaluated at the first 10 cantilever modes

The general expression for deflection is:

$$\xi(y) = \frac{-ML^2}{2YI}\sum_{i=1}^{\infty}\left(\frac{4\sin(k_iL)\sinh(k_iL)}{(\sinh(k_iL)+\sin(k_iL))(k_iL)^3}\right)(\cos(k_iy)-\cos(k_iy)-\alpha_i(\sin(k_iy)-\sinh(k_iy)))$$

Solving this expression for $y = L$

$$\xi(L) = \frac{-ML^2}{YI}\sum_{i=1}^{\infty}\left(\frac{2\sin(k_iL)\sinh(k_iL)}{(\sinh(k_iL)+\sin(k_iL))(k_iL)^3}\right)(\cos(k_iL)-\cos(k_iL)-\alpha_i(\sin(k_iL)-\sinh(k_iL)))$$

$$\xi(L) = \frac{-ML^2}{YI}\sum_{i=1}^{\infty}\frac{4}{(k_iL)^3}\left(\frac{\sin(k_iL)^2\sinh(k_iL)\cosh(k_iL)}{(\sinh(k_iL)+\sin(k_iL))^2}-\frac{\sinh(k_iL)^2\sin(k_iL)\cos(k_iL)}{(\sinh(k_iL)+\sin(k_iL))^2}\right) \tag{3.14}$$

Virtual Work Method

Equation (2.22) is the same as equation (3.14), derived above. Considering the sum part of the equation, noticing that it is independent of device dimensions, its value is 0.5. The values for the sum part of equation (3.14) for the first ten cantilever modes are given in table (3.3).

Simplifying equation (3.14) yields equation (3.15) which is similar to the parabolic tine tip deflection equation (3.11). The tip deflection changes linearly with applied potential and piezoelectric constant and changes as the square of length.

$$\xi(L) = \frac{-ML^2}{YI}\sum_{i=1}^{\infty}\frac{4}{(k_iL)^3}\left(\frac{\sin(k_iL)^2\sinh(k_iL)\cosh(k_iL)}{(\sinh(k_iL)+\sin(k_iL))^2}-\frac{\sinh(k_iL)^2\sin(k_iL)\cos(k_iL)}{(\sinh(k_iL)+\sin(k_iL))^2}\right)$$

$$\xi(L) = \frac{-ML^2}{YI}(Sum)$$

$$\xi(L) = \frac{4e_{21}V_oH^2L^2}{Y\left(\frac{1}{12}(H)(2W)^3\right)}\sum_n C_n(Sum)$$

$$\xi(L) = \frac{6e_{21}V_oHL^2}{YW^3}\sum_n C_n(Sum)$$

Fork Size	*Analytical Deflection* $\xi(y)$ (m)	*Ansys Deflection* $\xi(y)$ (m)
Large	3.40×10^{-11}	3.40×10^{-11}
Medium	5.77×10^{-11}	5.71×10^{-11}
Small	9.29×10^{-11}	9.15×10^{-11}

Table 3.4: Comparison between analytical and simulation results

$$\xi(L) = \frac{6e_{21}V_oHL^2}{YW^3}\sum_n C_n \quad (0.5)$$

$$\xi(L) = \frac{3e_{21}V_oHL^2}{YW^3}\sum_n C_n \quad (3.15)$$

Table (3.4) is a comparison between the analytical and simulated deflection for all three QTF sizes. The simulation package used is Ansys. As is seen the analytical and simulated results are in good agreement, i.e. maximum error of 1.51%. The applied potential is 0.1 V. Generally speaking, as the size decreases the amount of deflection increases.

3.3.2 Dielectric and Piezoelectric Charge

Equation (2.36) is the general expression for calculating charge on the electrodes due to inverse piezoelectric effect and the dielectric. Expressing this equation for the QTF case results in equation (3.16). The charge is calculated over one electrode. This value must be multiplied by 2 because 2 electrodes drive the device and 2 are used for detecting. In the actual device this value must be multiplied by 4, because charges from four plates are measured. The piezoelectric charge is first calculated then the dielectric.

$$Q = \int_o^L \int_o^H e_{21}\varepsilon_y dzdy + \int_o^L \int_o^H \varepsilon_r\varepsilon_o E_x(W,z)\, dzdy \quad (3.16)$$

3.3.2.1 Piezoelectric Charge

$$Q = \int_o^L \int_o^H e_{21}\varepsilon_y dzdy$$

$$Q = \int_o^L \int_o^H e_{21}x\frac{\partial^2\xi}{\partial y^2}dzdy$$

$$Q = xe_{21}\int_o^L \int_o^H \frac{\partial^2\xi}{\partial y^2}dzdy$$

where $x = \frac{W_o}{2}$ is the distance from the neutral axis, i.e. position of largest strain

$$Q = \frac{W_o}{2}e_{21}H\frac{\partial\xi}{\partial y}|_{y=L}$$

where $\frac{\partial\xi}{\partial y}$ - can be represented either by the parabolic approximation or the cantilever mode shape

Parabolic Approximation

Using the parabolic deflection equation the equation for charge is (3.17) and is derived as follows:.

$$\xi(y) = \xi_o\left(\frac{y}{L}\right)^2$$

$$\frac{\partial \xi(y)}{\partial y}|_{y=L} = \frac{2\xi_o L}{L^2} = \frac{2}{L^2}\frac{ML^2 L}{2YI} = \frac{ML}{YI}$$

$$Q = \frac{W_o}{2} e_{21} H \frac{\partial \xi}{\partial y}|_{y=L}$$

$$Q = \frac{W_o}{2} e_{21} H \frac{ML}{YI}$$

$$Q = e_{21}(W_o HL)\left[\frac{M}{2YI}\right]$$

Multiplying by 2

$$Q = e_{21}(W_o HL)\left[\frac{M}{YI}\right]$$

$$Q = e_{21}(W_o HL)\left[\frac{6\varepsilon_{21} V_o H \sum_n C_n}{W^3 Y}\right]$$

$$Q = \frac{12 e_{21}^2 V_o H^2 L \sum_n C_n}{YW^2} \tag{3.17}$$

$$Q = \frac{12 d_{21}^2 Y V_o H^2 L \sum_n C_n}{W^2} \tag{3.18}$$

Cantilever Approximation

Using equation (2.21), evaluated at $y_1 = L$, for the deflection of a beam the equation for charge is (3.19) and is derived as follows:

$$\xi(y) = \frac{ML^2}{YI}\sum_{i=1}^{\infty}\left[\frac{(\cos(k_i y) - \cosh(k_i y) - \alpha_i(\sin(k_i y) - \sinh(k_i y)))}{(k_i L)^3}\right.$$
$$\left.\frac{(-\sin(k_i L) - \sinh(k_i L) - \alpha_i(\cos(k_i L) - \cosh(k_i L)))}{(k_i L)^3}\right]$$

$$b_i = \frac{ML^2}{YI}\frac{(-\sin(k_i L) - \sinh(k_i L) - \alpha_i(\cos(k_i L) - \cosh(k_i L)))}{(k_i L)^3}$$

$$X_i = (\cos(k_i y) - \cosh(k_i y) - \alpha_i(\sin(k_i y) - \sinh(k_i y)))$$

$$\xi(y) = \sum_{i=1}^{\infty} b_i X_i$$

$$\frac{\partial \xi(y)}{\partial y} = \sum_{i=1}^{\infty} b_i \frac{\partial X_i}{\partial y}$$

$$\frac{\partial \xi(y)}{\partial y} = \sum_{i=1}^{\infty} b_i \frac{\partial((\cos(k_i y) - \cosh(k_i y) - \alpha_i(\sin(k_i y) - \sinh(k_i y))))}{\partial y}$$

$$\frac{\partial \xi(y)}{\partial y} = \sum_{i=1}^{\infty} b_i k_i(-\sin(k_i y) - \sinh(k_i y) - \alpha_i(\cos(k_i y) - \cosh(k_i y)))$$

$$\frac{\partial \xi(y)}{\partial y} = \frac{ML^2}{YI}\sum_{i=1}^{\infty}\left[\frac{k_i\left(-\sin(k_iy)-\sinh(k_iy)-\alpha_i\left(\cos(k_iy)-\cosh(k_iy)\right)\right)}{(k_iL)^3}\right.$$
$$\left.\frac{\left(-\sin(k_iL)-\sinh(k_iL)-\alpha_i\left(\cos(k_iL)-\cosh(k_iL)\right)\right)}{(k_iL)^3}\right]$$

$$\frac{\partial \xi(y)}{\partial y} = \frac{ML}{YI}\sum_{i=1}^{\infty}\left[\frac{(k_iL)\left(-\sin(k_iy)-\sinh(k_iy)-\alpha_i\left(\cos(k_iy)-\cosh(k_iy)\right)\right)}{(k_iL)^3}\right.$$
$$\left.\frac{\left(-\sin(k_iL)-\sinh(k_iL)-\alpha_i\left(\cos(k_iL)-\cosh(k_iL)\right)\right)}{(k_iL)^3}\right]$$

$$\frac{\partial \xi(y)}{\partial y} = \frac{ML}{YI}\sum_{i=1}^{\infty}\left[\frac{\left(-\sin(k_iy)-\sinh(k_iy)-\alpha_i\left(\cos(k_iy)-\cosh(k_iy)\right)\right)}{(k_iL)^2}\right.$$
$$\left.\frac{\left(-\sin(k_iL)-\sinh(k_iL)-\alpha_i\left(\cos(k_iL)-\cosh(k_iL)\right)\right)}{(k_iL)^2}\right]$$

$$\frac{\partial \xi(y)}{\partial y}|_{y=L} = \frac{ML}{YI}\sum_{i=1}^{\infty}\left[\frac{\left(-\sin(k_iL)-\sinh(k_iL)-\alpha_i\left(\cos(k_iL)-\cosh(k_iL)\right)\right)}{(k_iL)^2}\right.$$
$$\left.\frac{\left(-\sin(k_iL)-\sinh(k_iL)-\alpha_i\left(\cos(k_iL)-\cosh(k_iL)\right)\right)}{(k_iL)^2}\right]$$

$$\frac{\partial \xi(y)}{\partial y}|_{y=L} = \frac{ML}{YI}\sum_{i=1}^{\infty}\frac{4}{(k_iL)^2}\left(\frac{\sin(k_iL)\sinh(k_iL)}{\sinh(k_iL)+\sin(k_iL)}\right)^2$$

$$Q = \frac{W_o}{2}e_{21}H\frac{\partial \xi}{\partial y}|_{y=L}$$

$$Q = \frac{W_o}{2}e_{21}H\left(\frac{ML}{YI}\sum_{i=1}^{\infty}\frac{4}{(k_iL)^2}\left(\frac{\sin(k_iL)\sinh(k_iL)}{\sinh(k_iL)+\sin(k_iL)}\right)^2\right) \tag{3.19}$$

Considering the sum part of the equation, noticing again that it is independent of device dimensions, its value is 1. The values for the sum part of equation (3.19) for the first ten cantilever modes are given in table (3.5).

Simplifying equation (3.19) yields equation (3.20) which is similar to the parabolic charge deflection equation (3.17). Therefore the piezoelectric charge changes linearly with applied potential but unlike the deflection case changes as the squared of the piezoelectric constant term and linearly in length.

$$Q = \frac{W_o}{2}e_{21}H\left(\frac{ML}{YI}\sum_{i=1}^{\infty}\frac{1}{(k_iL)^2}\left(\frac{\sin(k_iL)\sinh(k_iL)}{\sinh(k_iL)+\sin(k_iL)}\right)^2\right)$$

$$Q = \frac{e_{21}MWHL}{YI}(Sum)$$

i	k_iL	Sum
1	1.875104069	.6130760896
2	4.69409133	.1883003453
3	7.85475748	.6473223092e-1
4	10.99554073	.3308689030e-1
5	14.13716839	.2001399883e-1
6	17.27875953	.1339784424e-1
7	20.42035225	.9592538040e-2
8	23.56194490	.7205061948e-2
9	26.70353756	.5609477292e-2
10	29.84513021	.4490689580e-2

Table 3.5: Sum part of equation (3.19) evaluated at the first 10 cantilever modes

$$Q = \frac{12e_{21}^2 V_o H^2 L \sum_n C_n}{YW^2} (Sum)$$

$$Q = \frac{12e_{21}^2 V_o H^2 L \sum_n C_n}{YW^2} \tag{3.20}$$

3.3.2.2 Dielectric Charge

$$Q = \varepsilon_r \varepsilon_o \int_o^L \int_o^H E_x(W,z)\, dzdy$$

Evaluating the integral part:

$$\int_o^L \int_o^H E_x(W,z)\, dzdy = \int_o^L \int_o^H -4V_o \sum_{n=odd} \left[\frac{\sinh\left(\frac{n\pi W}{H}\right) \sin\left(\frac{n\pi z}{H}\right)}{H \cosh\left(\frac{n\pi W}{H}\right)} \right] dzdy$$

$$= 4V_o \sum_{n=odd} \int_o^L \left[\frac{\sinh\left(\frac{n\pi W}{H}\right) (\cos(n\pi) - 1)}{\cosh\left(\frac{n\pi W}{H}\right) n\pi} \right] dy$$

$$= 4V_o \sum_{n=odd} \left[\frac{\sinh\left(\frac{n\pi W}{H}\right) (\cos(n\pi) - 1) L}{\cosh\left(\frac{n\pi W}{H}\right) n\pi} \right]$$

$$= 4V_o L \sum_{n=odd} \left[\frac{\sinh\left(\frac{n\pi W}{H}\right) (\cos(n\pi) - 1)}{\cosh\left(\frac{n\pi W}{H}\right) n\pi} \right]$$

$$Q = 4\varepsilon_r \varepsilon_o V_o L \sum_{n=odd} \left[\frac{\sinh\left(\frac{n\pi W}{H}\right) (\cos(n\pi) - 1)}{\cosh\left(\frac{n\pi W}{H}\right) n\pi} \right]$$

Multiplying by 2:

$$Q = 8\varepsilon_r \varepsilon_o V_o L \sum_{n=odd} \left[\frac{\sinh\left(\frac{n\pi W}{H}\right) (\cos(n\pi) - 1)}{\cosh\left(\frac{n\pi W}{H}\right) n\pi} \right] = 8\varepsilon_r \varepsilon_o V_o L a_n \tag{3.21}$$

The sum term in equation (3.21) for all three sizes is given in table (3.6) and is plotted in figure (3.10). The values are independent of size.

Table (3.7) is a comparison between the analytical and simulated charge, piezoelectric and dielectric, for all three QTF sizes. As stated above, the simulation package used is Ansys and the

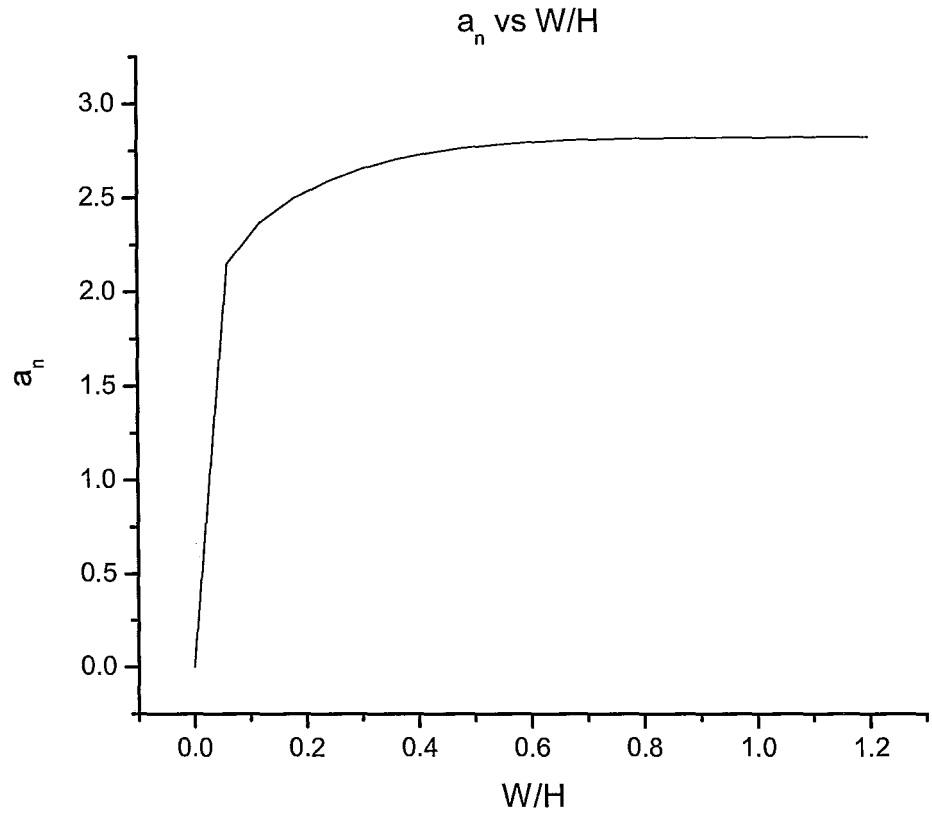

Figure 3.10: Plot of $a_n$vs $\frac{W}{H}$ for equation (3.21)

Size	W (m)	H (m)	$\frac{W}{H}$	*Sum*
Large	2.90×10^{-4}	2.80×10^{-4}	1.04	2.82
Medium	1.80×10^{-4}	2.40×10^{-4}	0.64	2.81
Small	1.20×10^{-4}	1.20×10^{-4}	1.00	2.82

Table 3.6: Sum part of equation (3.21) evaluated for the three sizes of QTF

Size	*Piezoelectric Analytical Charge (C)*	*Dielectric Analytical Charge (C)*	*Piezoelectric Simulated Charge (C)*	*Dielectric Simulated Charge (C)*
Large	1.13×10^{-16}	3.33×10^{-13}	7.91×10^{-17}	2.98×10^{-13}
Medium	1.17×10^{-16}	2.86×10^{-13}	7.19×10^{-17}	2.52×10^{-13}
Small	7.90×10^{-16}	2.27×10^{-13}	5.51×10^{-16}	1.94×10^{-13}

Table 3.7: Comparison of analytical and simulated piezoelectric and dielectric charge for the three sizes of QTF

Size	*Frequency (Hz)*	*Piezoelectric Capacitance (F)*	*Inductance (H)*	*Dielectric Capacitance (F)*
Large	31,067.53	2.26×10^{-15}	11,612.30	6.66×10^{-12}
Medium	35,848.25	2.34×10^{-15}	8424.83	5.72×10^{-12}
Small	28,368.98	1.58×10^{-15}	19,920.29	4.54×10^{-12}

Table 3.8: Theoretical frequency, inductance and capacitance for the three sizes of QTF

conditions used are the same as above. The discrepancy in the dielectric and piezoelectric charge is due to meshing. Using both COMSOL and Ansys the mesh density has to be fine for electrostatic simulations. Comparing the analytical summation terms equations (3.11) and (3.21), for the electrical case more than a 1000 terms has to summed to yield a steady result. For the deflection less than 100 terms has to be used.

Using equation (2.19), table (2.1) and equation (2.39) the theoretical resonance frequency at the fundamental mode, the inductance for the three sizes of the QTFs is given in table (3.8) for a drive voltage of 0.1 V_{rms}. The values for the piezoelectric capacitance is calculated from the piezoelectric charge, table (3.7), divided by the drive voltage and multiplied by two for the QTF case, i.e. two tines therefore double the charge. The density is 2650 kg/m^3[10], modulus of elasticity is 102.59 GPa[2] and the dimensions are given table (3.1).

3.4 Experimental Setup and Results

This section describes the experimental setup used and the associated results of measured frequency, capacitance, inductance, resistance, Q and thermal noise of the QTFs at the fundamental mode. The results of the measurements are also compared to the theoretical derived values. The dimensions of the fork, table (3.1), are measured using a microscope with a 50x magnification.

3.4.1 Experimental Setup

The experimental setup is designed for frequency sweeping experiments of the three QTFs. To aid in this, an HP 33120 A function generator, SR-830 lock-in amplifier and an Amptek A250 charge sensitive amplifier are used. The function generator synchronizes the lock-in amplifier while the lock-in amplifier's drive is used to drive the QTF. The signal from the QTF is amplified using the Amptek A250 amplifier. The output from the amplifier is fed into the input of the SR844 lock-in. The setup is illustrated in figure (3.11). The computer in the setup is used to control the function generator and SR-830 and record the results from SR-830. This is done using Labview. A drive voltage of 100 - 4 mVrms is used and the associated voltage is recorded. Figure (3.12) is the setup used to measure the QTF noise. The difference between the two setups is the QTF is not driven, i..e. grounded.

[2] *The modulus of elasticity is calculated from Ansys.*

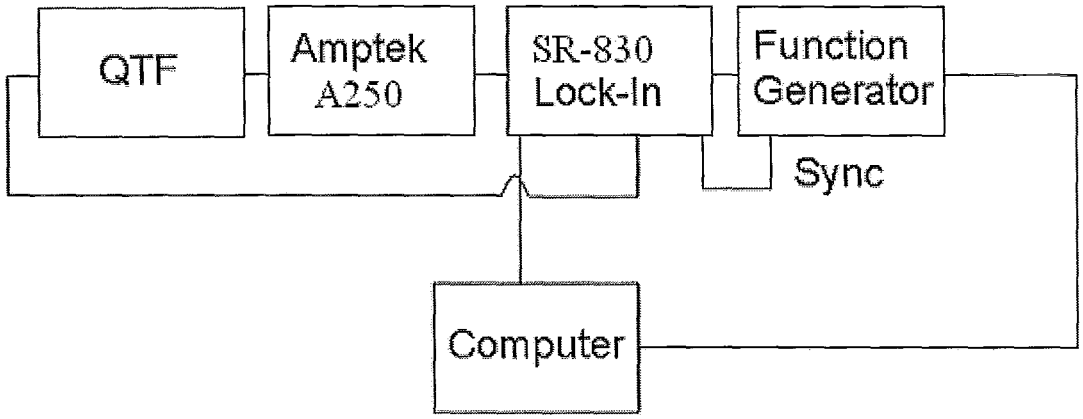

Figure 3.11: Experimental setup for QTF. The function generator syncs the lock-in amplifier, SR-830, which drives the QTF. The charge from the QTF is amplified by Amptek A250 and is detected by SR-830. Data is recorded on the computer. The setup is controlled by Labview

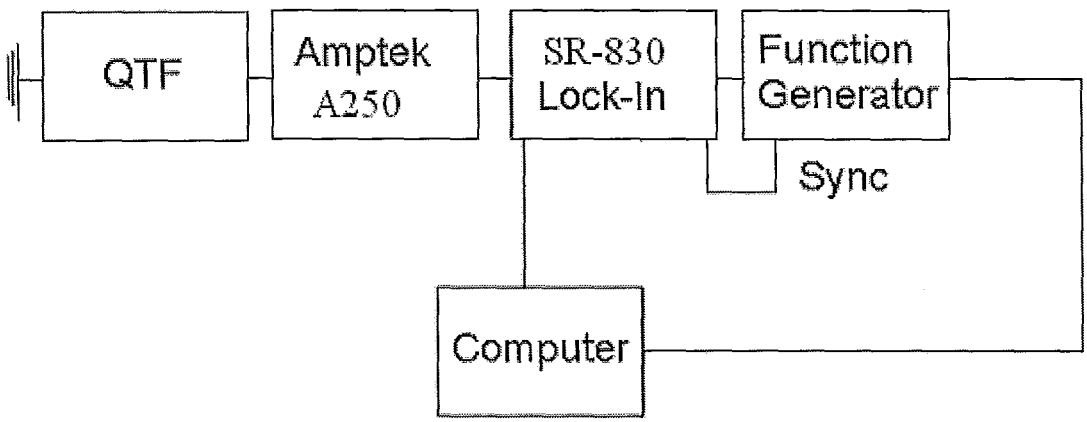

Figure 3.12: Experimental setup for QTF noise. Similar setup as above with the change being the QTF is grounded

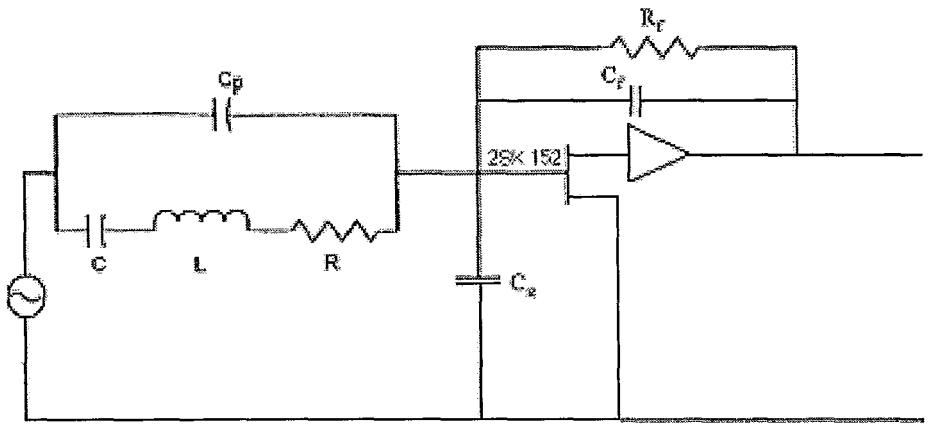

Figure 3.13: Equivalent electrical circuit for QTF and Amptek A250

3.4.2 Results

In order to relate the measured voltage to the intrinsic impedance of the resonator the equivalent circuit of the system, i.e. the QTF and Amptek A250, must be analyzed, figure (3.13). Through circuit analysis the voltage gain of the system is given by equation (3.22), where R_f and C_f are the feedback resistance and capacitance and have values of $300\,M\Omega$ and $1.0\,pF$, respectively. Equation (3.23) is the feedback impedance of this circuit.

$$V_{out} = \frac{V_{IN}R_F\sqrt{1-2w^2LC_p+2C_p/C+(wC_pR)^2+(w^2LC_p)^2-2w^2LC_p^2/C+(C_p/C)^2}}{\sqrt{R^2+(wL)^2-2L/C+1/(wC)^2+(wC_fR_fR)^2+(w^2C_fR_FL)^2-2(wC_fR_f)^2L/C+(C_fR_f/C)^2}} \tag{3.22}$$

$$Z_f = \frac{R_f}{\sqrt{1+(wR_fC_f)^2}} \tag{3.23}$$

Figure (3.14) is a plot of the measured impedance vs frequency for the three QTFs and is similar to the theoretically expected result, figure (2.10). Using the equation for $Q = \frac{1}{w_r RC}$, (2.44), (2.41) (2.39) and $X_{C_p} = 1/wC_p$ the experimental values for Q, RLC and C_p for the three sizes of QTFs are calculated and given in table (3.9). The resonance frequency, f_r, is read off the plot. The Q-value for the devices are in the medium to high range, which is as expected. The resonant frequency remains the same between the three and the piezoelectric capacitance decreases with size.

Comparing the analytical, table (3.8), and experimental values, table (3.9), generally the analytical results agree well with the experimental results. The measured frequency differs by at most 13.42% from the theoretical result. This is attributed to inexact measurements of the tine length, width and thickness. The measured package capacitance is about an order of magnitude lower than the analytical result. This is attributed to the edge effects of the electrodes on the tines. In the above derivation for package capacitance the electrodes are assumed to be the same dimension as the width and thickness of the tine. In the actual device the electrodes do not extend to the entire width or thickness of the tine.

	Large	*Medium*	*Small*
Q	102,387.19	65,529.10	81,912.38
$f_r\ (Hz)$	32,763.88	32,764.55	32,764.95
$R\,(\Omega)$	23,283.35	40,240.26	38,481.06
$L\,(H)$	11,580.20	12,808.87	15,311.12
$C\,(F)$	2.03e-15	1.84e-15	1.54e-15
$C_p\,(F)$	8.50e-13	9.38e-13	7.38e-13

Table 3.9: Experimentally determined values of Q, f_r, RLC and C_p

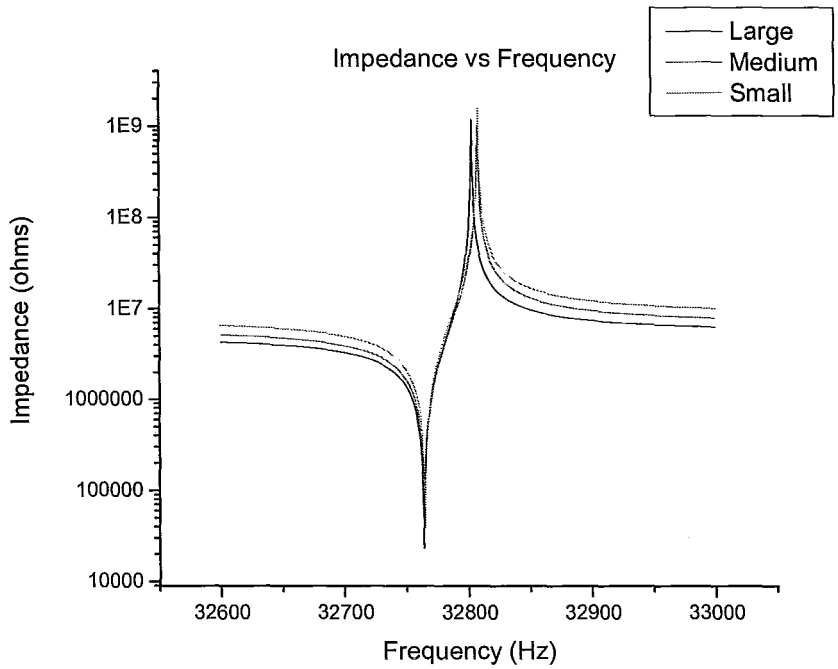

Figure 3.14: Impedance vs Frequency for three sizes of QTF. The lowest impedance is the resonance mode, highest impedance in the anti-resonance mode and the impedance of the tails are due to package capacitance.

Noise

The thermal noise due to the resistance in the QTF is the dominant source of noise as reported by[19]. This serves as the fundamental limit in measuring the resonance of QTF. Figure (3.12) is the experimental setup used, to verify this assertion. The equivalent circuit of a grounded QTF is shown in figure (3.15).

From circuit theory the noise sources are: johnson noise due to the resonant resistance of the QTF, feedback resistance of the op-amp and shot noise of the JFET. Johnson noise is given by equation (3.24)[25] and the shot noise of the JFET is $1\frac{nV}{\sqrt{Hz}}$[26]. The output noise due to the three sources are given by equations (3.25)-(3.27). V_1 is the output noise due to R of the QTF, V_2 is the output noise due to JFET and V_3 is the output noise due to feedback resistance, R_f. These three terms add in quadrature to give the total noise.

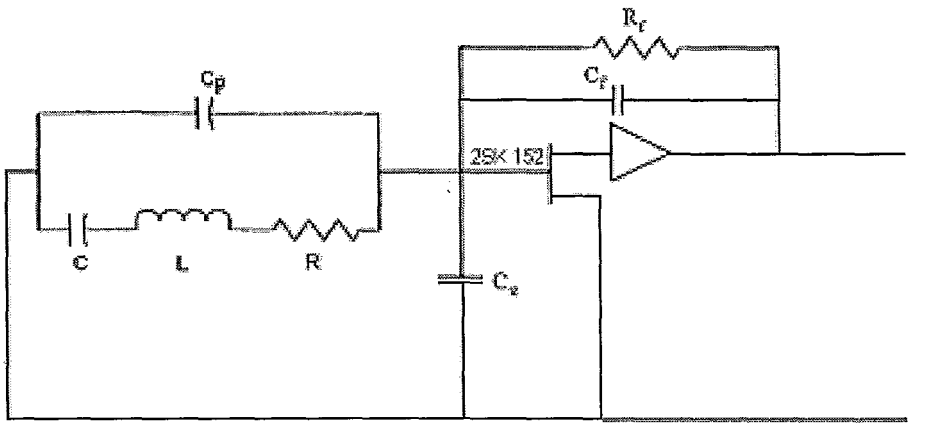

Figure 3.15: Equivalent electrical circuit for grounded QTF and Amptek A250

$$\frac{V_T}{\sqrt{f}} = \sqrt{4K_BTR} \tag{3.24}$$

$$V_1 = \frac{\sqrt{4K_BTR}R_f}{\sqrt{1+(wC_fR_f)^2}\sqrt{R^2+(1/(wc)^2)-(2L/C)+(wL)^2}} \tag{3.25}$$

$$V_2 = \frac{(1.0e-9)R_f\sqrt{1+2C_p/C-2w^2LC_p+(RwC_p)^2+(C_p/C)^2-2(C_pw)^2L/C+(w^2LC_p)^2}}{\sqrt{1+(wC_fR_f)^2}\sqrt{R^2+(1/(wC)^2)-(2L/C)+(wL)^2}} \tag{3.26}$$

$$V_3 = \frac{\sqrt{4K_BTR_f}}{\sqrt{1+(wC_fR_f)^2}} \tag{3.27}$$

Figure (3.16) is a plot of the measured and the theoretical noise of the large fork at the fundamental mode. The other tuning forks were not measured because of the time taken for such measurements. For the large fork this is 168 hrs. As is seen from this plot there is a strong agreement between the experimental and theoretical results. The theoretical results are generated using the experimental RLC and $C_p$values. To analyze the contribution of each noise source, figure (3.17) is a plot of equations (3.25)-(3.27) and their quadrature. This plot indicates that the dominant source of noise is the resonant resistance, R. The baseline noise in figure (3.17) is due to the feedback impedance, mainly due to the feedback capacitance, C_f.

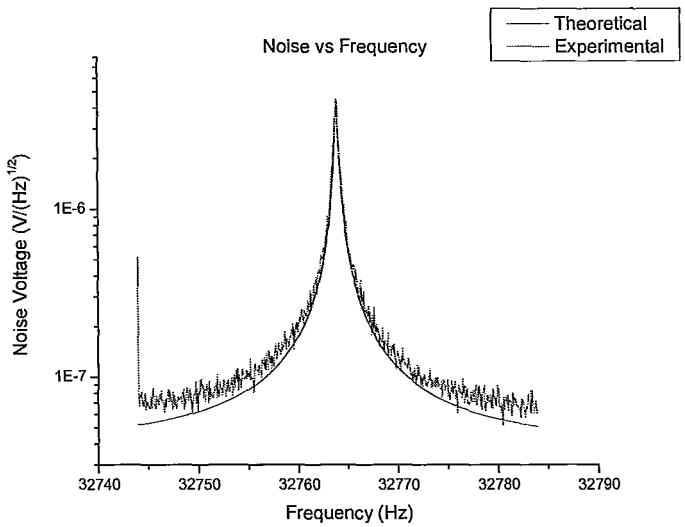

Figure 3.16: Experimental and theoretical noise voltage vs frequency. The experimental and theoretical results are in good agreement.

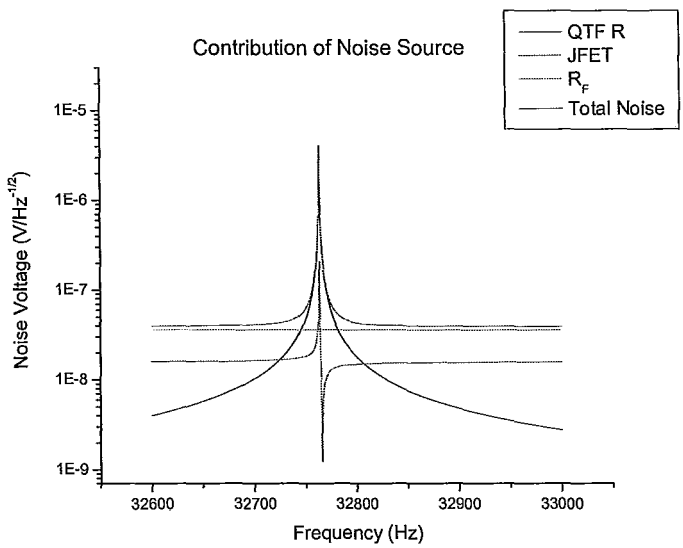

Figure 3.17: Theoretical plot of equations (3.25)-(3.27) and their quadrature

Chapter 4

3-Terminal System

In the previous section the drive and detect of a 2-terminal device is presented. The problem with such a device is the impedance of the package capacitance, C_p, must be larger than the resonator's impedance. If this is not the case, the package capacitance must either be removed or its value decreased. While the former might be impossible the latter can be achieved by designing electrodes and the associate detecting system so as to decrease this value. An example of such a system is a 3-terminal device. Here one terminal is used to drive the device, another to detect and the third one is ground. Therefore the package capacitance can be chosen to either terminal, i.e. detect to ground or detect to drive.

In this section the theory and simulated results of a 3-terminal device is presented.

4.1 Theory

Figure (4.1) illustrates a possible 3-terminal device. Here, 1 is the drive electrode, 2 is the detect electrode and 3, connected at either ends, the ground electrode. If electrodes 1 and 2 are connected the device becomes a 2-terminal device, similar to the QTF presented in the previous section. For the simulation presented quartz piezoelectric coefficient and geometry of large QTF is used.

The equivalent circuit for such a system is presented in figures (4.2) and (4.3). The former is for the non-piezoelectric case while the latter is for the piezoelectric case. In both these cases the package capacitance is between terminals 1 and 2. The piezoelectric capacitance is assumed to be parallel to the package capacitance. The output voltage measured from the drive with respect to ground is given in equations (4.1) and (4.2) for the non-piezoelectric and piezoelectric case.

$$\frac{V_{O/P}}{V_{I/P}} = \frac{C_1}{C_1 + C_0} \tag{4.1}$$

$$\frac{V_{O/P}}{V_{I/P}} = \frac{C_1 + C_m}{C_1 + C_0 + C_m} \tag{4.2}$$

4.2 Simulation Results

First the non-piezoelectric case is considered then the piezoelectric case.

4.2.1 Non-Piezoelectric

To verify the non-piezoelectric circuitry the values of the capacitances are first extracted in Ansys using the treffetz domain method, table(4.1). The treffetz domain method extracts capacitances

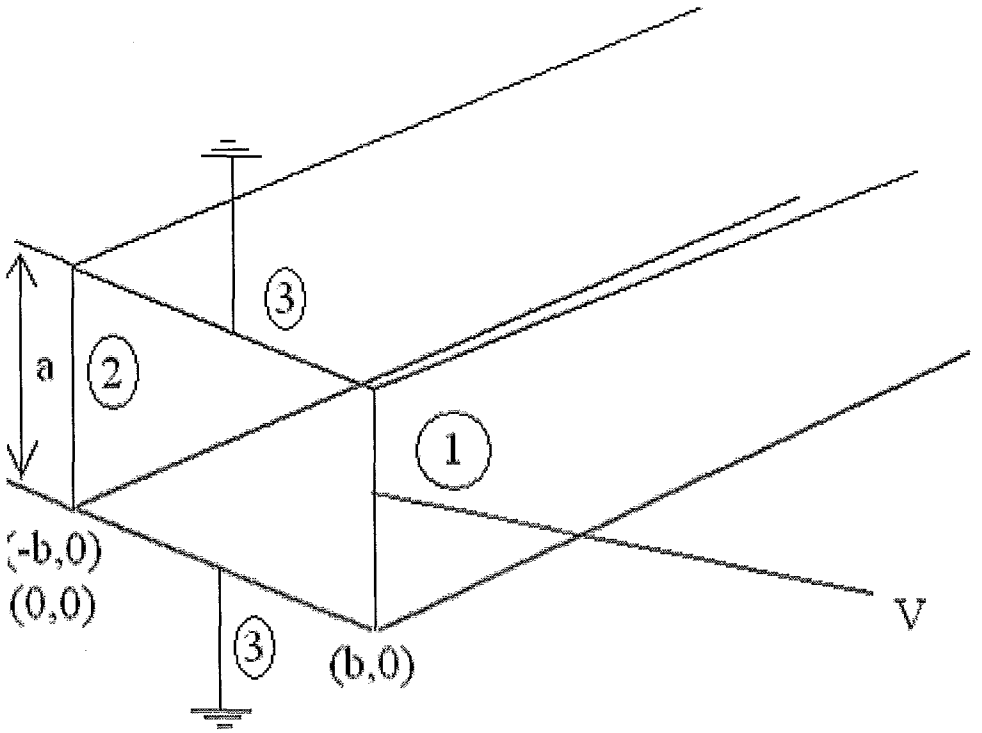

Figure 4.1: 3-Terminal electrode geometry. Terminal 1 is drive, 2 is detect and 3 is ground

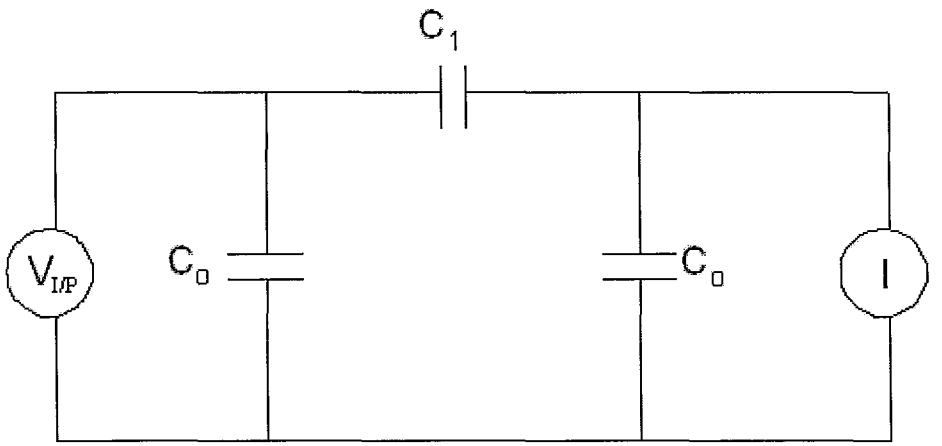

Figure 4.2: Equivalent circuit for non-piezoelectric case. C_1 - package capacitance and C_0 - capacitance to ground

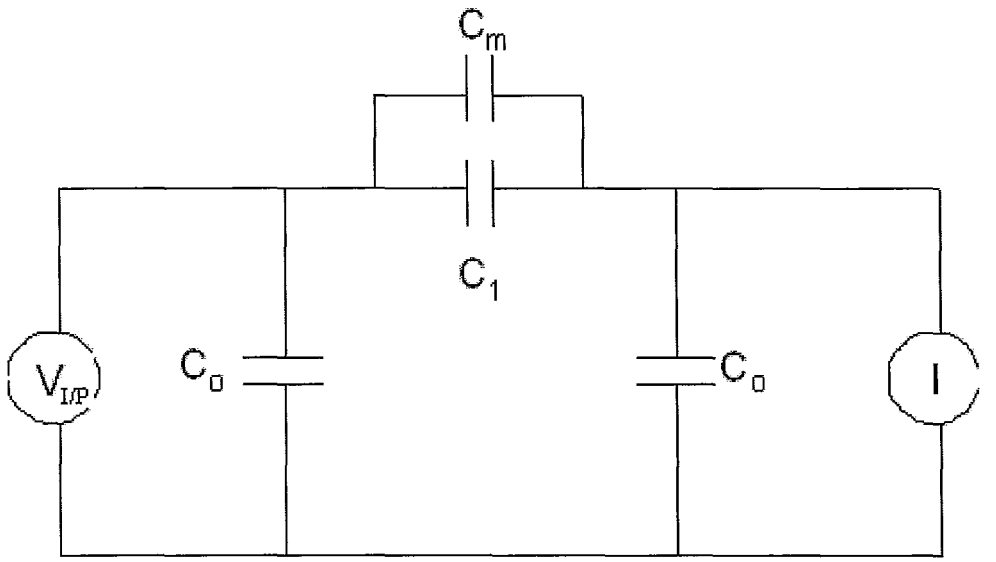

Figure 4.3: Equivalent circuit for piezoelectric case. C_1 - package capacitance, C_m - piezoelectric capacitance and C_0 - capacitance to ground

1&3 C_0 (pF)	2&3 C_0 (pF)	1&2 C_1 (fF)
0.8993	0.8993	1.1205

Table 4.1: Capacitance values between terminals

based on the geometry and position of the electrodes. The capacitance between terminals 1&3 are equivalent to 2&3 which is expected because they share similar geometry. A 2nd simulation is done where $1.0\,V$ is applied to terminal 1, terminal 3 is grounded and a voltage is measured from terminal 2 is $9.98 \times 10^{-4}\,V$. Using the equation(4.1) and the capacitance values from table (4.1) the output voltage is $1.24 \times 10^{-3}\,V$ which is 19.52% greater than the measured voltage. The reason for this discrepancy could be coarse mesh, capacitance derived from the treffetz method could be mesh independent etc. The amount of error is deemed acceptable therefore the circuit is held to be true.

4.2.2 Piezoelectric

Unlike the previous case the treffetz domain method cannot be used to extract the piezoelectric capacitance. As a result the circuit in figure (4.3) and its associated equation (4.2) is assumed true. To verify this, a similar simulation as above, i.e. applying $1.0\,V$ to terminal 1 and measuring the output voltage from terminal 2 while holding terminal 3 to ground, is done for different piezoelectric stress coefficients, e. From equation (4.2) the piezoelectric capacitance is calculated. From equation (3.18) the charge or capacitance is known to vary as e^2. The calculated piezoelectric capacitance and the piezoelectric stress coefficients used is given in table (4.2). As is seen, the capacitance varies as $2e^2$ when comparing $e = 0.171$ and $e = 1.710$ while the capacitance varies approximately as e^2 when comparing $e = 1.710$ and $e = 17.10$. .

$e\ \left(\frac{c}{m^2}\right)$	$C_m\ (F)$	$Change$
0.171	1.17150×10^{-16}	
1.710	2.2998×10^{-14}	196.31
17.10	2.81917×10^{-12}	122.58

Table 4.2: Piezoelectric capacitance to piezoelectric stress coefficient

Chapter 5

Indium Phosphide (InP) MEMS Resonator

InP is primarily used as a substrate for epitaxial growth to support InGaAsP lasers for optical fibre telecommunications and to fabricate InGaAs/AlInAs psuedomorphic high electron mobility transistors for microwave generation and amplification[27]. MEMS devices such as optical integrated stress sensors, optical modulators or switches, wavelength selective and tuneable filters etc have been proposed and fabricated in InP[28, 29]. These devices use electro-static force to cause actuation. InP MEMS using piezoelectricity has not been investigated. In general, very little is known about the piezoelectric property of InP. In fact its piezoelectric stress constant is still a matter of debate[30, 31]. Conversely, GaAs and AlGaAs MEMS devices using piezoelectric effect have been widely investigated[32, 33, 7].

This section begins with a discussion on the piezoelectric properties of InP. Using this piezoelectric relationship the design, theoretical and experimental results of InP MIS bridges is discussed.

5.1 Piezoelectric Properties

InP belongs to a class of crystals lacking a symmetry between the positive and negative ions of the crystal lattice. In this case, there is a tendency for the electron clouds to shift towards the phosphide atoms resulting in a dipole moment along the [111] axis, figure (5.1)[34] - the white circles are indium atoms and the grey circles are phosphide atoms. This deviation from inversion symmetry results in a non-vanishing piezoelectric coefficients.

To determine the piezoelectric coefficient the wafer orientation and the type of deformation needs to be considered. Figure (5.2) illustrates the coordinate system, the general form of the piezoelectric matrix and the type of deformation achieved. As stated in the theory section flexural vibrations are of interest, therefore d_{31} and d_{32} should be the largest coefficients.

The most common wafer orientation of InP is (100). For this wafer, [100] is the normal axis x_3 , $[0\bar{1}1]$ the x_1 axis ($\phi = 0$) and let ϕ be a rotation of the coordination system around the x_3-axis. Figure (5.3) is the reduced piezoelectric matrix for the (100) wafer orientation, where $\pm b_2$ is d_{31} and d_{32}. Here $b_2 = cos\,(2\phi)$ and $a_2 = sin\,(2\phi)$; therefore $\pm b_2$ is maximized if $(\phi = \frac{n\pi}{2})$ or the fabricated beam is along $\langle 011 \rangle$.The crystallographic coordinate system, i.e. [010], [001], is obtained by setting $(\phi = \frac{\pi}{4})$.

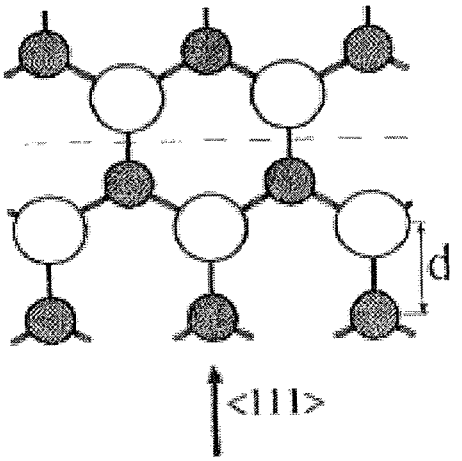

Figure 5.1: Schematic projection of atom in the [111] direction. White circles - indium atoms, grey circles - phosphide atoms[34]

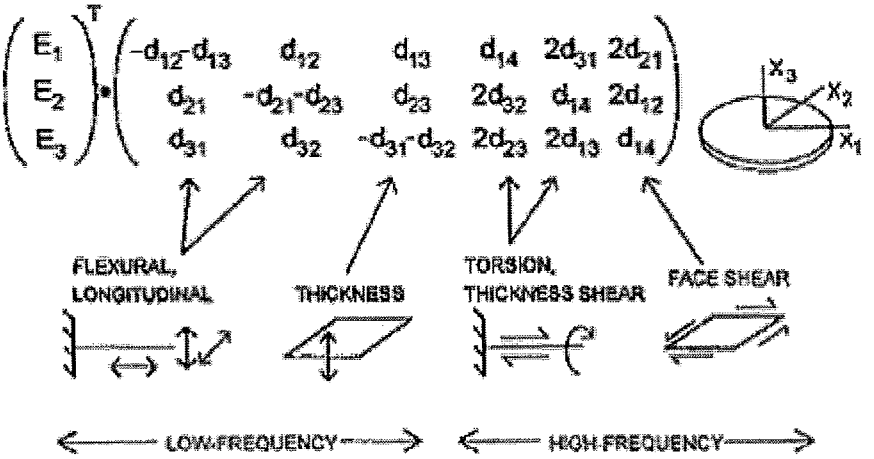

Figure 5.2: Piezoelectric matrix, d_{ik}, specialized to cubic system and definition of the coordinate system. Indicated are possible vibration modes for various electric field components[34]

$$d_{ik}(\phi) = \frac{d_{14}}{2}\begin{pmatrix} 0 & 0 & 0 & 2a_2 & -2b_2 & 0 \\ 0 & 0 & 0 & 2b_2 & 2a_2 & 0 \\ -b_2 & b_2 & 0 & 0 & 0 & 2a_2 \end{pmatrix}$$

Figure 5.3: Piezoelectric matrix for (100) wafer orientation. $b_2 = cos\,(2\phi)$ and $a_2 = sin\,(2\phi)$[34]

The piezoelectric and mechanical coefficients of InP are:

Modulus of Elasticity[35]:

$$Y^E_{pq} = \begin{bmatrix} 102.20 & 57.6 & 5.61 & 0 & 0 & 0 \\ 57.6 & 102.20 & 5.61 & 0 & 0 & 0 \\ 5.61 & 5.61 & 102.20 & 0 & 0 & 0 \\ 0 & 0 & 0 & 44.2 & 0 & 0 \\ 0 & 0 & 0 & 0 & 44.2 & 0 \\ 0 & 0 & 0 & 0 & 0 & 102.20 \end{bmatrix} GPa$$

Piezoelectric coefficient matrix[31]:

$$d_{iq} = \begin{bmatrix} 0 & 0 & 0 & 0 & -3.6 & 0 \\ 0 & 0 & 0 & 3.6 & 0 & 0 \\ 1.8 & 1.8 & 0 & 0 & 0 & 0 \end{bmatrix} = \begin{bmatrix} 0 & 0 & 1.8 \\ 0 & 0 & 1.8 \\ 0 & 0 & 0 \\ 0 & 3.6 & 0 \\ -3.6 & 0 & 0 \\ 0 & 0 & 0 \end{bmatrix} \frac{pm}{V}$$

Piezoelectric constant matrix[31]:

$$e_{iq} = \begin{bmatrix} 0 & 0 & 0.0307 \\ 0 & 0 & 0.0307 \\ 0 & 0 & 0 \\ 0 & 0 & 0 \\ 0 & -0.1227 & 0 \\ 0 & 0.1227 & 0 \end{bmatrix} \frac{c}{m^2}$$

Permittivity matrix[36]:

$$\varepsilon^E_{ik} = \begin{bmatrix} 12.4 & 0 & 0 \\ 0 & 12.4 & 0 \\ 0 & 0 & 12.4 \end{bmatrix}$$

5.2 Design

In order to induce piezoelectric property in InP it must be an insulator. There are two ways of achieving this: doping with iron or using its semiconductor property to create a depletion width. Here, the latter is chosen. The depletion width is used to induce piezoelectricity and control the thickness of this layer hence creating a monomorph. Control means the piezoelectric thickness, hence amount of deflection, can be changed by changing the width of the depletion region. To elucidate this idea the electrical design is first discussed then mechanical.

5.2.0.1 Electrical Design

Depletion widths are created using junctions – pn or hetero. A heterojunction is used in order to keep the layers as intrinsic as possible. Figure (5.4) is the schematic of the MBE grown structure which consists of three layers grown on an InP substrate. This structure is similar to the high responsivity InGaAs/InP- based MSM photodetector as reported by B. J. Robinson et al[37]. The first layer grown is a 4.0 μm thick $In_{0.53}Ga_{0.47}As$ sacrificial layer. The mechanical layer is the 1.67 μm thick InP layer. This layer in addition with the 100 Å $In_{0.85}Ga_{0.15}P$ layer forms the heterojunction. These layers are grown to be as intrinsic as possible, i.e. n+ doped with $2.0 \times 10^{21}\, m^{-3}$.

The depletion width of the heterojunction, $In_{0.85}Ga_{0.15}P$/InP, determined using equation (5.1)[36] and values from table (5.1), is 109.56 nm at 0 volts. Therefore $In_{0.85}Ga_{0.15}P$ is completely depleted and 99.56 nm of InP layer is also depleted. A depletion width is also created due to the surface state. Using equation (5.3) the depletion width is approximately 429.53 nm. To aid in increasing/controlling the depletion width Schottky contacts made from platinum/gold are grown on $In_{0.85}Ga_{0.15}P$. This results in a total depletion width of 517.20 nm equation (5.4) at 0 volts, increasing the depletion

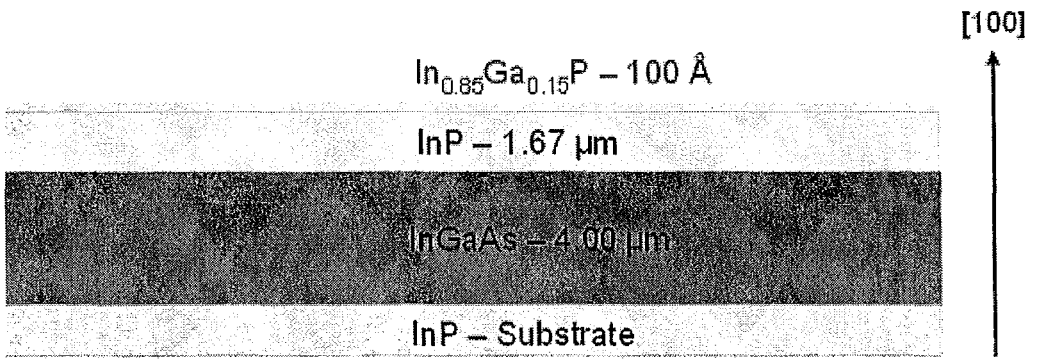

Figure 5.4: Schematic of MBE grown structure on an InP substrate

	Gold (Au)	InP	$In_{0.85}Ga_{0.15}P$
Work Function $\phi\,(eV)$	5.1	4.65[38]	4.685[38]
Carrier Concentration $N_d\,(m^{-3})$	1.0×10^{27}	2.0×10^{21}	2.0×10^{21}
Dielectric Constant ϵ_r	-	12.4	12.4
Bandgap $E_g\,(eV)$	-	1.35[38]	1.47[38]
Resistivity $\Omega - m$	2.44×10^{-8}[38]	1.4×10^{-3}	1.4×10^{-3}

Table 5.1: Material properties used for depletion width calculations

width by 4.7 times the heterojunction depletion width. Therefore 507.2 nm or 30.19% of InP is depleted. This is reminiscent of a MIS structure. The above depletion widths, mechanisms and percentage of depleted layer are summarized in table (5.2). The calculations are given in appendix A. In table (5.1) and for the depletion width calculation the dielectric constant and resistivity of $In_{0.85}Ga_{0.15}P$ is assumed to be the same as InP. The bandgap energy for $In_{0.85}Ga_{0.15}P$ is calculated using equation (5.5)[38]; where $x = 0.15$.

As discussed in the previous section the longitudinal, d_{31}, piezoelectric coefficient is of interest. Using the above piezoelectric strain matrix a field applied in the z-direction or parallel to the X_3 will result in a longitudinal extension in the x and y direction, equations (5.6)&(5.7). The depletion width is parallel to the field causing excitation of the longitudinal d_{31} piezoelectric coefficient, figure (5.5). The depletion width/piezoelectric region can therefore be changed by applying a DC voltage. The type of structures and deformation is discussed in the next section.

$$W = \left[\frac{2\epsilon_1\epsilon_2\epsilon_0\left(\psi_{bi} - V_0\right)}{q\left(\epsilon_1 N_{d_1} + \epsilon_2 N_{d_2}\right)}\right]^{\frac{1}{2}} \tag{5.1}$$

$$C = \frac{\epsilon_1\epsilon_0 A}{W} \tag{5.2}$$

$$W = \left[\frac{2\varepsilon_r\varepsilon_o V}{qN_{d_1}}\right]^{1/2};\ V = \varphi - \left[\frac{E_g}{2q} - \frac{k_B T}{q}\ln\left(\frac{N_{d_1}}{n_i}\right)\right] \tag{5.3}$$

$$W = \left[\frac{2\varepsilon_r\varepsilon_0}{qN_D}\left(\psi_{bi} - V - \frac{kT}{q}\right)\right]^{1/2} \tag{5.4}$$

$$E_g = 1.35 + 0.688x + 0.758x^2 \tag{5.5}$$

Depletion Mechanism	Depletion Width (nm)	$In_{0.85}Ga_{0.15}P$	InP(%)
$In_{0.85}Ga_{0.15}P$/InP	109.56	Fully	5.96
Surface States	429.53	Fully	25.12
Au/$In_{0.85}Ga_{0.15}P$	517.20	Fully	30.37

Table 5.2: Depletion width from the various mechanisms

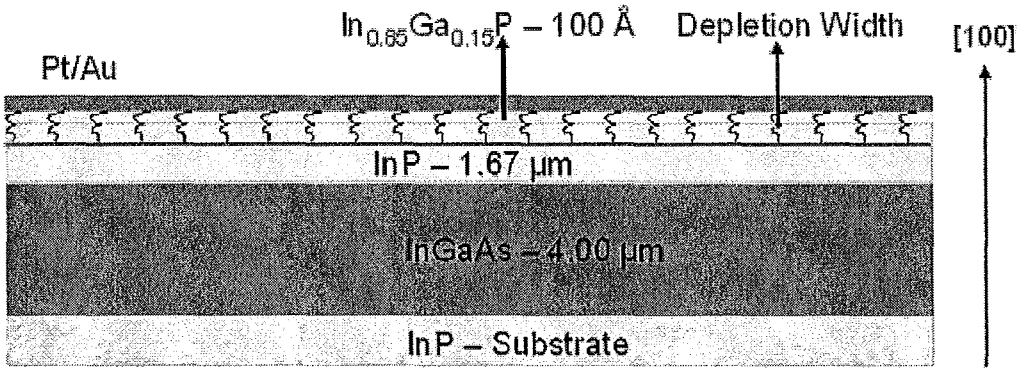

Figure 5.5: Depletion width of Au/$In_{0.85}Ga_{0.15}P$/InP

$$\epsilon_p = d_{iq} E_q$$

$$\begin{bmatrix} \epsilon_x \\ \epsilon_y \\ \epsilon_z \\ \epsilon_{yz} \\ \epsilon_{xz} \\ \epsilon_{xy} \end{bmatrix} = 1.0e-12 \begin{bmatrix} 0 & 0 & 1.8 \\ 0 & 0 & 1.8 \\ 0 & 0 & 0 \\ 0 & 3.6 & 0 \\ -3.6 & 0 & 0 \\ 0 & 0 & 0 \end{bmatrix} \begin{bmatrix} 0 \\ 0 \\ E_z \end{bmatrix}$$

$$\epsilon_x = 1.8 \times 10^{-12} E_z \tag{5.6}$$

$$\epsilon_y = 1.8 \times 10^{-12} E_z \tag{5.7}$$

5.2.0.2 Mechanical Design

The mechanical structures intended for actuation are cantilevers and bridges made from the 1.68 μm thick $In_{0.85}Ga_{0.15}P$/InP layer, figure (5.6). As discussed above, only a certain width of the region will be piezoelectrically active. This is the monomorph configuration discussed in the theory section. A field in the X_3 or z-direction will result in a flexural deformation along the X_1X_3 or xz plane, figure (5.7).

With regards to the Q-value a low to medium value is expected because: considering the intrinsic mechanisms single crystal InP with MBE grown layers is used which results in low defects, considering the extrinsic mechanisms: the contributions from: (a) gas pressure can be neglected by placing the device in a vacuum, (b) surface losses and (c) clamping losses, although hard to quantify, will contribute to lowering the Q-value.

With the above criteria of thickness the following range of dimensions could be used for fabricating bridges and cantilevers $(l \times w \times t)\,\mu m$: $168 - 1000 \times 10.68 - 100 \times 1.68$

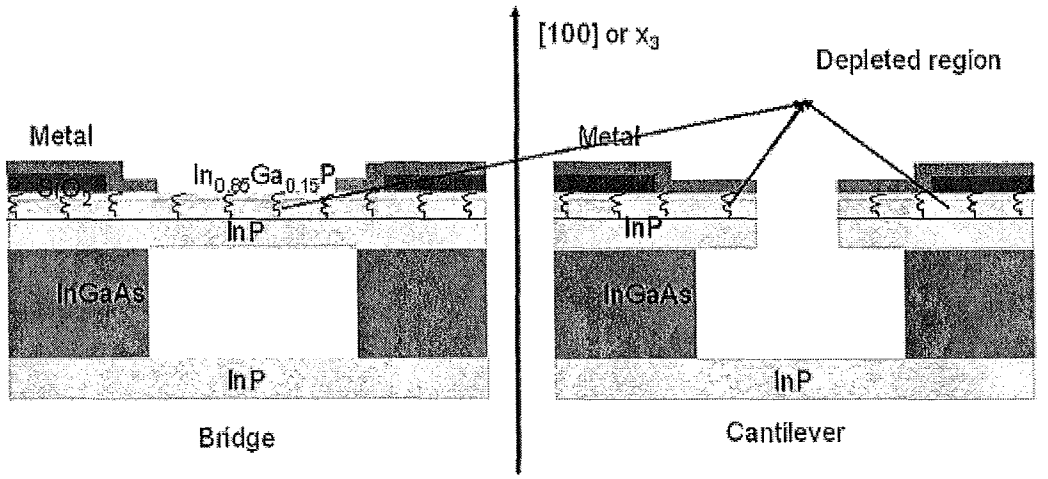

Figure 5.6: InP mechanical structures, bridges and cantilevers, with depletion width showing

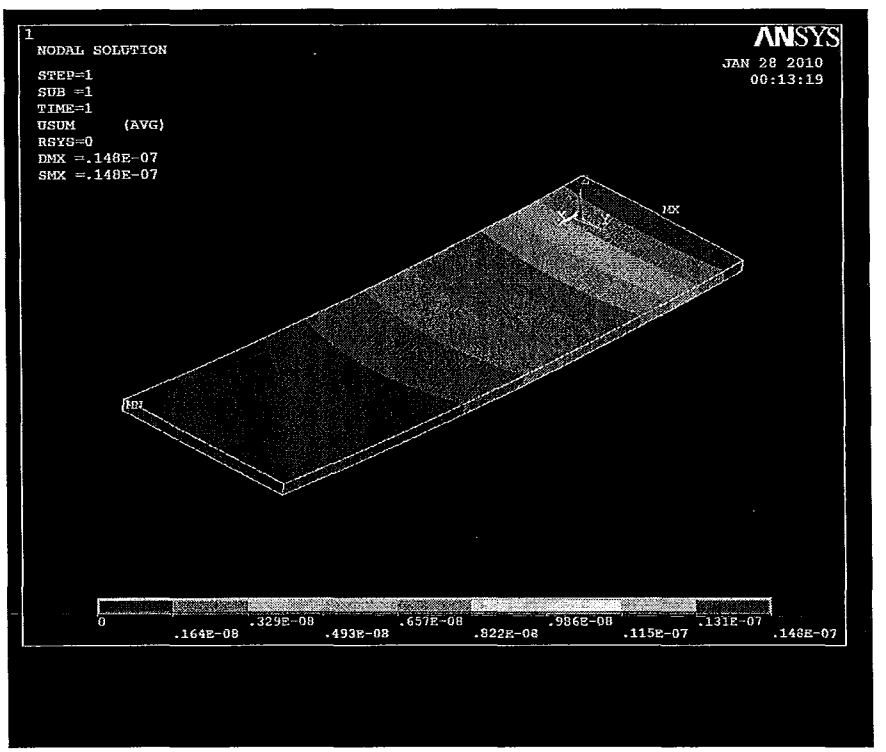

Figure 5.7: Flexural vibrations in xz plane of a cantilever

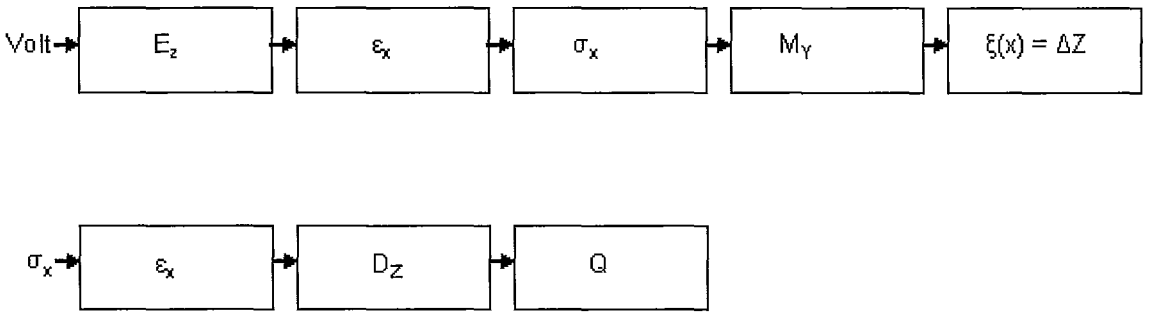

Figure 5.8: Overview of calculation for deflection (above) from an applied voltage and piezoelectric charge (below) from stress

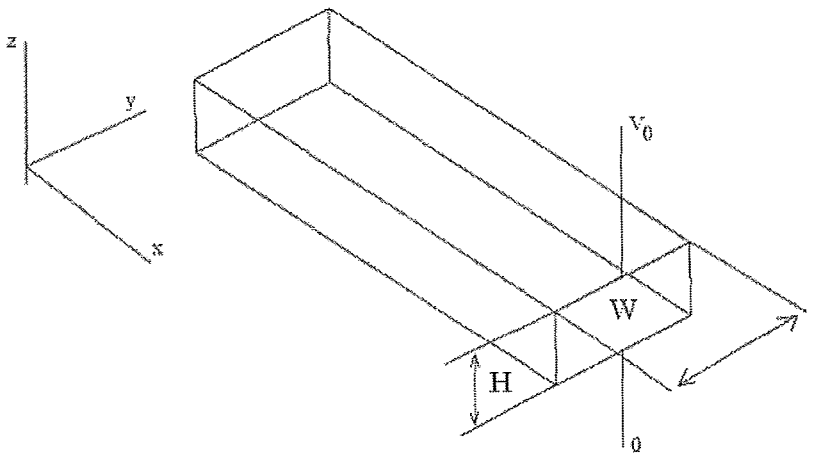

Figure 5.9: Geometry and associated coordinate system for InP

5.3 Theoretical Result

In this section the deflection of the cantilever and bridge and the associated charge is calculated using equations (2.12)&(2.36). The overview of the derivation, given in figure (5.8), is as follows: an applied voltage creates a z-directed field which produces a x-directed strain due to the piezoelectric effect. The resulting strain produces a x-directed stress. The stress creates a bending moment in the y-direction resulting in a deflection in the z-direction. For calculating the charge the x-directed strain due to the applied field results in a dipole, producing an electric displacement in the z-direction which can be integrated to calculate the piezoelectric charge. Figure (5.9) is the geometry of the InP structure and the associated coordinate system. Here the x-axis is the length, L, y-axis is the width, W, and z-axis is the height or thickness, H, of the beam. Electrodes are applied orthogonal to the z-direction.

5.3.1 Cantilever Deflection and Charge

5.3.1.1 Deflection

The potential due to the electrode configuration is V_0 and the electric field is given by equation (5.8), where d is the distance between the top electrode and the ground plane which is some fraction of the total thickness H. Additionally, d is the thickness of the piezoelectric region. Using the strain

equation (2.34) the stress is given by equation (5.9). This is the normal stress pertaining to a normal force figure (2.3).

$$E_z(z) = \frac{\Delta V}{d} = \frac{V_o}{d} \tag{5.8}$$

$$\sigma_x = \frac{d_{13} Y V_o}{d} \tag{5.9}$$

The moment is calculated using equation (2.3). Equation (5.10) is the moment of the cantilever beam.

$$M_y = \int_0^d \int_0^W z \sigma_x dy dz$$

$$M_y = \int_0^d \int_0^W \frac{z d_{13} Y V_o}{d} dy dz$$

$$M_y = \frac{d d_{13} Y V_o W}{2} \tag{5.10}$$

The above moment is for the piezoelectric region only. The moment for a monomorph, equation (5.11), takes into account the complete thickness of the structure. Therefore when the structure is completely piezoelectric the moment should be zero which is as expected because instead of bending the structure will extend or compress.

$$M_y = \frac{(H-d)\, d_{13} Y V_o W}{2} \tag{5.11}$$

Similar to the QTF case the displacement of the tip can be calculated using two approaches: (a) assuming the beam bends in a parabolic shape and (b) using the mode shapes of a cantilever subjected to a constant moment . As shown in the previous section, the two will result in the same equation. Therefore using the parabolic assumption the tip deflection is derived.

The equation for parabolic deflection is $\xi(x) = \xi_0 \left(\frac{x}{L}\right)^2$; where ξ_0 is the tip deflection. The maximum deflection occurs at $x = L$. Using the 2^{nd} order differential equation for beam bending the tip displacement is given by equation (5.12) and equation (5.13) is the general expression for deflection along the beam. Equation (5.12) is independent of the width of the beam while equation (3.11), for the QTF case, depends linearly. This linear dependence is due to the electrode configuration. The contribution of the electrode placement in the InP case is the deflection depends as the inverse square of the height or thickness. In both cases the deflection increases linearly with applied potential and as the square of length.

$$\frac{1}{\rho} = \frac{M}{YI} = \frac{\partial^2 \xi}{\partial x^2}$$

$$\frac{\partial^2 \xi}{\partial x^2} = \frac{2\xi_o}{L^2}$$

$$\frac{M}{YI} = \frac{2\xi_o}{L^2}$$

$$\frac{ML^2}{2YI} = \xi_o$$

$$\xi_o = \frac{(H-d)\, d_{13} Y V_o W}{2} \left(\frac{L^2}{2YI}\right)$$

$$\xi_o = \frac{(H-d)\, d_{13} V_o W}{4} \left(\frac{L^2}{I}\right)$$

$$\xi_o = \frac{(H-d)\, d_{13} V_o W}{4} \left(\frac{L^2}{\frac{1}{12} W H^3}\right)$$

$$\xi_o = \frac{3\,(H-d)\, d_{13} V_o L^2}{H^3} = \frac{3\,(H-d)\, e_{13} V_o L^2}{Y H^3} \tag{5.12}$$

$$\xi\,(x) = \frac{3\,(H-d)\, e_{13} V_o x^2}{Y H^3} \tag{5.13}$$

5.3.1.2 Dielectric and Piezoelectric Charge

Equation (2.36) is the general expression for calculating charge on the electrodes due to inverse piezoelectric effect and the dielectric. Expressing this equation for the InP case results in equation (5.14). As before, the piezoelectric charge is first calculated then the dielectric.

$$Q = \int_o^L \int_o^W e_{13} \varepsilon_x dy dx + \int_o^L \int_o^W \varepsilon_r \varepsilon_o E_z dy dx \tag{5.14}$$

Piezoelectric Charge Equation (5.16) is the piezoelectric charge for the InP cantilever. The $\overline{z}$ term in this equation is the distance from the neutral axis, equation (5.15), to the region of greatest stress/strain and is dependent on the thickness of the piezoelectric and elastic layers. The region of greatest stress is on the surface of the beam, therefore this value is subtracted by the total thickness of the beam.

The neutral axis is calculated using the cross-section, figure (5.10) and the following three conditions:

1. Sum of all normal forces along the x-direction is zero

$$\sum_{i=1}^{2} F_{x,i} = 0$$

2. Strain related to curvature is defined as:

$$\epsilon_x\,(x,z) = -z \frac{\partial^2 \xi}{\partial x^2}$$

3. Mechanical stress or normal stress in the x-direction is:

$$\sigma_x\,(x,z) = -zY \frac{\partial^2 \xi}{\partial x^2}$$

Relating the normal stress to the normal force:

$$\sigma_x\,(x,z) = \frac{dF_{x,i}}{dA}$$

Rearranging this expressions for $F_{x,i}$, using the first condition and noticing that the curvature and width is constant across the layers:

$$0 = \sum_{i=1}^{2} \int_{h_{i,u}}^{h_{i,o}} z dz = \sum_{i=1}^{2} z^2 \,|_{h_{i,u}}^{h_{i,o}} = \sum_{i=1}^{2} (h_{i,o})^2 - (h_{i,u})^2 = (h_{1,o})^2 - (h_{1,u})^2 + (h_{2,o})^2 - (h_{2,u})^2$$

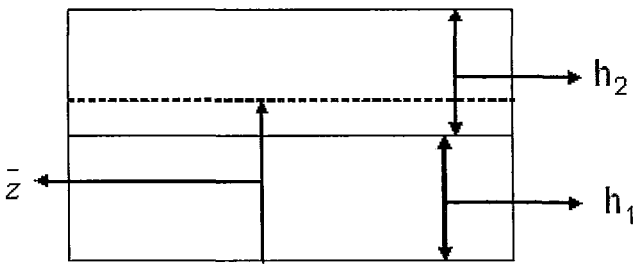

Figure 5.10: Geometry for neutral width calculation, $\overline{z}$ is the neutral plane, h_1- thickness of elastic region and h_2- thickness of piezoelectric layer. All distances are measured with respect to the bottom of the elastic region.

The limits of integration (lower and upper) are defined relative to the neutral axis, $\overline{z}$:

$$h_{i,u} = \overline{z} - \sum_{j=1}^{2} h_j = \overline{z} - h_1 - h_2 \, and \, h_{i,o} = \overline{z} - \sum_{j=1}^{1} h_j = \overline{z} - h_1$$

The neutral axis is:

$$\overline{z} = -\left[\frac{-h_1^2 - h_2^2 - 4h_1h_2}{2\left(h_1+h_2\right)}\right] \tag{5.15}$$

If either of the thickness is zero, i.e. $h_1 = 0$or $h_2 = 0$, the neutral axis is half of the other thickness, i.e. $\overline{z} = \frac{h_2}{2}$or $\overline{z} = \frac{h_1}{2}$

Using the above equation for neutral axis the charge is derived::

$$Q = \int_o^L \int_o^W \overline{z} \frac{\partial^2 \xi}{\partial x^2} e_{13} dy dx$$

$$Q = \left(H - \overline{z}\right) e_{13} W \frac{\partial \xi}{\partial x}|_{x=L}$$

$$Q = \left(H - \overline{z}\right) e_{13} W \frac{6 d d_{13} V_o L}{H^3}$$

$$Q = \frac{3\left(H - d\right)\left(H - \overline{z}\right) e_{13}^2 V_0 L W}{Y H^3} \tag{5.16}$$

Dielectric Charge Equation (5.17) is the dielectric charge.

$$Q = \int_o^L \int_o^W \varepsilon_r \varepsilon_o E_z dy dx$$

$$Q = \frac{\varepsilon_r \varepsilon_o V_o L W}{d} \tag{5.17}$$

5.3.2 Bridge Deflection and Charge

5.3.2.1 Bridge Deflection

Bridge deflection is calculated using equation (2.31). This equation is the maximum deflection of a bridge, which is at the center. The same boundary conditions and assumptions as for the cantilever case is used. The sum part of the equation is first evaluated. Equation (5.18) is the sum part and the values for the first ten modes are given in table (5.3). As is seen from the table the contributions

i	k_iL	Sum
1	4.730040745	0.01534103888
2	7.853204624	-0.2464865261e-10
3	10.99560784	0.0006397621772
4	14.13716549	0.4727637217e-10
5	17.27875966	-0.0003619224408
6	20.42035225	0.6426962000e-9
7	23.56194490	-0.00005821168207
8	26.70353756	0
9	29.84513021	0.00006946533940
10	32.98672286	0

Table 5.3: Sum part of equation (5.18) evaluated at the first 10 cantilever modes

from the even modes is zero which is expected because at half the length the deflection is zero. The total sum for the ten modes is 0.015630132. Equation (5.19) is the maximum deflection of the bridge with evaluated sum.

$$\xi\left(\frac{L}{2}\right) = \frac{ML^2}{YI}\sum_{i=1}^{\infty}\left[\frac{\left(cosh\left(\frac{k_iL}{2}\right)-cos\left(\frac{k_iL}{2}\right)-\alpha_i\left(sinh\left(\frac{k_iL}{2}\right)-sin\left(\frac{k_iL}{2}\right)\right)\right)}{\left(k_iL\right)^2}\right.$$
$$\left.\frac{\left(sinh\left(\frac{k_iL}{4}\right)+sin\left(\frac{k_iL}{4}\right)-\alpha_i\left(cosh\left(\frac{k_iL}{4}\right)-cos\left(\frac{k_iL}{4}\right)\right)\right)}{\left(k_iL\right)}\right]$$

$$sum = \sum_{i=1}^{\infty}\left[\frac{\left(cosh\left(\frac{k_iL}{2}\right)-cos\left(\frac{k_iL}{2}\right)-\alpha_i\left(sinh\left(\frac{k_iL}{2}\right)-sin\left(\frac{k_iL}{2}\right)\right)\right)}{\left(k_iL\right)^2}\right.$$
$$\left.\frac{\left(sinh\left(\frac{k_iL}{4}\right)+sin\left(\frac{k_iL}{4}\right)-\alpha_i\left(cosh\left(\frac{k_iL}{4}\right)-cos\left(\frac{k_iL}{4}\right)\right)\right)}{\left(k_iL\right)}\right] \tag{5.18}$$

$$\xi\left(\frac{L}{2}\right) = \frac{6\left(H-d\right)e_{13}V_oL^2}{YH^3}\left(0.015630132\right)$$

$$\xi\left(\frac{L}{2}\right) = \frac{\left(0.093780782\right)\left(H-d\right)e_{13}V_oL^2}{YH^3} \tag{5.19}$$

5.3.2.2 Dielectric and Piezoelectric Charge

Equation (5.14) is used to calculate the piezoelectric and dielectric charge.

Piezoelectric Charge Equation (5.20) is the piezoelectric charge for the bridge case and is derived as follows:

$$Q = \int_o^a\int_o^W \overline{z}\frac{\partial^2\xi}{\partial x^2}\varepsilon_{13}dydx$$

$$Q = \overline{z}\varepsilon_{13}W\frac{\partial\xi}{\partial x}|_{x=a}$$

$$\xi(x) = \frac{ML^2}{YI}\sum_{i=1}^{\infty}\left[\frac{[\cosh(k_i x)-\cos(k_i x)-\alpha_i(\sinh(k_i x)-\sin(k_i x))]}{(k_i L)^2}\right.$$
$$\left.\frac{[\sinh(\frac{k_i L}{4})+\sin(\frac{k_i L}{4})-\alpha_i(\cosh(\frac{k_i L}{4})-\cos(\frac{k_i L}{4}))]}{(k_i L)}|_{x=a}\right]$$

$$\frac{\partial\xi}{\partial x} = \frac{ML^2}{YI}\sum_{i=1}^{\infty}\left[\frac{k_i[\sinh(k_i x)+\sin(k_i x)-\alpha_i(\cosh(k_i x)-\cos(k_i x))]}{(k_i L)^2}\right.$$
$$\left.\frac{[\sinh(\frac{k_i L}{4})+\sin(\frac{k_i L}{4})-\alpha_i(\cosh(\frac{k_i L}{4})-\cos(\frac{k_i L}{4}))]}{(k_i L)}|_{x=a}\right]$$

$$\frac{\partial\xi}{\partial x} = \frac{ML}{YI}\sum_{i=1}^{\infty}\left[\frac{[\sinh(k_i x)+\sin(k_i x)-\alpha_i(\cosh(k_i x)-\cos(k_i x))]}{(k_i L)^2}\right.$$
$$\left.\frac{[\sinh(\frac{k_i L}{4})+\sin(\frac{k_i L}{4})-\alpha_i(\cosh(\frac{k_i L}{4})-\cos(\frac{k_i L}{4}))]}{(k_i L)^2}|_{x=a}\right]$$

$$\frac{\partial\xi}{\partial x} = \frac{ML}{YI}\sum_{i=1}^{\infty}\left[\frac{[\sinh(k_i a)+\sin(k_i a)-\alpha_i(\cosh(k_i a)-\cos(k_i a))]}{(k_i L)}\right.$$
$$\left.\frac{[\sinh(\frac{k_i L}{4})+\sin(\frac{k_i L}{4})-\alpha_i(\cosh(\frac{k_i L}{4})-\cos(\frac{k_i L}{4}))]}{(k_i L)}\right]$$

$$Q = \frac{(H-\overline{z})\,e_{13}WML}{2YI}$$
$$\sum_{i=1}^{\infty}\left[\frac{[\sinh(k_i a)+\sin(k_i a)-\alpha_i(\cosh(k_i a)-\cos(k_i a))]}{(k_i L)}\right.$$
$$\left.\frac{[\sinh(\frac{k_i L}{4})+\sin(\frac{k_i L}{4})-\alpha_i(\cosh(\frac{k_i L}{4})-\cos(\frac{k_i L}{4}))]}{(k_i L)}\right]$$

$$Q = \frac{(H-\overline{z})\,e_{13}WL}{2YI}\left(\frac{(H-d)\,d_{13}YV_oW}{2}\right)$$
$$\sum_{i=1}^{\infty}\left[\frac{[\sinh(k_i a)+\sin(k_i a)-\alpha_i(\cosh(k_i a)-\cos(k_i a))]}{(k_i L)}\right.$$
$$\left.\frac{[\sinh(\frac{k_i L}{4})+\sin(\frac{k_i L}{4})-\alpha_i(\cosh(\frac{k_i L}{4})-\cos(\frac{k_i L}{4}))]}{(k_i L)}\right]$$

$$Q = \frac{3(H-\overline{z})(H-d)\,e13d_{13}V_oWL}{H^3}$$
$$\sum_{i=1}^{\infty}\left[\frac{[\sinh(k_i a)+\sin(k_i a)-\alpha_i(\cosh(k_i a)-\cos(k_i a))]}{(k_i L)}\right.$$
$$\left.\frac{[\sinh(\frac{k_i L}{4})+\sin(\frac{k_i L}{4})-\alpha_i(\cosh(\frac{k_i L}{4})-\cos(\frac{k_i L}{4}))]}{(k_i L)}\right]$$

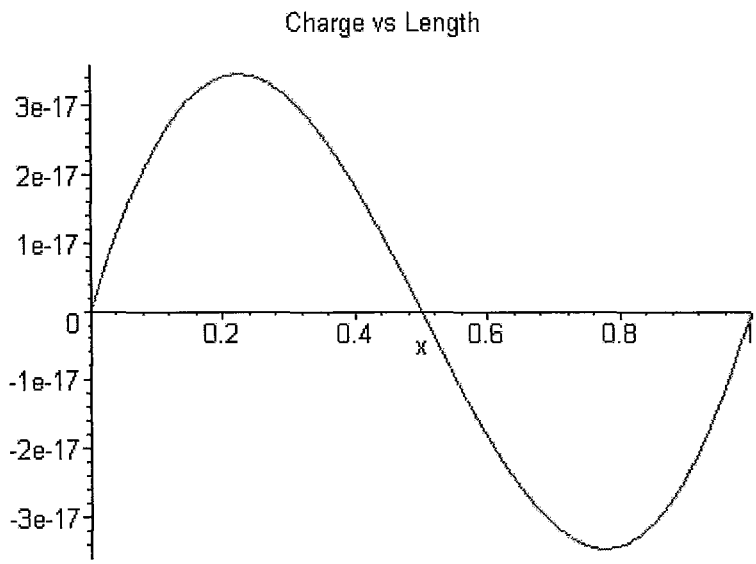

Figure 5.11: Charge vs bridge length. Maximum charge is at maximum strain at quarter length

$$Q = \frac{3(H-\overline{z})(H-d)e_{13}^2 V_o W L}{YH^3} \sum_{i=1}^{\infty}\left[\frac{[\sinh(k_i a)+\sin(k_i a)-\alpha_i(\cosh(k_i a)-\cos(k_i a))]}{(k_i L)} \frac{[\sinh(\frac{k_i L}{4})+\sin(\frac{k_i L}{4})-\alpha_i(\cosh(\frac{k_i L}{4})-\cos(\frac{k_i L}{4}))]}{(k_i L)}\right]$$

Plotting the charge vs length, figure (5.11), the maximum charge is detected at quarter the length of the bridge at the point of maximum strain. Therefore $a = L/4$ and equation (5.20) is the expected piezoelectric charge.

$$Q = \frac{3(H-\overline{z})(H-d)e_{13}^2 V_o W L}{YH^3} \sum_{i=1}^{\infty}\left[\frac{[\sinh(\frac{k_i L}{4})+\sin(\frac{k_i L}{4})-\alpha_i(\cosh(\frac{k_i L}{4})-\cos(\frac{k_i L}{4}))]}{(k_i L)} \frac{[\sinh(\frac{k_i L}{4})+\sin(\frac{k_i L}{4})-\alpha_i(\cosh(\frac{k_i L}{4})-\cos(\frac{k_i L}{4}))]}{(k_i L)}\right]$$

$$Q = \frac{3(H-\overline{z})(H-d)(0.072878)e_{13}^2 V_o W L}{YH^3} \tag{5.20}$$

Figures (5.12)-(5.13)(a)-(c) is the comparison between the analytical and simulated deflect on, piezoelectric and dielectric capacitance as a result of change in depletion width. The following dimension are used for the cantilever and bridge: $(l \times w \times t)\,\mu m$ $100 - 150 \times 20 \times 1.68$. From both these sets of plots it is readily seen that as the depletion width or piezoelectric thickness is increased the deflection and piezoelectric charge decreases. This is expected because increasing the width of

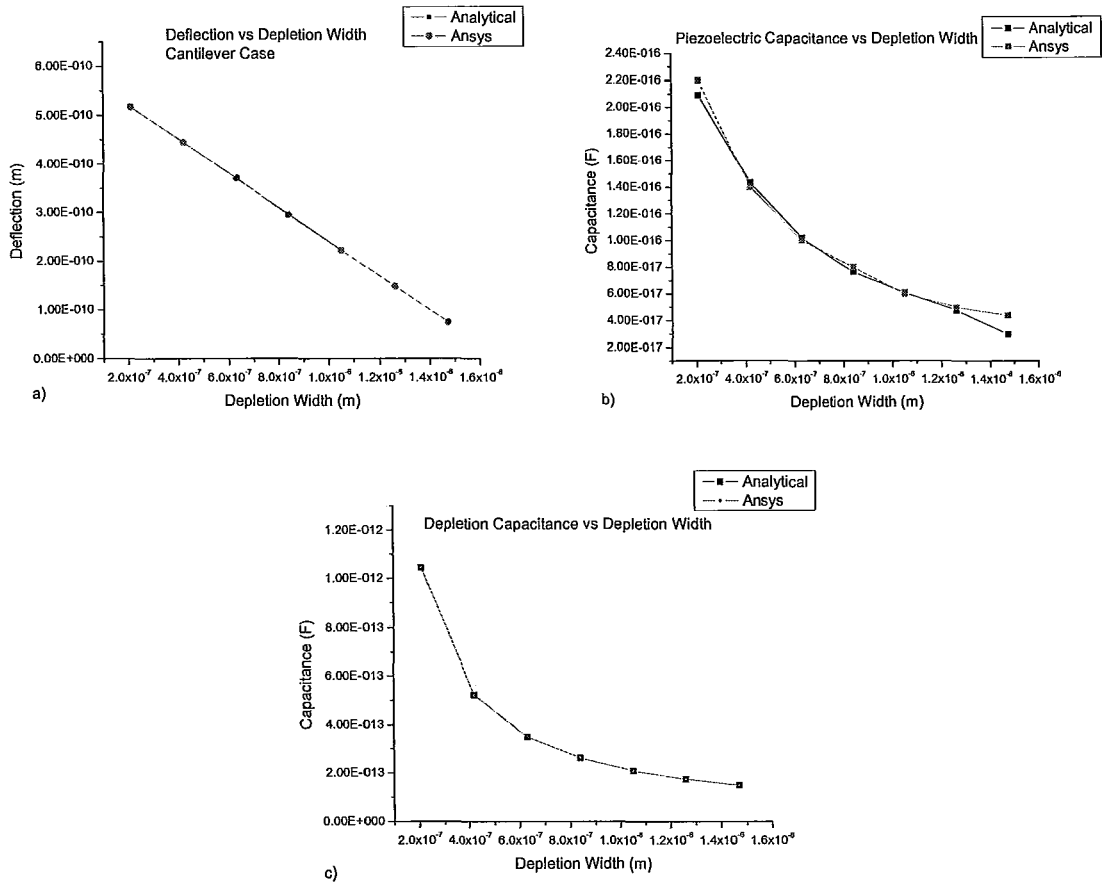

Figure 5.12: Cantilever case comparison of analytical and simulation: (a) deformation; (b) piezoelectric and (c) depletion capacitance vs depletion width

the piezoelectric thickness decreases the moment hence strain. For the bridge case the simulated charge is four times larger than the analytical result. Figure (5.14)(a)(b) is a comparison between the deflection and piezoelectric capacitance between the cantilever and bridge. The cantilever's deflection is 32 times larger and the cantilever charge is 13.7 times larger than the bridge. This is expected by analyzing equation (5.12) and (5.20). The depletion capacitance of the cantilever is 5 times larger than the bridge.

5.3.3 Bridge Design

The bridge resonator is chosen, as opposed to the cantilever, to be fabricated because it is less susceptible to stiction issues during fabrication and the three terminal configuration can be used to measure its piezoelectric properties. The disadvantage, as mentioned above, is the lower piezoelectric capacitance while relatively higher depletion or package capacitance. Using equation (2.19), table (2.2) and equation (2.39) the theoretical resonance frequency, inductance, piezoelectric and dielectric capacitance at the fundamental mode is given in table (5.4) for a drive voltage of $0.1V_{rms}$and a depletion width of 210 nm. The density and modulus of elasticity chosen are: 4810 kg/m^3[30] and

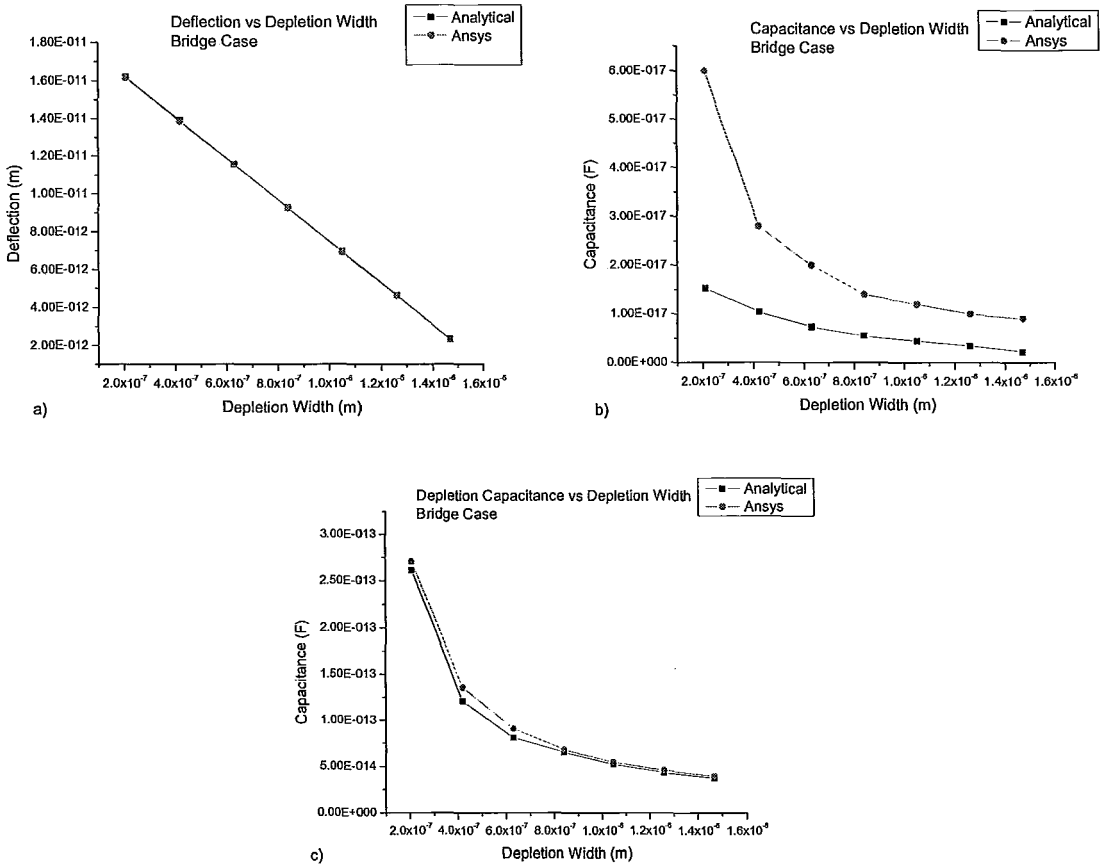

Figure 5.13: Bridge case comparison of analytical and simulation: (a) deformation; (b) piezoelectric and (c) depletion capacitance vs depletion width

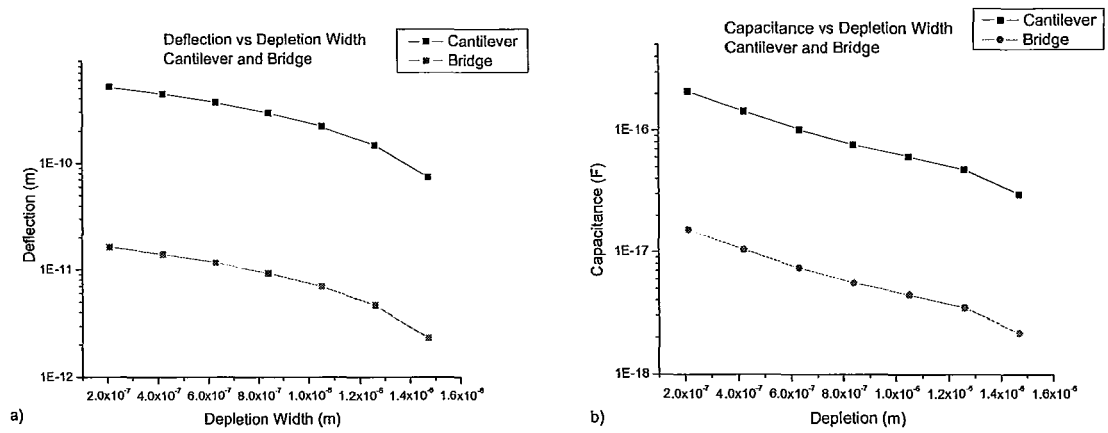

Figure 5.14: Comparison between cantilever and bridge: (a) deflection, (b) piezoelectric capacitance

Bridge Dimensions $(l \times w \times t)\ \mu m$	*Frequency (Hz)*	*Piezoelectric Capacitance (F)*	*Inductance (H)*	*Package Capacitance (F)*
$100 \times 20 \times 1.68$	584,323.49	1.525×10^{-17}	4866.45	2.612×10^{-13}

Table 5.4: Theoretical frequency, inductance and capacitance

55.09 GPa[1].

The expected Q-value is approximately 1000 giving a resonator resistance of 17.86 $M\Omega$ which is 17 times larger than the impedance of the package capacitance at resonance. Therefore, in order to measure the signal from the resonator any or all signals from the background including the package capacitance must be removed. In the design of the device this is done by isolating the metal from the semiconductor using an oxide layer of appropriate thickness except where required, i.e. the bridge and the ground planes. Adding an oxide layer adds to the package capacitance. A three terminal setup, as described in the previous section, can be used where the mutual capacitance between the electrodes is used as the package capacitance. This reduces the capacitance by eleven million as calculated in section (5.6.0.2), 3-Term Method . The oxide on metal is the familiar MOS design, making this device a MOS in parallel with a MIS.

5.4 Fabrication

The layer structure that constitutes the basis of the fabricated resonators is grown on a 2 in. diameter InP(100) wafer in ultrahigh vacuum MBE. Figure (5.4) is the cross-section of the grown structure. As mentioned above, the first layer grown is a 4.0 µm thick $In_{0.53}Ga_{0.47}As$ sacrificial layer(orange). The cantilever/bridge layer consists of layers two and three – InP(blue) and $In_{0.85}Ga_{0.15}P$(yellow) having thickness of 1.67 µm and 100 Å, respectively. In this research work, bridges are fabricated.

The 2 in. diameter wafer is cleaved into $14.0 \times 14.0 mm$ samples on which resonators are fabricated. Bridges having dimension of $(l \times w \times t)\ \mu m$ $100 - 150 \times 30 \times 1.68$ are fabricated. On each sample there are nine bridges, three of which share the same dimension. These three belong to a set making a total of three sets. The middle bridge of every set has different electrode configuration giving the ability to measure and subtract the background contributions.

The bridges are fabricated in a clean room facility using standard fabrication techniques - CVD, optical lithography, metallization and wet chemical etching. A total of four masking steps are used to fabricate the bridges and three for cantilevers. Each of these steps are described below. The first step defines the ground electrodes, the second step defines the etch holes, third step metallization for lift-off and fourth step release of bridge. The CVD is used to deposit SiO_2 which serves the purpose of an etch masking layer and an insulator to isolate the resonator signal from background. Optical lithography is used to transfer the pattern from a mask to a photoresist.

1. **Preparation of ground electrodes by selectively removing the $In_{0.85}Ga_{0.15}P$ layer.** A 1000 Å of CVD SiO_2 is grown. SiO_2 serves as a masking layer for the subsequent removal of $In_{0.85}Ga_{0.15}P$. Photoresist (PR) is spun and deposited. In figure (5.15)(a) red represents SiO_2 and green represents PR. Using optical lithography the mask pattern, figure (5.15)(b), is transferred. The exposed PR is removed exposing SiO_2. SiO_2 is removed using hydrogen flouride (HF) exposing $In_{0.85}Ga_{0.15}P$. $In_{0.85}Ga_{0.15}P$ is removed using a one to three ratio of hydrogen chloride and hydrogen phosphide (1:3 $HCl:H_3PO_4$). The underlying InP is now exposed, figure (5.15)(c), and in step 2 will be defined so that in step 3 metalization can occur. Both PR and SiO_2 are removed. The sample is now ready for the next step.

2. **Pattern ground electrodes and expose $In_{0.85}Ga_{0.15}P$ etch holes** by selectively removing grown SiO_2. Similar to the previous step SiO_2 is grown and PR is deposited, figure (5.16)(a).

[1] *Calculated from Ansys*

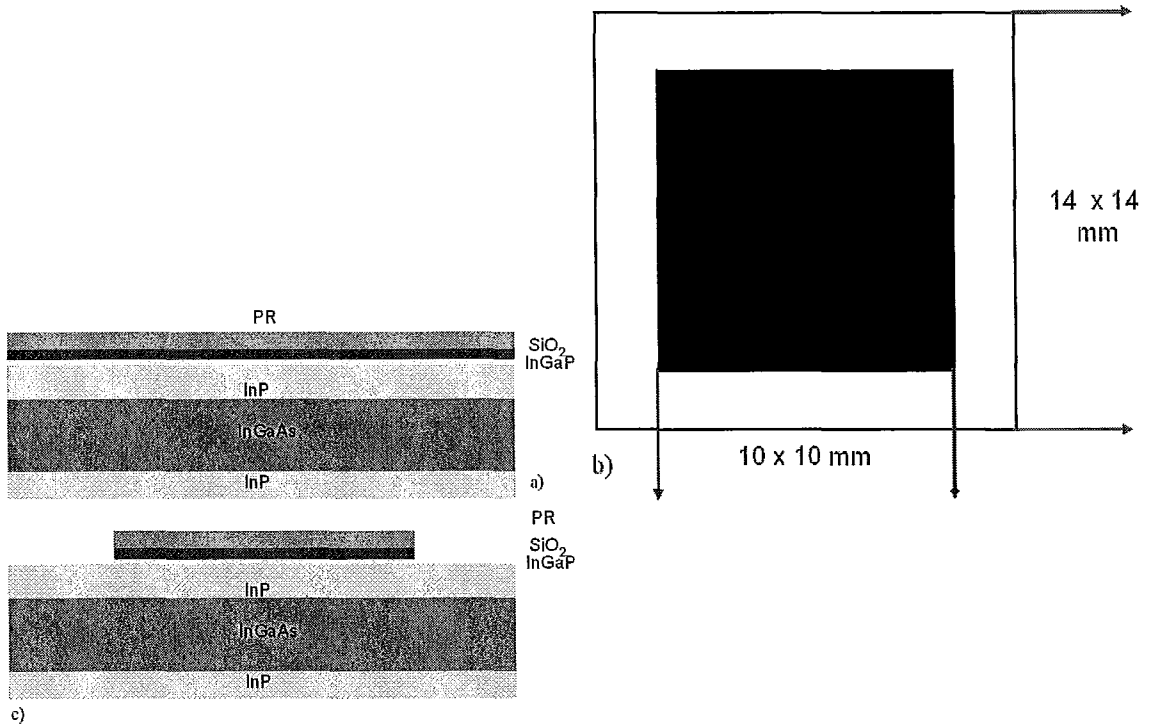

Figure 5.15: a)Cross-secton of CVD grown SiO_2(red) and PR(green), b) Mask pattern, c) Cross-section of PR, SiO_2 and $In_{0.85}Ga_{0.15}P$ removed exposing InP

The thickness of SiO_2 is 3000 Å. Mask pattern, figure (5.16)(b), is transferred and the exposed PR is removed, allowing for the exposed SiO_2 to be removed. The final step is to remove the PR. The InP ground electrode area is now defined and the etch holes are defined for release of bridge in step 4, figure (5.16)(c)

3. **Metalization**. Lift-off technique is used. PR is deposited and the mask pattern is transferred, figure (5.17)(a). PR is developed and the exposed regions are now ready for deposition of metal. For Schottky contact the following metals are deposited - Ti/Pt/Au/Ti (150/500/1500/150 Å). Ti is deposited on top of Au to provide adhesion for growth of SiO_2 in the final step. After deposition of metal the sample is placed in an acetone bath for lift-off. Majority of the sample has, SiO_2, figure (5.17)(c). Only the bridge regions have electrodes touching the $In_{0.85}Ga_{0.15}P$ layer, figure (5.17)(b). The sample is ready for the final step of bridge release.

4. **Bridge release** This is the final mask step. Similar to steps 1 and 2, SiO_2 is grown and PR is deposited. The thickness of SiO_2 is 1000 Å. Mask pattern, figure (5.18)(a), is transferred and the exposed PR is removed, allowing for the exposed SiO_2 to be removed. This opens up the etch holes from step 2. Using SiO_2 as a masking layer protecting the bridge, the bridge is released by etching $In_{0.85}Ga_{0.15}P$/InP using 1:3 HCl:H_3PO_4 and $In_{0.53}Ga_{0.47}As$ using one to eight to eighty hydrogen sulphide to hydrogen peroxide to water (1:8:80 H_2SO_4: H_2O_2:H_2O), figure (5.18)(b). SiO_2 and PR are removed. Figure (5.18)(c) is the final top-view of the device.

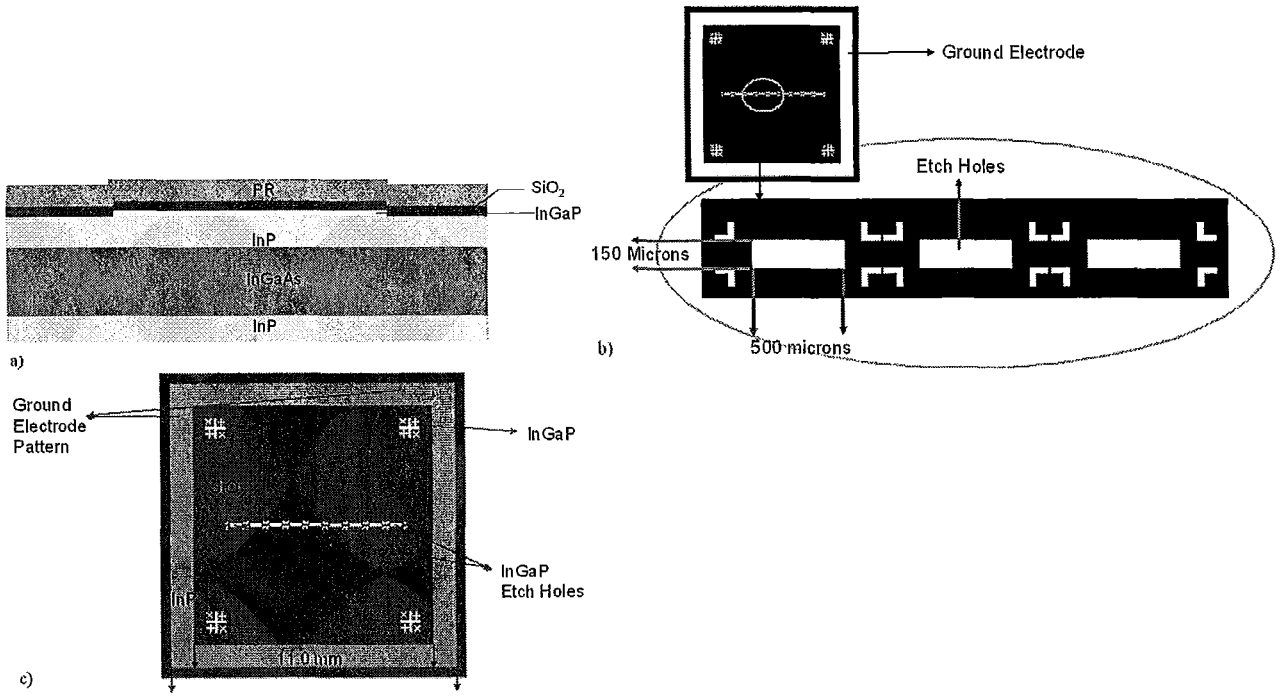

Figure 5.16: a)Cross-secton of CVD grown SiO_2(red) and PR(green), b) Mask pattern, c) Top view of exposed $In_{0.85}Ga_{0.15}P$ etch holes and defined ground electrodes

5.4.1 Results and problems alleviated

Figures (5.19)(a)&(b) and (5.20)(a)&(b) are the successfully fabricated bridges. The bridges dimensions are: $(l \times w \times t)\,\mu m$ $100 - 150 \times 30 \times 1.68$. Various problems were encountered making it difficult for successfull fabrication in the first attempt. One of the simple ones was adhesion between platinum and gold to the oxide layer. This caused unwanted etching in step 4, for example etching at the supports causing figure (5.21), and undesired removal of metal during lift-off. This was solved by adding 150 Å of titanium before platinum and after gold. The difficult problem was determining the etch rates for $In_{0.53}Ga_{0.47}As$ in <110>. An anisotropic etchant is used with a favored etch rate in <100>. Etch rate in <110> is not available. As mentioned in the introduction III-Vs suffer from such types of problems making MEMS fabrication difficult. The etch rate had to be determined experimentally by etching over a time period and measuring the amount removed (figure 5.22). The etch rate was determined to be 250 nm/min. This is 50% slower than in the <100> direction.

5.5 Experimental Setup and Results

The diode characteristics of the device are first determined then the piezoelectric.

Two methods are used to measure the diodes - probe and mounted. For the latter, the sample is mounted on a dual in line package (DIP) header using silver paste as an adhesive between the substrate and the DIP header. Using a ball bonder, Giessen Model 4524, the devices are connected to the pins of the package. The piezoelectric property is measured using the mounted setup.

The bridges electrically are two diodes, because either ends of the bridge have an electrode that extends to a quarter length of the bridge total length. To distinguish between the size and ends of the bridge the following nomenclature is used: $device_{xy}$; here x is the bridge number and y is the side number, table (5.5) and figure (5.23)(a)-(b). As seen in table (5.5) $device_{22}$, $device_{52}$ and $device_{82}$

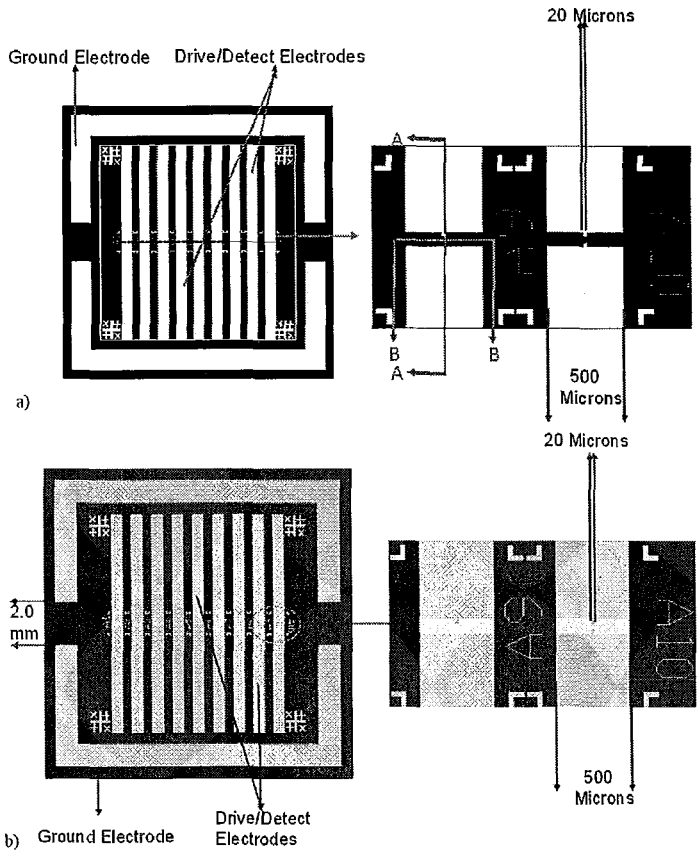

Figure 5.17: a)Mask pattern, b)deposited metal after lift-off

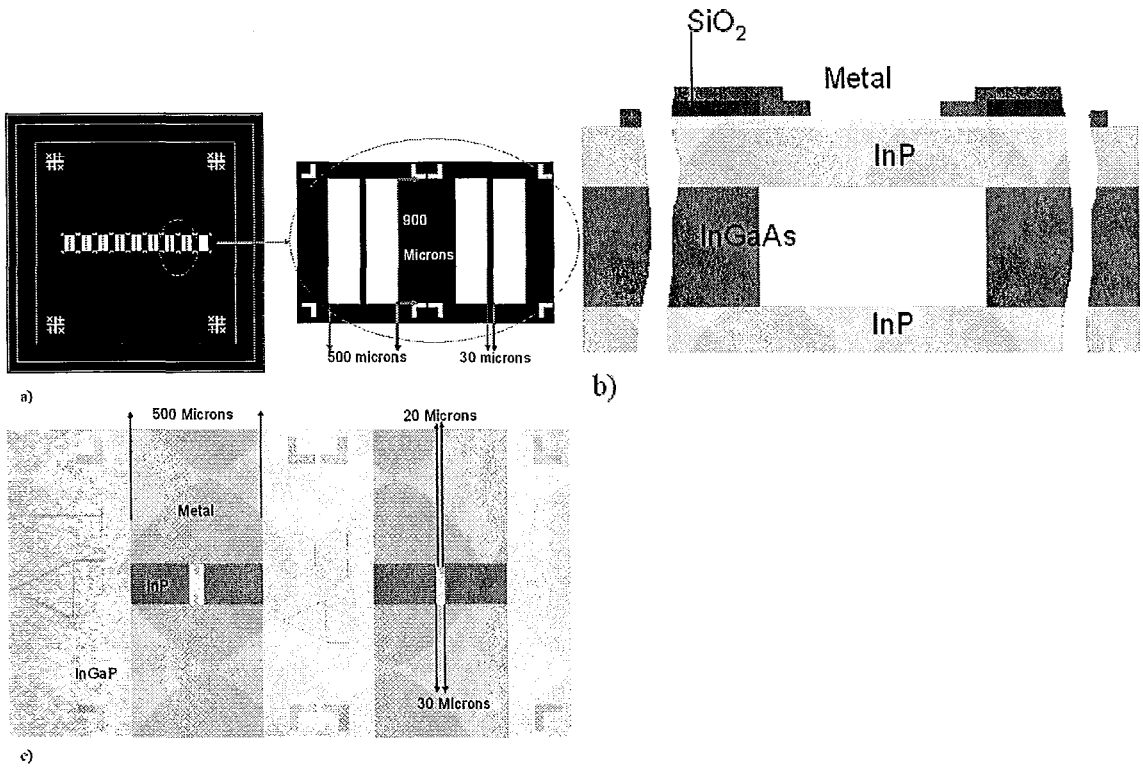

Figure 5.18: a)Mask pattern, b)cross-section etched bridge structure, c) final top-view of structure

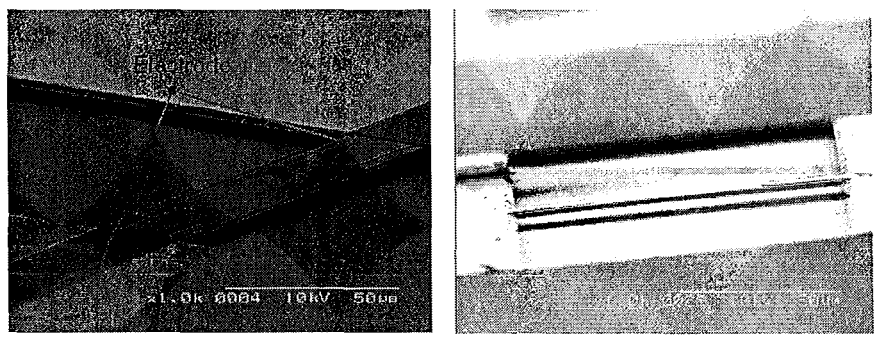

Figure 5.19: InP bridge SEM side view:(a)electrodes on bridge and etch holes; (b)bridge released

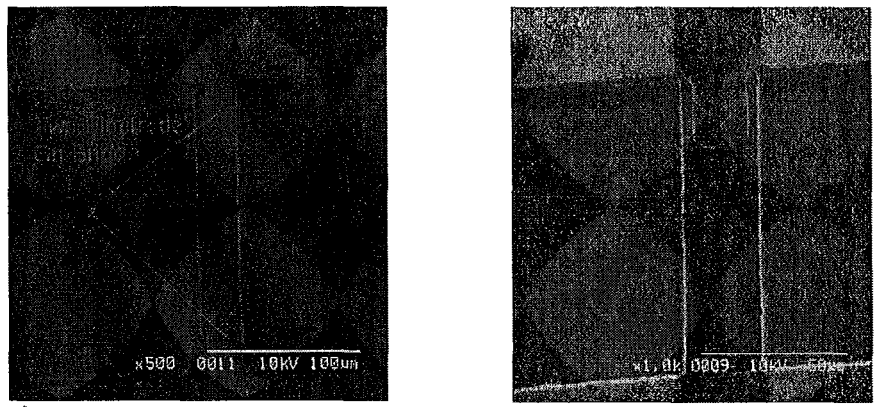

a) b)

Figure 5.20: InP bridge SEM top view:(a)two electrodes; (b)one electrode on bridge

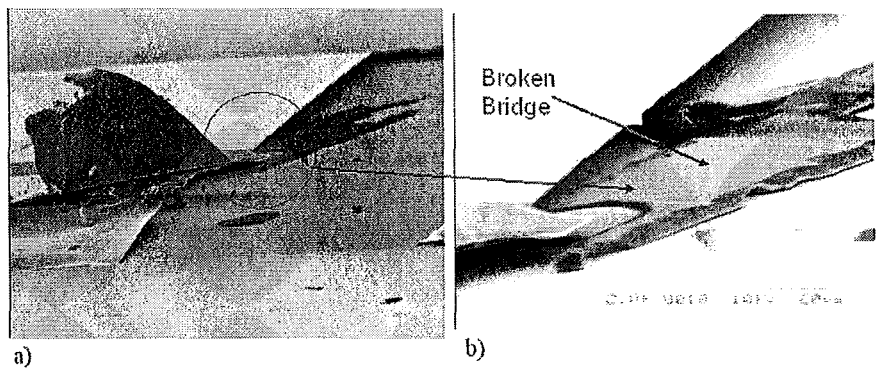

a) b)

Figure 5.21: Broken bridge SEM image:a)broken bridge from the electride; b)magnified view

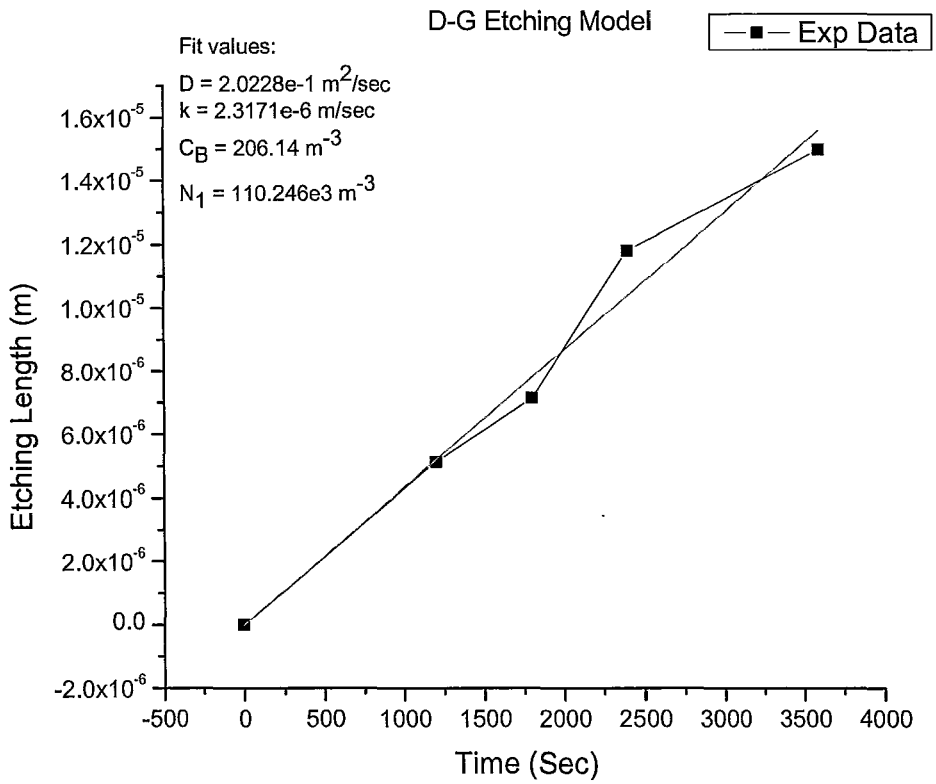

Figure 5.22: Plot of $In_{0.53}Ga_{0.47}As$ etch rate in <110> vs time

Device Number	*Size*(μm)	*Electrode type*
$Device_{11}$	100	*Full*
$Device_{21}$	100	*Full*
$Device_{31}$	100	*Full*
$Device_{41}$	125	*Full*
$Device_{51}$	125	*Full*
$Device_{61}$	125	*Full*
$Device_{71}$	150	*Full*
$Device_{81}$	150	*Full*
$Device_{91}$	150	*Full*
$Device_{12}$	100	*Full*
$Device_{22}$	100	*Half*
$Device_{32}$	100	*Full*
$Device_{42}$	125	*Full*
$Device_{52}$	125	*Half*
$Device_{62}$	125	*Full*
$Device_{72}$	150	*Full*
$Device_{82}$	150	*Half*
$Device_{92}$	150	*Full*

Table 5.5: Device nomenclature

are called half terminal devices because their electrodes do not touch the bridge, figure (5.23)(b) and figure (5.20)(b). The rest of the devices are called full terminal, figure (5.23)(a) and figure (5.20)(a)

.

5.5.0.1 Experimental Setup

Figure (5.24) is the probe setup using Hewlett Packard, HP-4145B, semiconductor parameter analyzer to measure IV curves. This is a simple setup consisting of the device connected to the HP-4145B. Labview is used to control and gather data from the parameter analyzer. Figure (5.25) is the experimental setup used for measuring C-V of the diodes and for frequency sweeping. The general setup consists of: on the drive side a DC source for biasing the device and a function generator for driving the device at a specific frequency and on the detect side: the Amptek A250 amplifier to amplify the signal and the SR-844 RF lock-in to measure this signal. As in the QTF setup, the function generator synchronizes the lock-in amplifier. The computer is used to control the equipment and record data. The frequenices of interest are from the 200 - 1000 KHz.

5.5.0.2 Characterization of 331 pF

A frequency sweep, figure (5.26), of a 331 pF capacitance is made to characterize the response of the amplifier at this frequency range. Ideally the capacitance should remain fixed as the frequency is changed. However, experimentally, the capacitance decreases. For the range of frequencies of interest a change of 10 - 22% is expected. .

5.5.1 Diode IV Curves

The IV curves are measured using Hewlett Packard HP-4145B semiconductor parameter analyzer. The experimental setup used is illustrated in figure (5.24). Figures (5.27)(a)-(c), (5.28)(a)-(c) and (5.29)(a)-(c) are the measured IV curves for $device_{xy}$ in the range of -1.5 to 1.5 V. Overall, the curves are the familiar diode IV relationship with a turn-on voltage ranging from 0.25 to 0.42

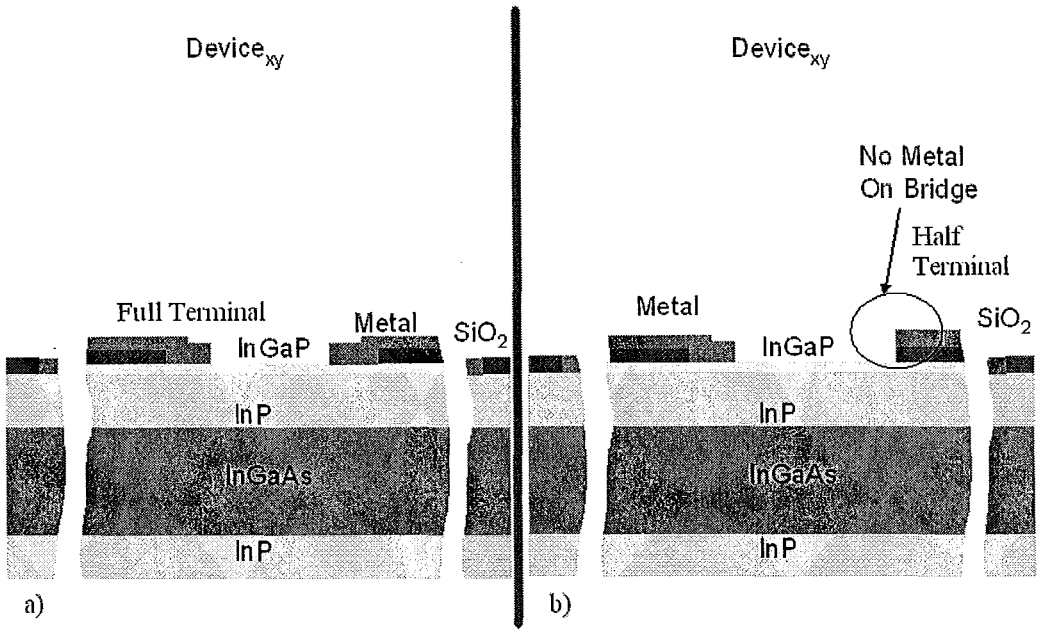

Figure 5.23: Device$_{xy}$ nomenclature. x - bridge number, y - side number:a) bridge with two electrodes on either side, b) electrode on only one side of the bridge

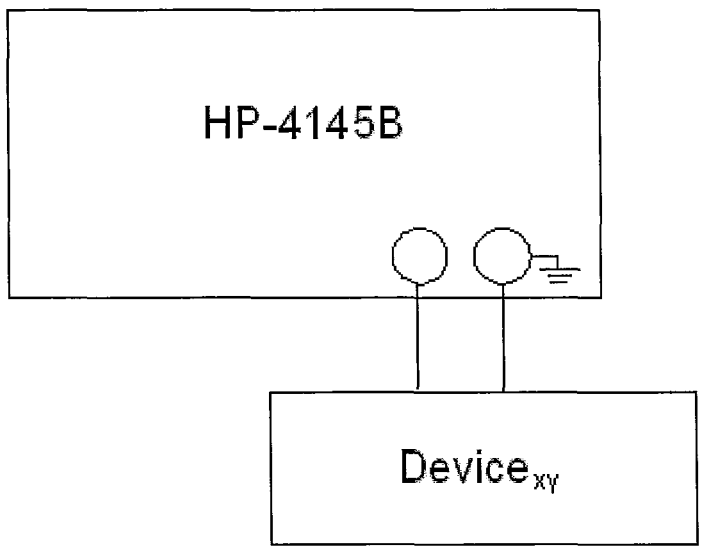

Figure 5.24: Diode IV setup using HP-4145B

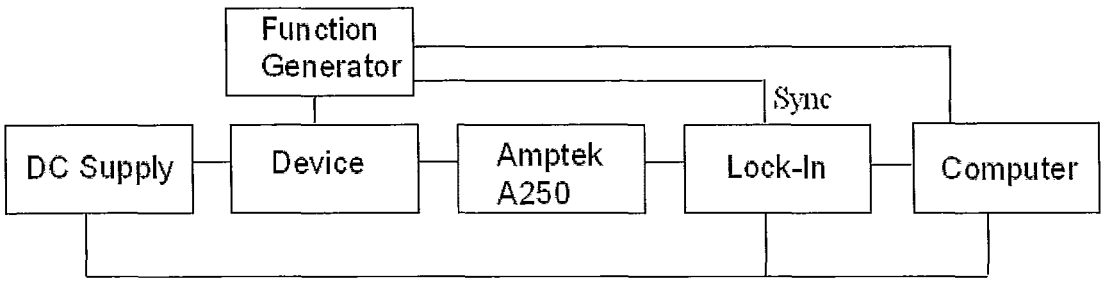

Figure 5.25: InP Experimental Setup

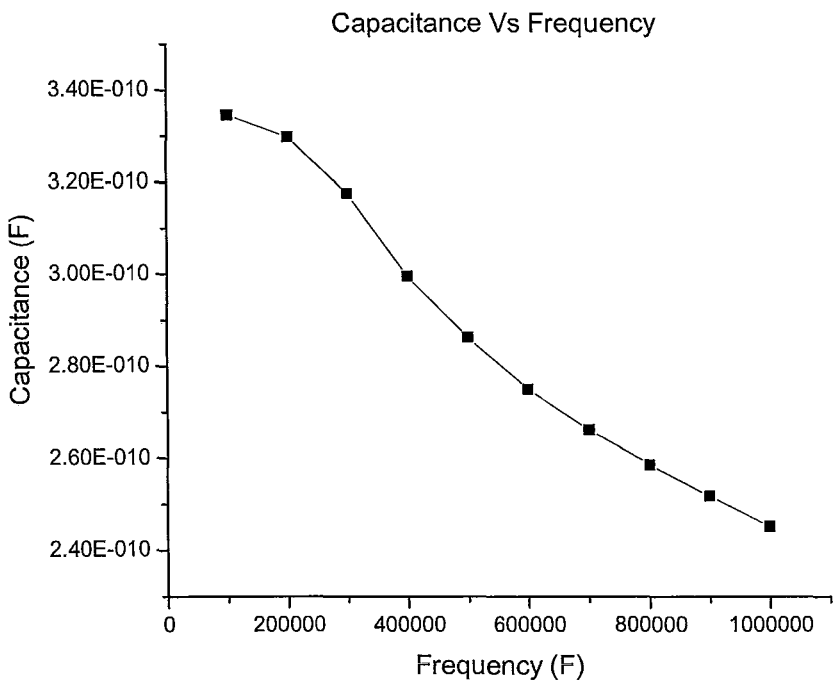

Figure 5.26: Frequency sweep, 200 - 1000 KHz, characterizing the output of A250 using a 331 pF capacitance

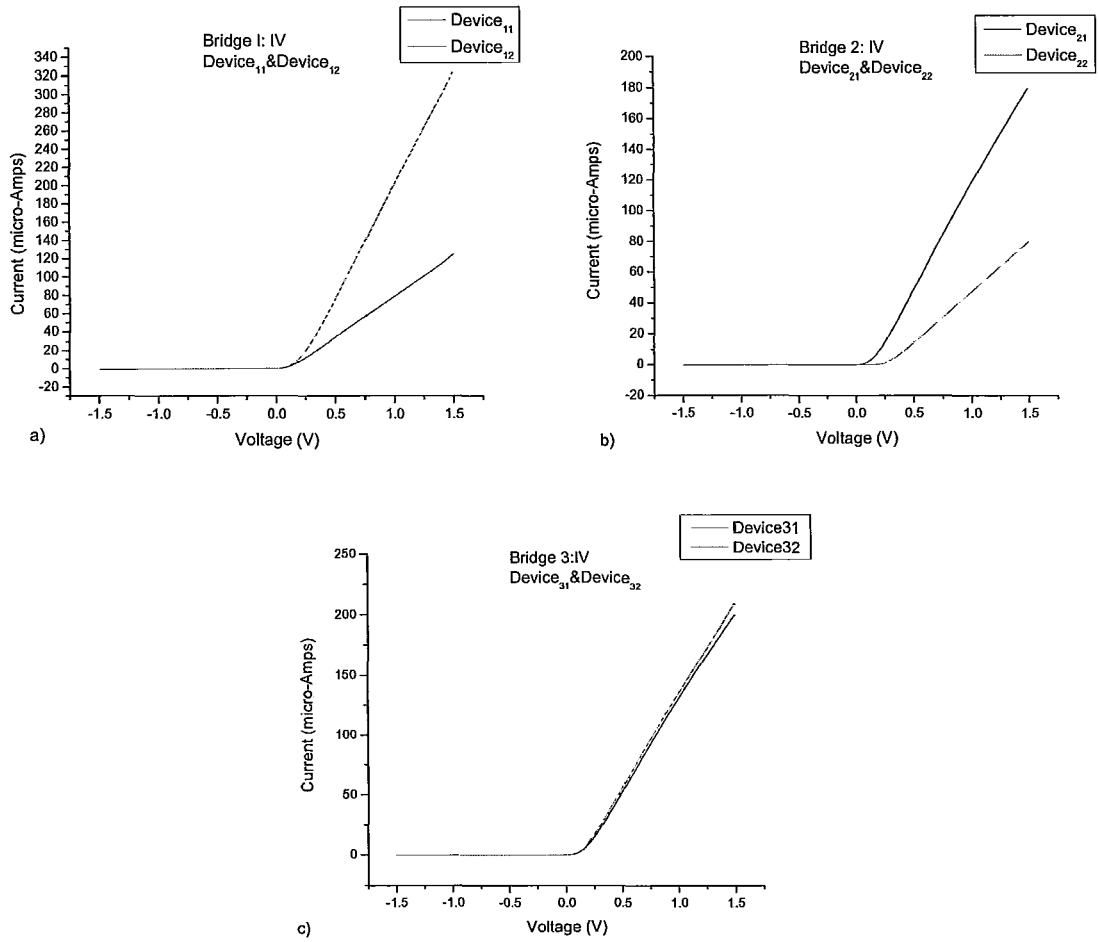

Figure 5.27: Diode IV for 100 μm bridge length (a)-(c)

V. Theoretically a turn-on voltage of 0.42 V is expected. As is seen from the figures, from device to device variation in measured current exists.

In the forward bias regime after turn-on voltage the expected exponential IV behaviour is not measured. The reason could be due to misalignment during fabrication, leading to unwanted touching of the metal to the semiconductor or pinholes in the oxide. To determine the factors, half terminal devices, $device_{22}$, $device_{52}$ and $device_{82}$ are analyzed. In the ideal situation the current from these devices should be zero, owing to the metal being on top of an insulator - SiO_2. This however is not the case. $Device_{52}$ shows higher than normal current for a half-terminal device. Infact, the current is similar to $device_{81}$, figure (5.30). This is a good indication of the predominant factor being misalignment. The IV curves of $device_{41}$/$device_{42}$ and $device_{61}$/$device_{62}$, on either sides of this device, have almost a one to one correspondence. The case for pinholes becomes apparent when analyzing $device_{22}$ and $device_{82}$. The reverse bias current from $device_{82}$ is two hundred times less than the reverse bais current from $device_{22}$ figure (5.31).

Even though the forward bias is not indicative of an ideal diode, the operating point for piezoelectricity is in the reverse bias regime for which all the devices have the expected diode characteristics, figure (5.32)(a)-(c), (5.33)(a)-(c) and figure (5.34)(a)-(c).

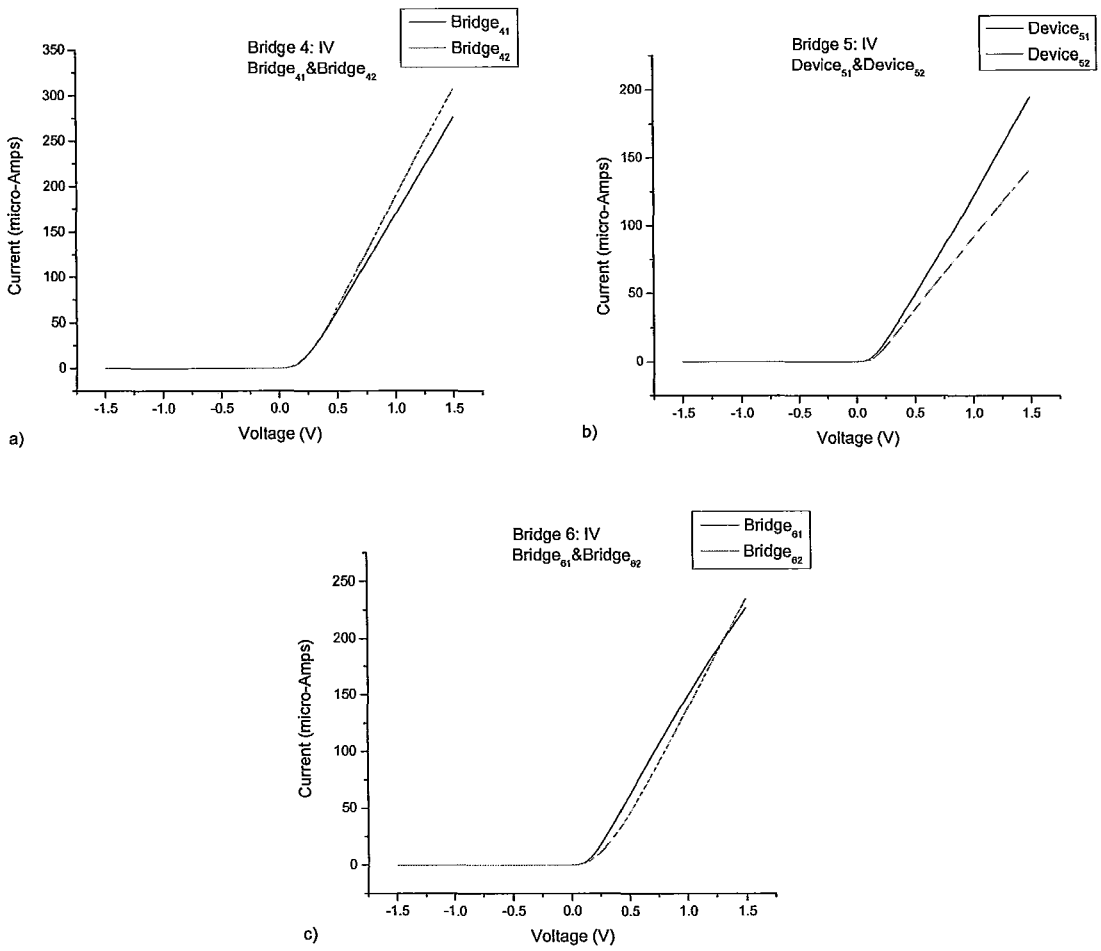

Figure 5.28: Diode IV for 125 μm bridge length (a)-(c)

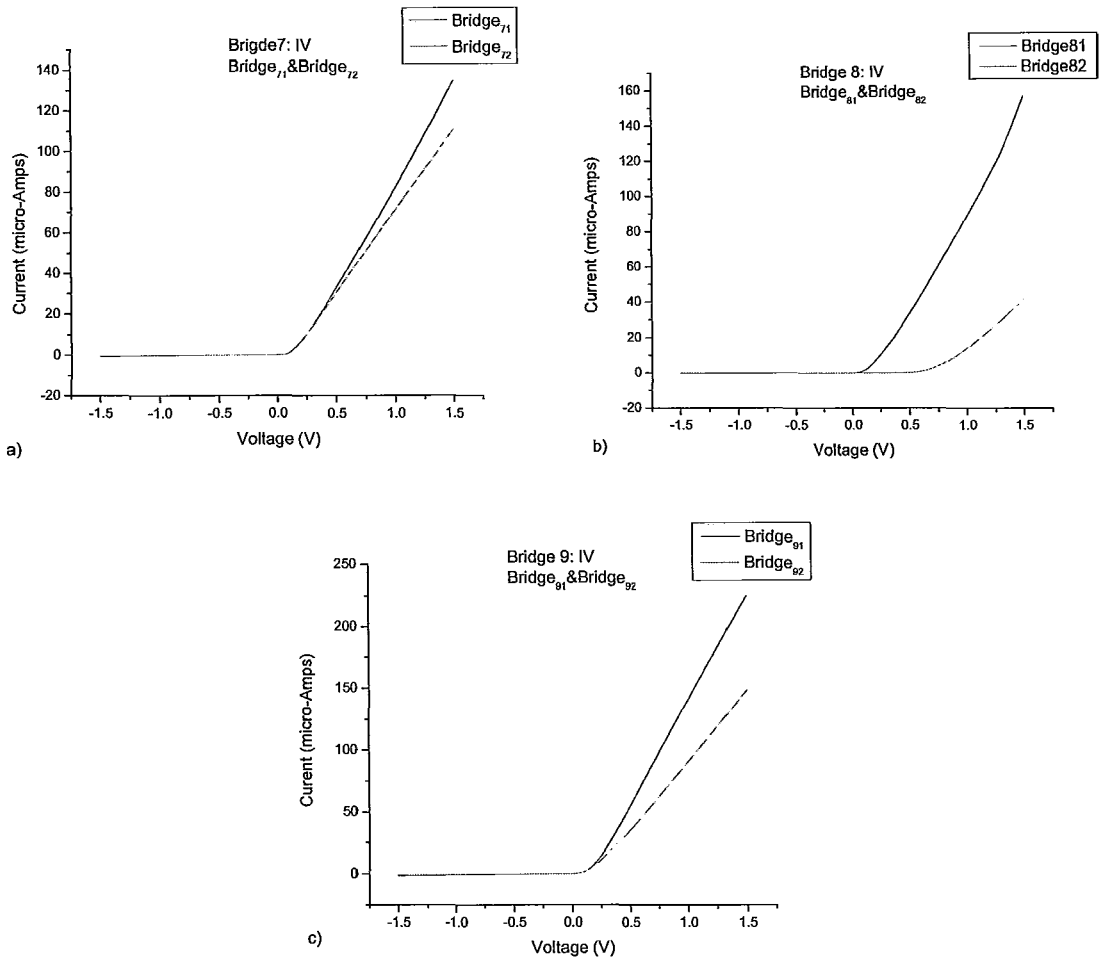

Figure 5.29: Diode IV for 150 μm bridge length (a)-(c)

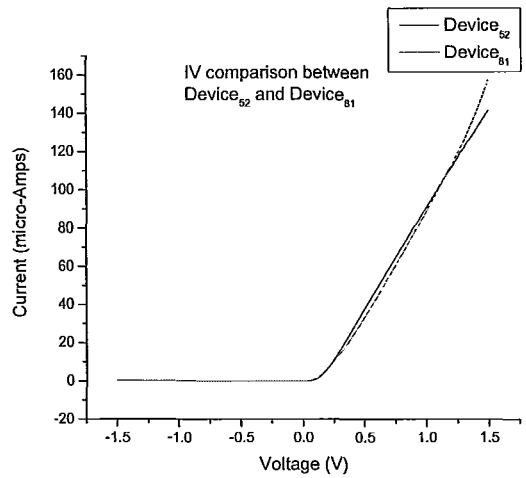

Figure 5.30: Comparison device$_{52}$ and device$_{81}$

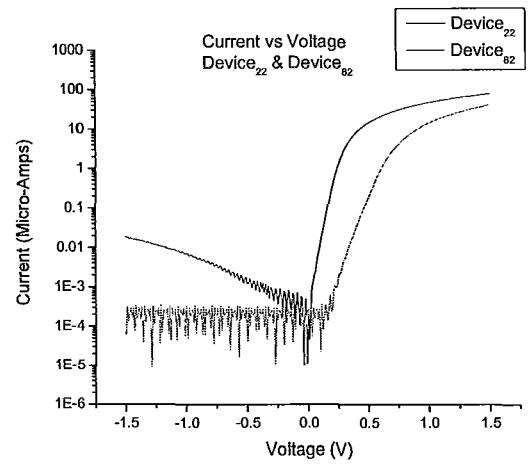

Figure 5.31: Comparison device$_{22}$ and device$_{82}$

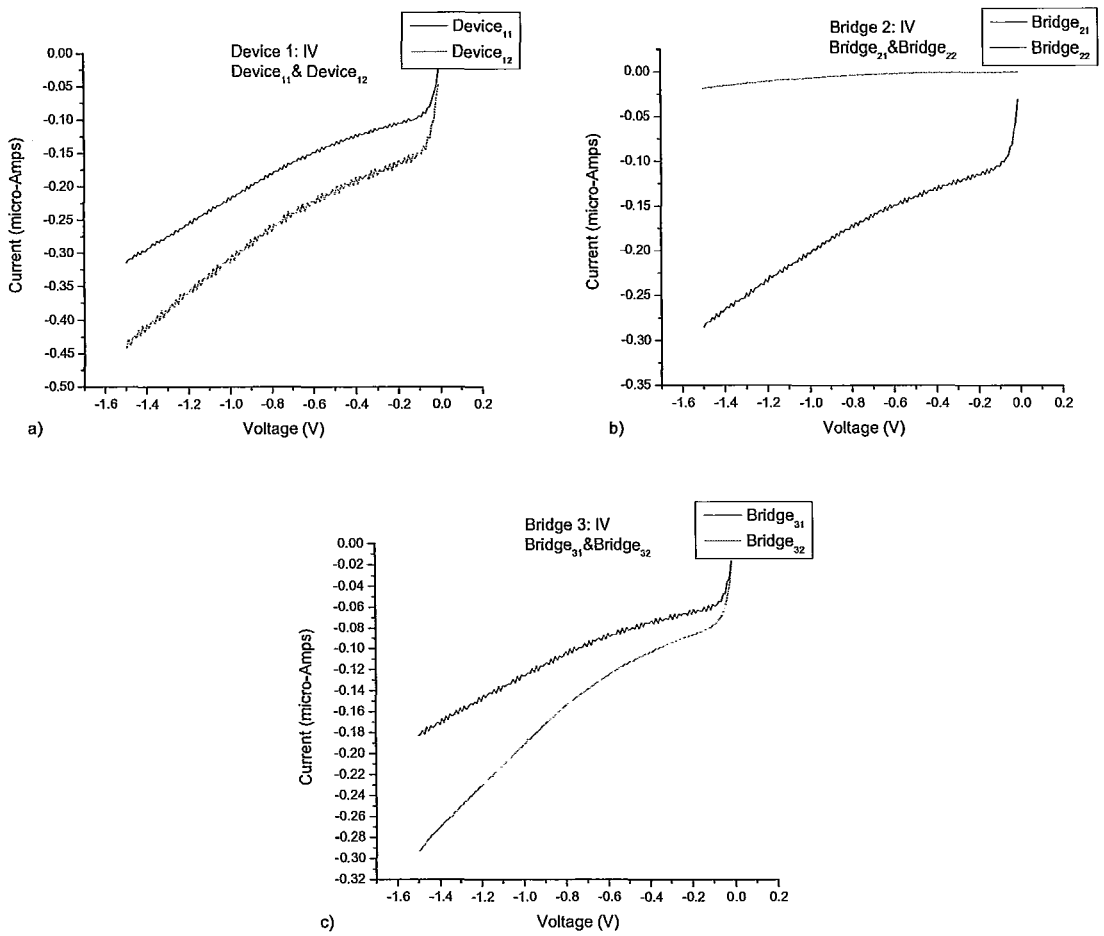

Figure 5.32: Diode reverse IV for 100 μm bridge length (a)-(c)

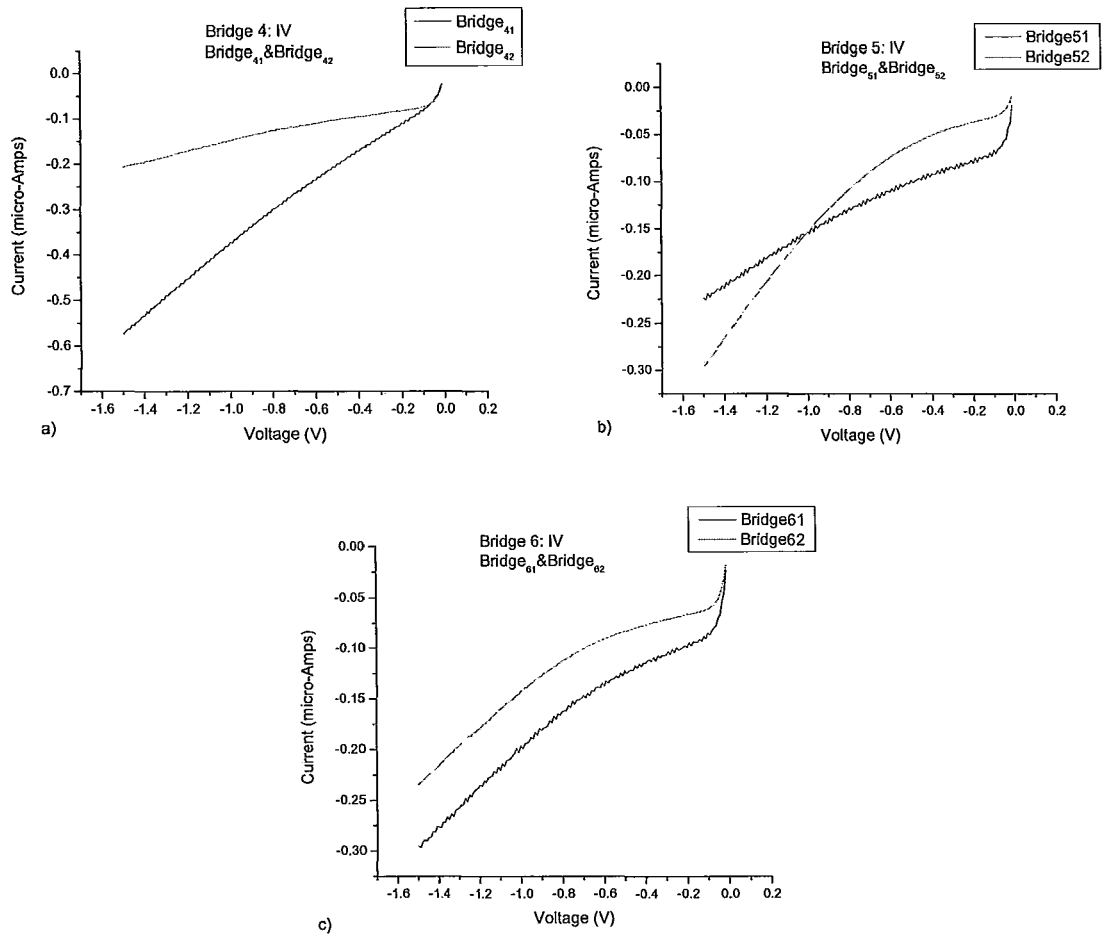

Figure 5.33: Diode reverse IV for 125 μm bridge length (a)-(c)

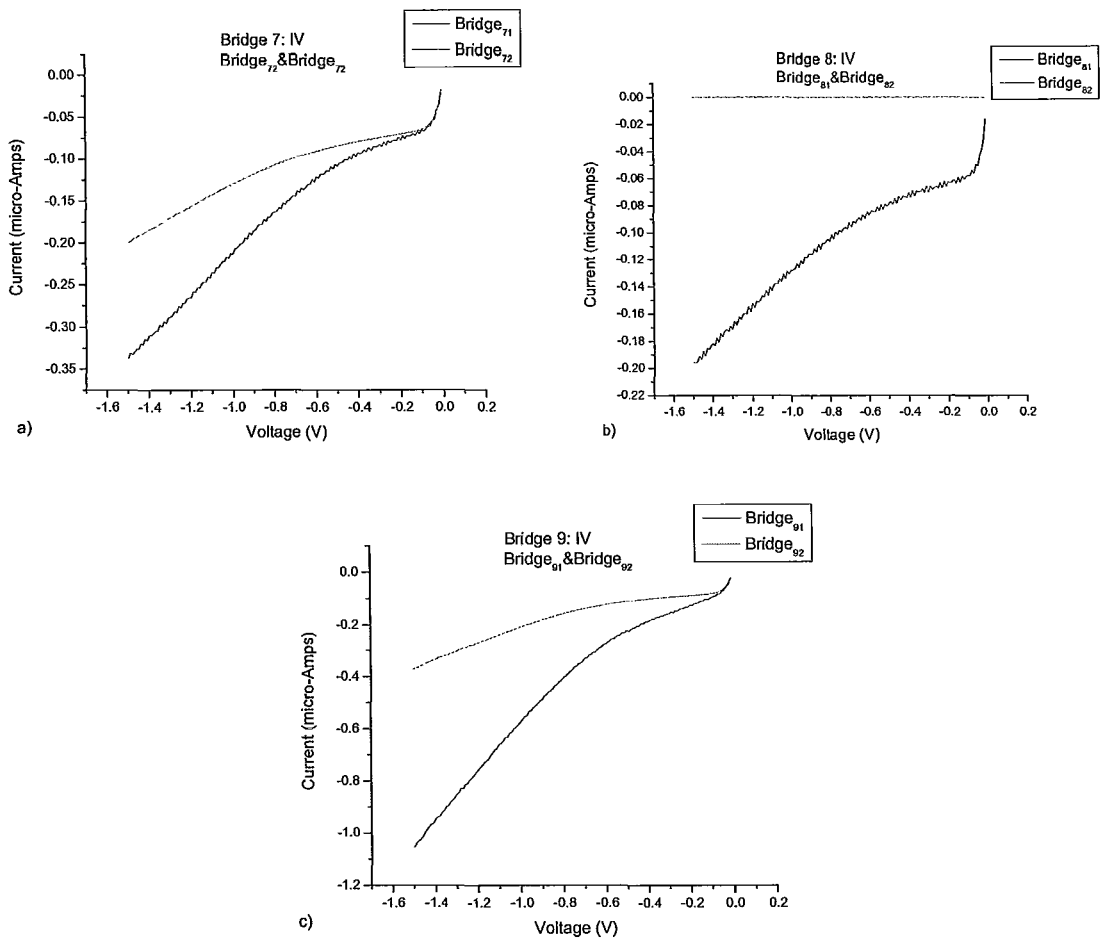

Figure 5.34: Diode reverse IV for 150 μm bridge length (a)-(c)

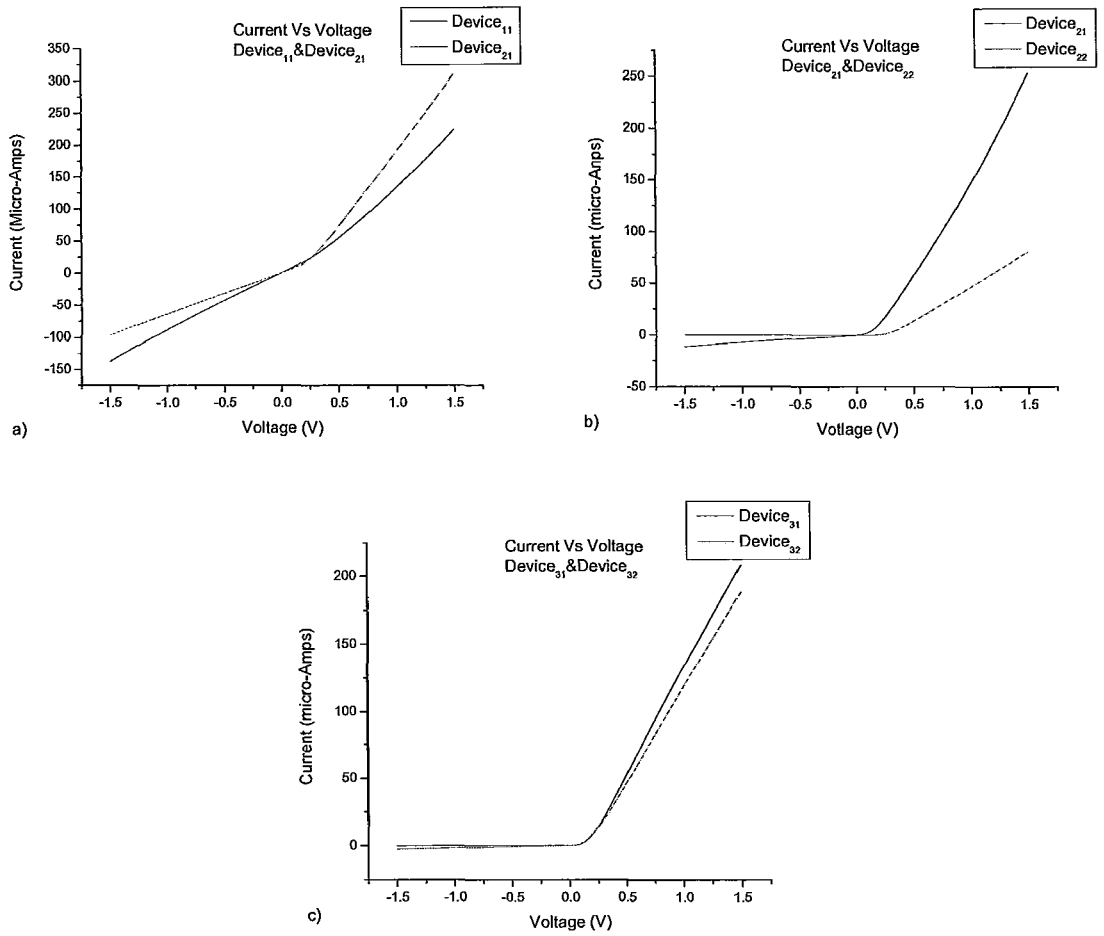

Figure 5.35: Diode IV for $100\,\mu m$ bridge length (a)-(c) after ball bond

Figure (5.35) are the IV curves for $device_{11}/device_{12}$, $device_{21}/device_{22}$ and $device_{31}/device_{32}$ after mounting and ball bonding. The IV of $device_{1y}$ is very different from its non-bonded characteristics. This is attributed to the fact the ball bonder penetrated through the oxide layer creating a resistor in parallel with the diode. $Device_{21}$ after boding also exhibits different characteristics, predominantly both the reverse and forward bias currents have increased. $Device_{22}$ and $Device_{31}$ retain their IV characteristics. $Device_{32}$ reverse bias current increases by an order of magnitude while the forward bias decreases by 0.9 times.

It is difficult to quantitatively understand this non-ubiquity across the sample. Qualitatively, it could be attributed to non-uniform thickness of oxide or metal across the sample, non-uniform force applied by the ball-bonder, parts of the sample being dirty causing loss of adhesion when bonding, greater adhesion in certain sections causing the force after first bond being large enough to break the wire etc.

To continue with experiments $device_{22}/device_{31}$ and $device_{32}$ are deemed fit in reverse bias mode.

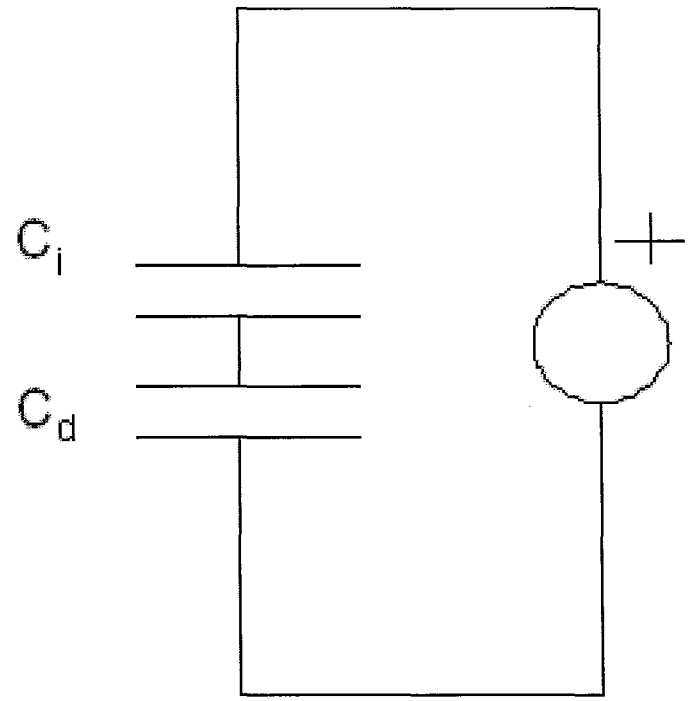

Figure 5.36: MIS circuit model, C_i- insulator capacitance due to SiO_2 and C_d- heterojunction depletion capacitance

5.5.2 Capacitance Measurement

Owing to the MOS and MIS design the capacitance of the ball bonded devices are measured. The ideal model for a MIS, figure (5.36), is an insulator capacitance, C_i, in series with a depletion capacitance, C_d. Therefore, in forward bias mode the measured capacitance is the insulator capacitance and in the reverse bias mode the measured capacitance is the series combination of insulator and depletion capacitance. Figure (5.37) is the setup used to measure capacitance. The idea being the capacitance at various bias voltages is measured. To do this the DC bias is set by V_{DC} while the AC voltage is set by V_{AC}. Keeping V_{AC} fixed a V_{DC} sweep is made from -0.5 ... 0.5 V. Measurements are made at V_{AC} equivalent to 7, 14 and 35 mVrms at 600 KHz.

The oxide capacitance theoretically is 163.12 pF because of the 3000 Å thick SiO_2 and the area of the electrode pads equivalent to 2.46×10^{-6}. The capacitance due to the heterojunction is plotted in figure (5.38) using the same electrode area and equation (5.1). As seen the heterojunction capacitance is much larger than oxide capacitance in both reverse and forward bias. Therefore, through circuit analysis of figure (5.36), the oxide capacitance should dominate in the measurements.

$$C = \frac{\epsilon_r \epsilon_o A}{d} = \frac{(2.25)\left(8.85 \times 10^{-12}\right)\left(500.0 \times 10^{-6}\right)\left(4.915 \times 10^{-3}\right)}{\left(3000.0 \times 10^{-10}\right)} = 163.12 pF$$

The C-V curve for $device_{22}$, figure (5.39)(a), is not as expected. The difference in capacitance from reverse to forward is 1.3 pF. This capacitance difference could be due the heterojunction capacitance not being as large as theoretically predicted. The maximum capacitance measured is at -0.1 V. In the forward bias regime the capacitance decreases with increase bias voltage. This could be attributed to charges in the oxide layer, parallel resistance due to pinholes etc. As stated above the capacitance due to the oxide layer is 163.12 pF. However the maximum measured value

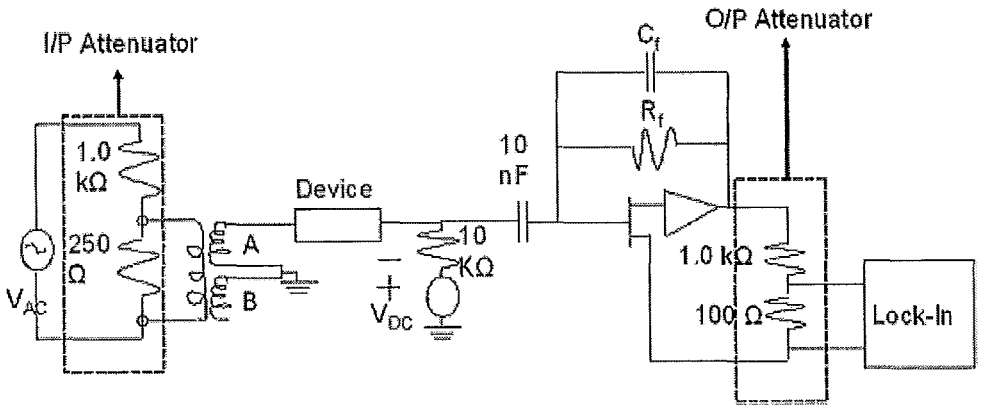

Figure 5.37: Capacitance experimental setup

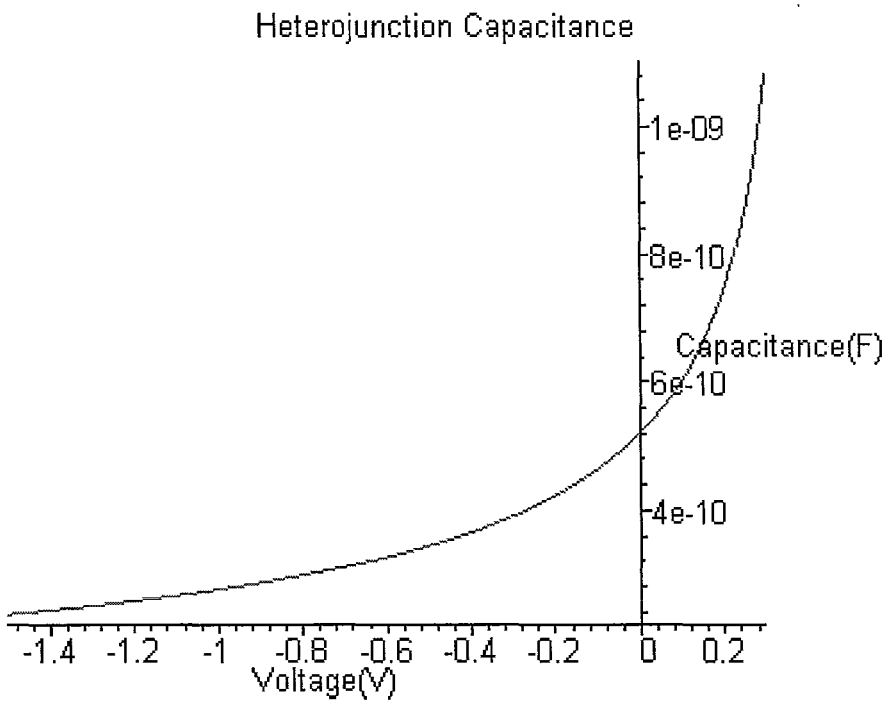

Figure 5.38: Theoretical heterojunction capacitance

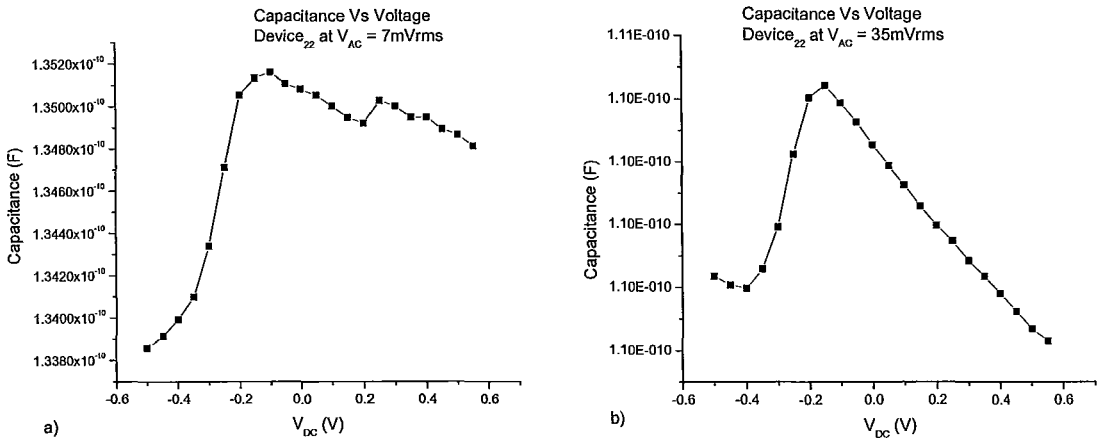

Figure 5.39: Capacitance vs V_{DC} for device$_{22}$ at (a) 7mVrms and (b) 35mVrms

in forward bias is 135.160 pF or 17.14% lower than the theoretical value. It was also found the capacitance changes with V_{AC}. Figure (5.39)(a) is a plot of capacitance for a drive voltage of 7 mVrms. Increasing the drive voltage to 14 mVrms yields the same result (not shown). However when the drive voltage is increased to 35 mVrms, figure (5.39)(b), the result is quite different. The maximum capacitance value shifts to -0.15 V from -0.1 V and decreases by 18.29%. The capacitance in the forward bias regime decrease linearly. This oddity is hard to explain.

Measuring device$_{31}$ the expected electrical equivalent circuit is an insulator capacitor, C_i in parallel with the depletion capacitance, C_d, due to the Schottky diode, figure (5.40). The hetero-junction capacitance is ignored in this model. Figure (5.41) is the theoretical predicted values for the Schottky capacitance. Therefore in the reverse bias mode the measured capacitance should be a combination of insulator capacitance and Schottky capacitance and in the forward bias mode the insulator capacitance should dominate.

Figure (5.42)(a)-(b) is the C-V curve of device$_{31}$ and agrees with the above theoretical assertion. Unlike device$_{22}$ at 0.0 V the capacitance is a maximum at 157.144 pF. This capacitance is 3.66% lower than the theoretically predicted oxide capacitance. A 4.8 pF change in capacitance occurs from reverse to forward bias. Changing V_{AC} to 35 mVrms figure (5.42)(b) the curve remains the same but the capacitance decreases by 25.30%. The change in capacitance from reverse to forward is 2.84 pF a decrease of 40.83% from the 7 mVrms case. This change due to applied V_{AC} is also seen in device$_{22}$. The expected change in capacitance, calculated theoretically using equation (5.4), is roughly 35.86 fF.

Subtracting the capacitance digitally, data from device$_{31}$ from data from device$_{22}$, analogous to removing the background insulating capacitance, yields figure (5.43). A change in capacitance of 3.0 pF exists from reverse to forward bias. Therefore choosing a bias voltage of -0.1 V the piezoelectric measurements are made.

5.6 Piezoelectric

The insulator capacitance in combination with the depletion capacitance is the package capacitance. In order to measure the piezoelectric signal the contributions from this capacitance must be negated. This is achieved by using a bridge circuit which consists of a transformer. The transformer yields two waveforms phase shifted from each other by 180^0. By adjusting the capacitance on one arm of

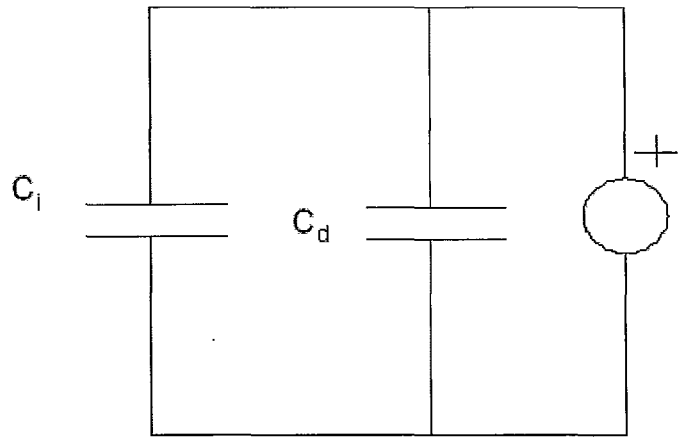

Figure 5.40: Equivalent circuit model for electrode on the bridge. C_i- insulator capacitance due to SiO_2 and C_d- Schottky depletion capacitance

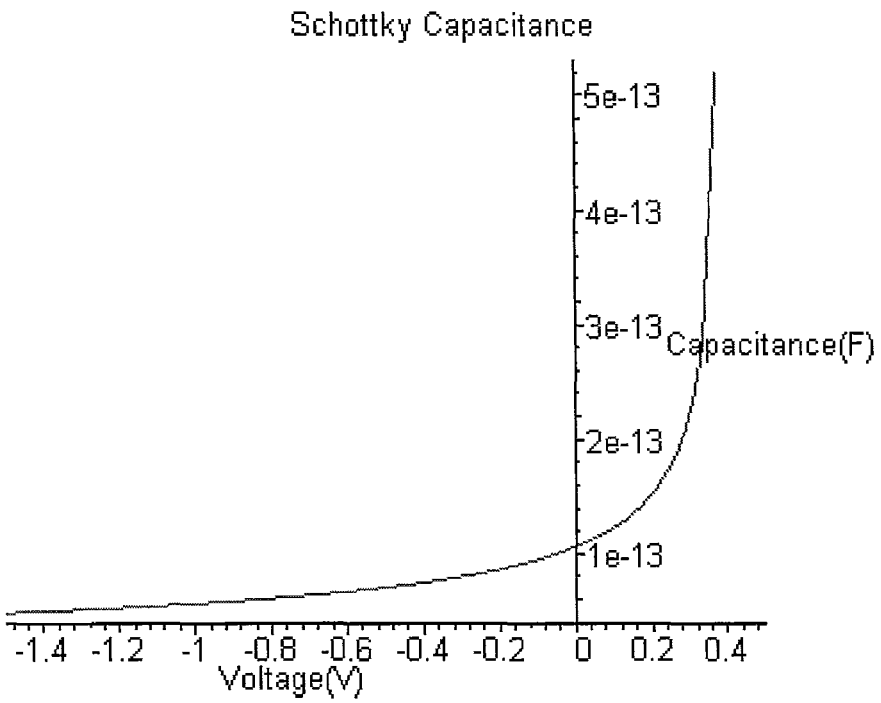

Figure 5.41: Theoretical Schottky capacitance

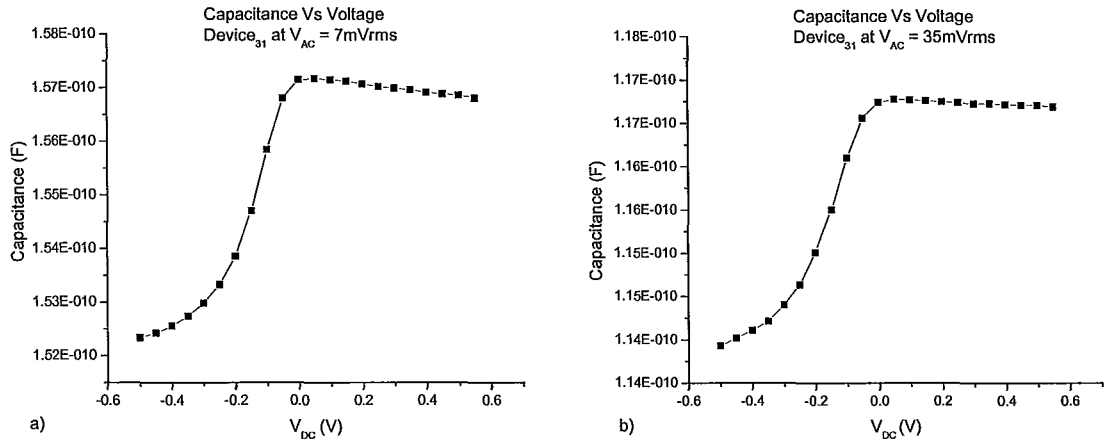

Figure 5.42: Capacitance vs V_{DC} for device$_{31}$ at (a) 7mVrms and (b) 35mVrms. Capacitance at 35 mVrms is 25.30% lower than at 7 mVrms

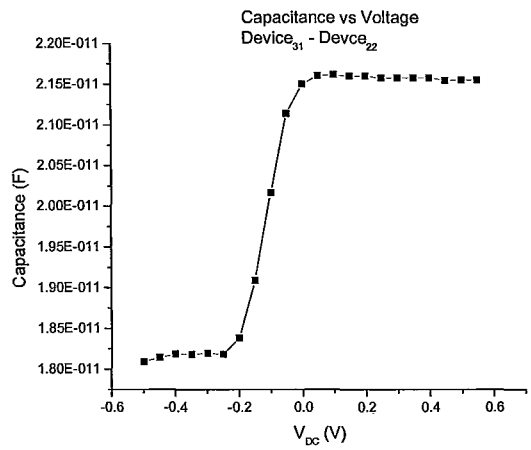

Figure 5.43: Capacitance vs V_{DC} of device$_{31}$-device$_{22}$

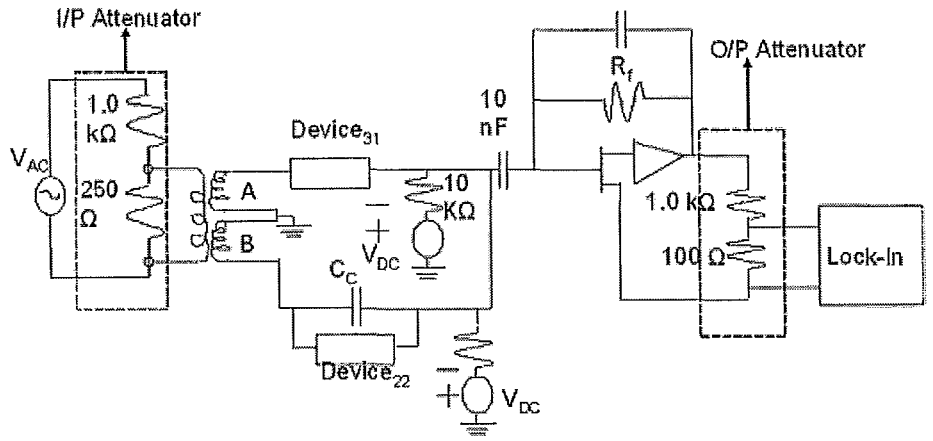

Figure 5.44: Two terminal bridge setup. Piezoelectric response of $Device_{31}$ is measured while $Device_{22}$ parallel with C_C are the compensating arm to negate the package capacitance

the bridge the current through the package capacitance can be negated by the current in the variable capacitance. The piezoelectric characteristic is measured using a two terminal and a three terminal setup.

5.6.0.1 Two Terminal

Motivation

The idea is to treat the device like a quartz tuning fork and measure the piezoelectric response form one arm of the InP bridge.

Experimental Setup

The experimental setup is illustrated in figure (5.44). The bias voltage, V_{DC}, is fixed at -0.1 V and a frequency sweep V_{AC} equivalent to 7.05 mVrms from 400.0 to 700.0 KHz is made. The idea of the setup is one arm contains $device_{31}$ whose piezoelectric response is being measured and the other arm contains $device_{22}$ in parallel with a variable capacitance to negate the package capacitance.

Result

Figure (5.45) is a plot of the measured output voltage vs frequency for $device_{31}$ and $device_{22}$ without compensation. The measured output voltage is roughly 100 times greater than the input voltage. Figure (5.46) is a plot of the compensated output (red curve). The signal is reduced by 22.0 times however the voltage increases with frequency. To improve this a 5.0 pF compensating capacitance, C_c, is added in parallel to $device_{22}$, figure (5.46) (black curve). This reduces the compensating signal by 30 times or an equivalent package capacitance of 5.2 pF.

Both the curves yield a change in trend between 500 and 600 KHz, hinting at some piezoelectric effect. The theoretical resonance frequency is roughly 584.0 KHz. Although promising, this setup had to be abandoned because a stable secondary DC source was not available. The secondary DC source used had voltage drift issues and setting voltages in the milli-volt range was difficult. More importantly, the resonant resistance cannot be lower than the equivalent impedance of the package capacitance - 52.41 kΩ. This would yield a Q-value of greater than 2000. A Q-value of 1000 or lower is expected.

The three-terminal setup is adopted.

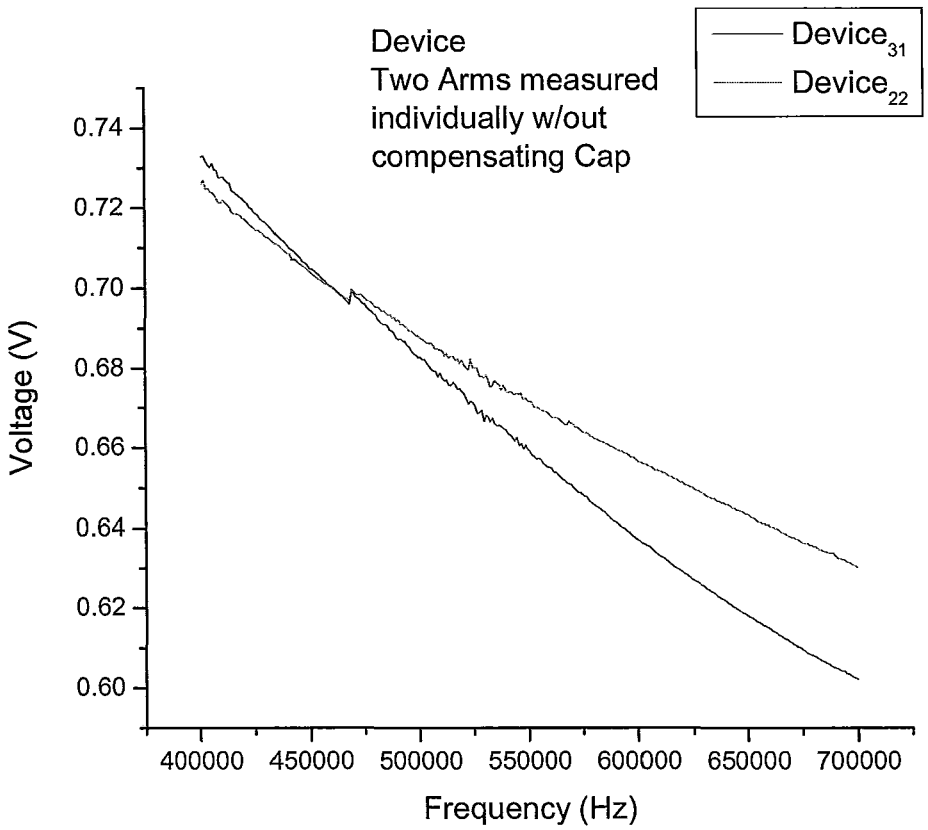

Figure 5.45: Two terminal individual device$_{31}$ and device$_{22}$

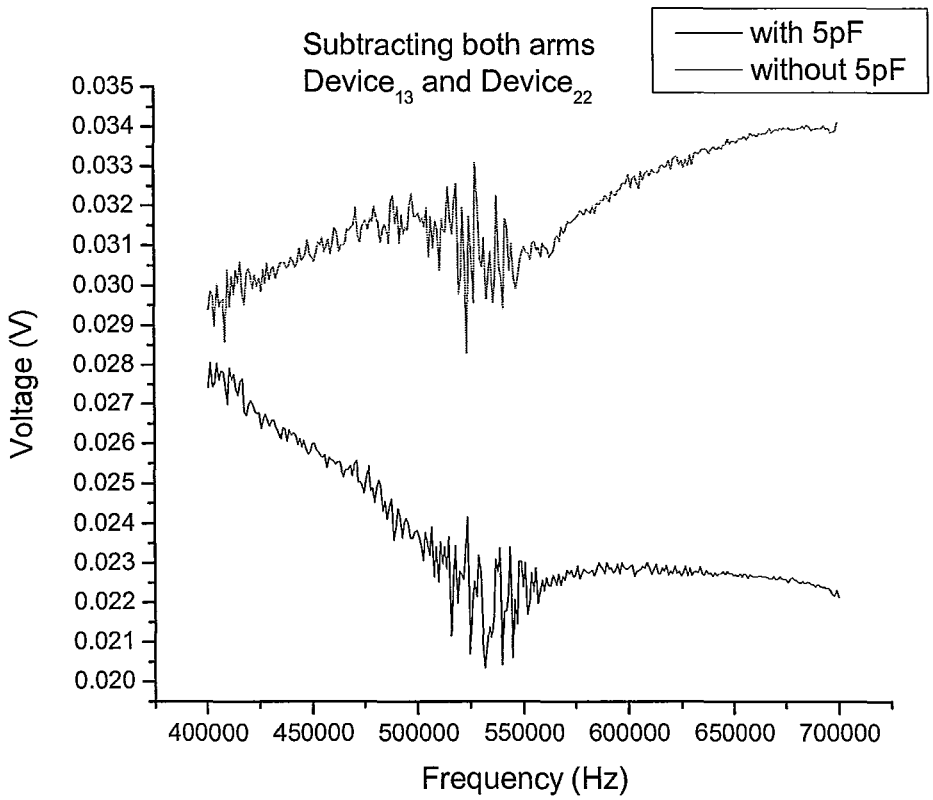

Figure 5.46: Two terminal subtracted with/without compensating capacitor

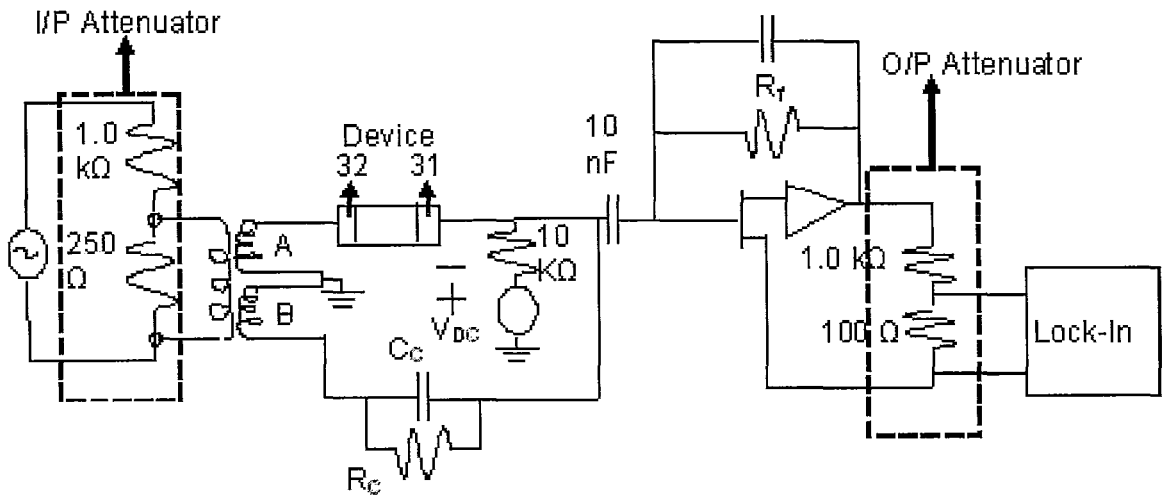

Figure 5.47: Three terminal bridge setup. $Device_{31}$ is driven while $device_{32}$ is measured. The compensating arm consists of a variable capacitance and resistor - C_C, R_C.

5.6.0.2 Three Terminal

Here three terminal means measuring the output voltage of one device while its associate is being driven. In this case $device_{31}$ is driven while $device_{32}$ is being measured. This is done using two approaches: transformer bridge method and 3-term method. The transformer method is first explained.

Transformer Bridge Method

Experimental Setup

The setup, figure (5.47), is similar to the two-terminal setup. The difference is the compensating arm is a combination of resistors and capacitors in series and parallel. Here $device_{31}$ is driven with a voltage of 7.05 mVrms while $device_{32}$ is measured. Both devices are biased at -0.1 V_{DC}.

Results

The method of compensation is as follows:

1. starting with a known capacitor in the compensating arm the output signal is measured at a specific frequency, this case 600.0 KHz
2. capacitance is increased till adding a capacitor increases the output signal
3. once achieved resistors are added in parallel or series to further reduce the signal
4. this is done till adding either component increases the compensated signal.

Using this technique the signal is reduced by 182 times or a compensating capacitor of 0.893 pF. Figure (5.48) is the output of the above setup with a step size of 1.0 KHz. The inset is data taken at 100 Hz. A 'V' shape is seen which is expected because the compensation is done at 600.0 kHz. Experimentally, however, the compensation is at 584.0 KHz. Unfortunately, no resonance is seen. C_c is 186 pF and R_c is 5.0 kΩ. To verify that depletion is occurring and the package capacitance is compensated the bias voltage is changed to -0.5 V and 0.0 V. For the latter a shift in the voltage frequency curve should be small but the former should exhibit a large shift. Figure (5.49) illustrates this result.

3-Term Method

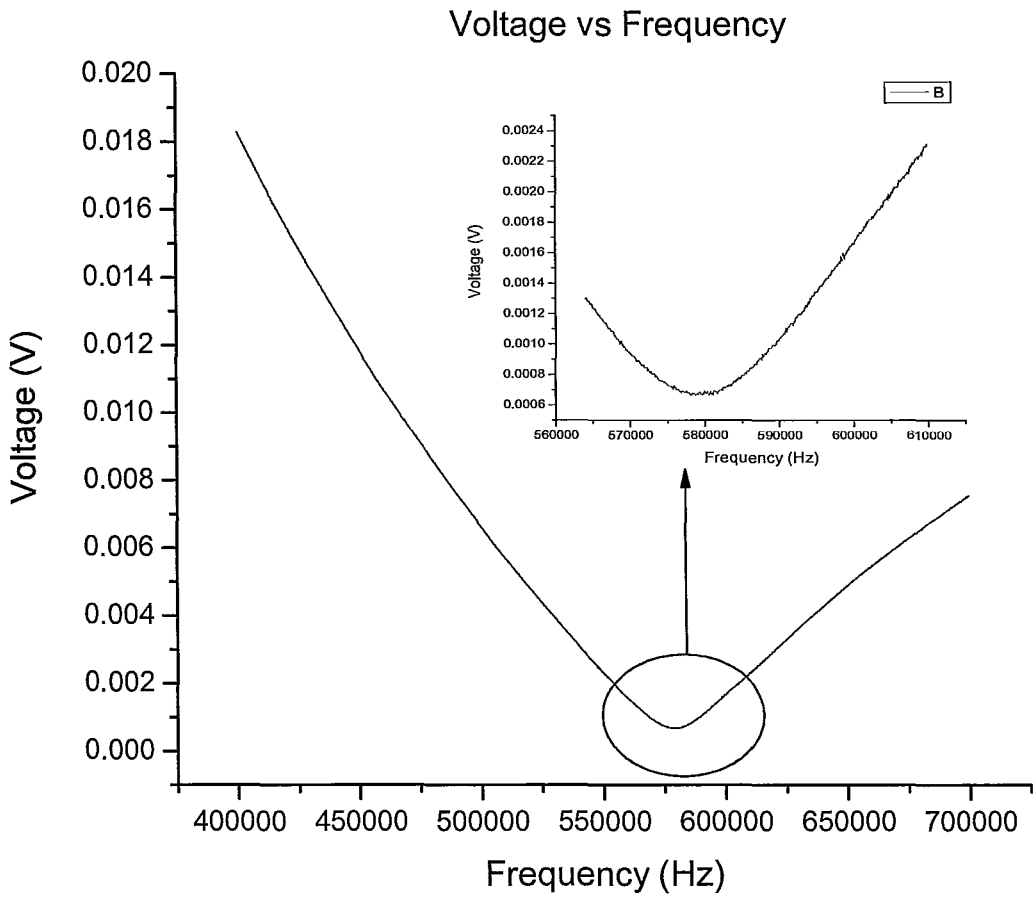

Figure 5.48: Device_{32} compensated at 584.0 kHz using setup described in figure (5.47)

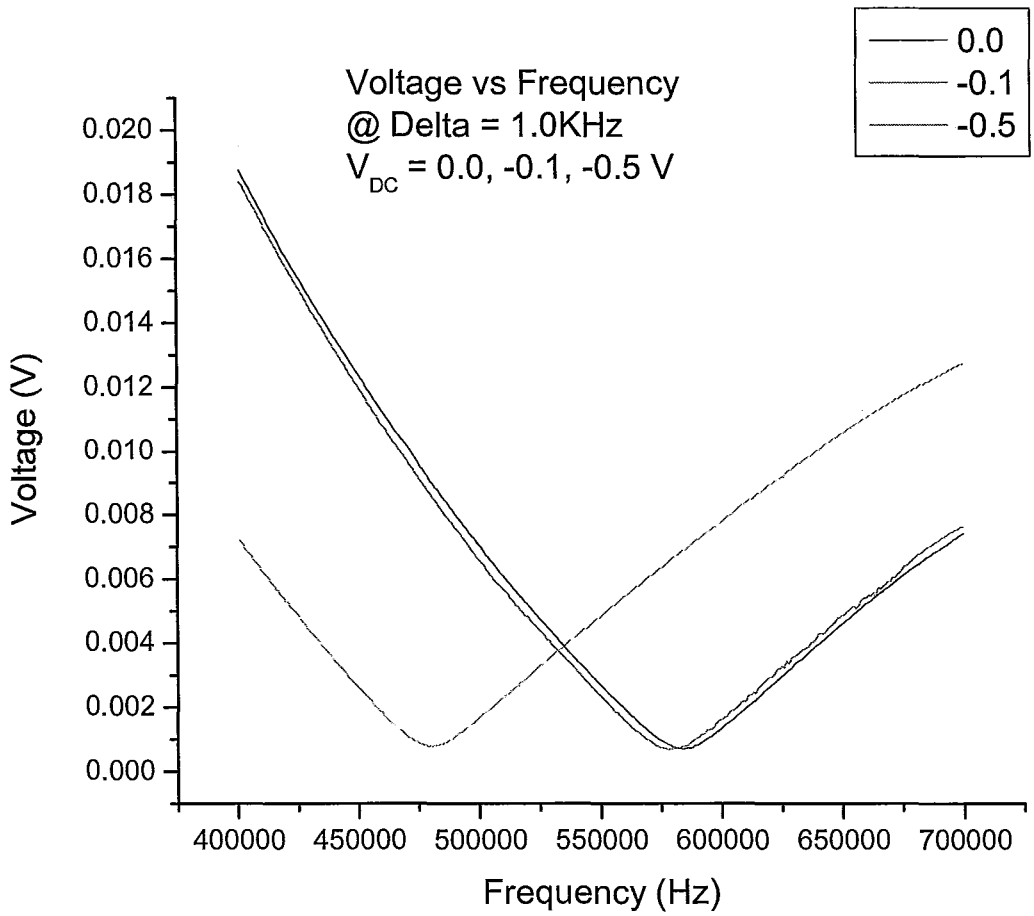

Figure 5.49: $Device_{32}$ compensated at 584.0 kHz for V_{DC} -0.5, -0.1 and 0.0 V using setup described in figure (5.47)

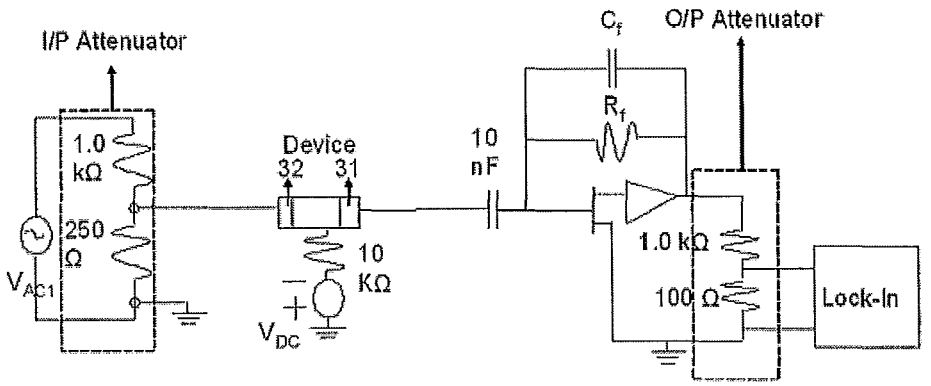

Figure 5.50: 3-Term setup. Piezoelectric response of device$_{31}$ is measured while device$_{32}$ is driven. The package capacitance in between device$_{31}$ & device$_{32}$

Similar to the above setup but the resonance is measured not with respect to ground but with respect to virtual ground of the op-amp. The package capacitance is the capacitance between device$_{31}$ and device$_{32}$. This capacitance will be much lower because the separation between the electrodes is greater than or equal to 50μm leading to a capacitance of 13.806×10^{-18} F or 11.08×10^{6} times lower. This setup is similar to the idea described in the previous chapter.

Experimental Setup

Figure (5.50), illustrates the setup used. In this setup the ground of device$_{31}$and device$_{32}$ are connected to the bias potential V_{DC}. A bias potential of -0.1 V is applied. V_{AC} of 7.05 mVrms is applied to device$_{32}$. Output from device$_{31}$ is measured. This point with the 10.0 nF is held at virtual ground.

Result

Figure (5.51) is the capacitance vs bias voltage. There are two oddities with this result: (a) the value of the capacitance is about one million times larger than the expected result and (b) the capacitance increases as the bias voltage is increased when it should remain constant. This basically means within the bridge or in the measurement setup stray capacitance's exist impeding the measurement of the real capacitance. Figure (5.51) is a frequency sweep of capacitance vs voltage. Resonance is not detected. In order to determine the reason for this oddity another device was bonded and tested. However the bond punched through the metal making making it impossible to determine the reason. However using the three terminal setup did reduce the package capacitance by an order of magnitude.

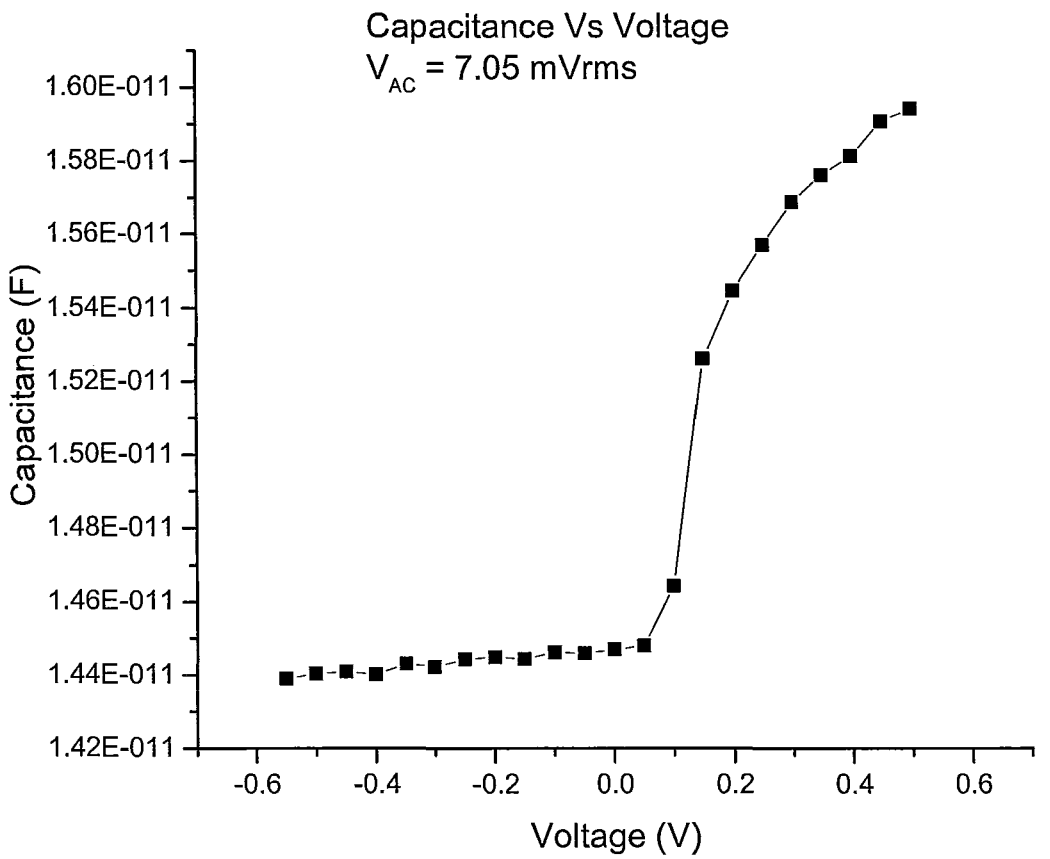

Figure 5.51: Capacitance vs V_{DC} for 3-term setup

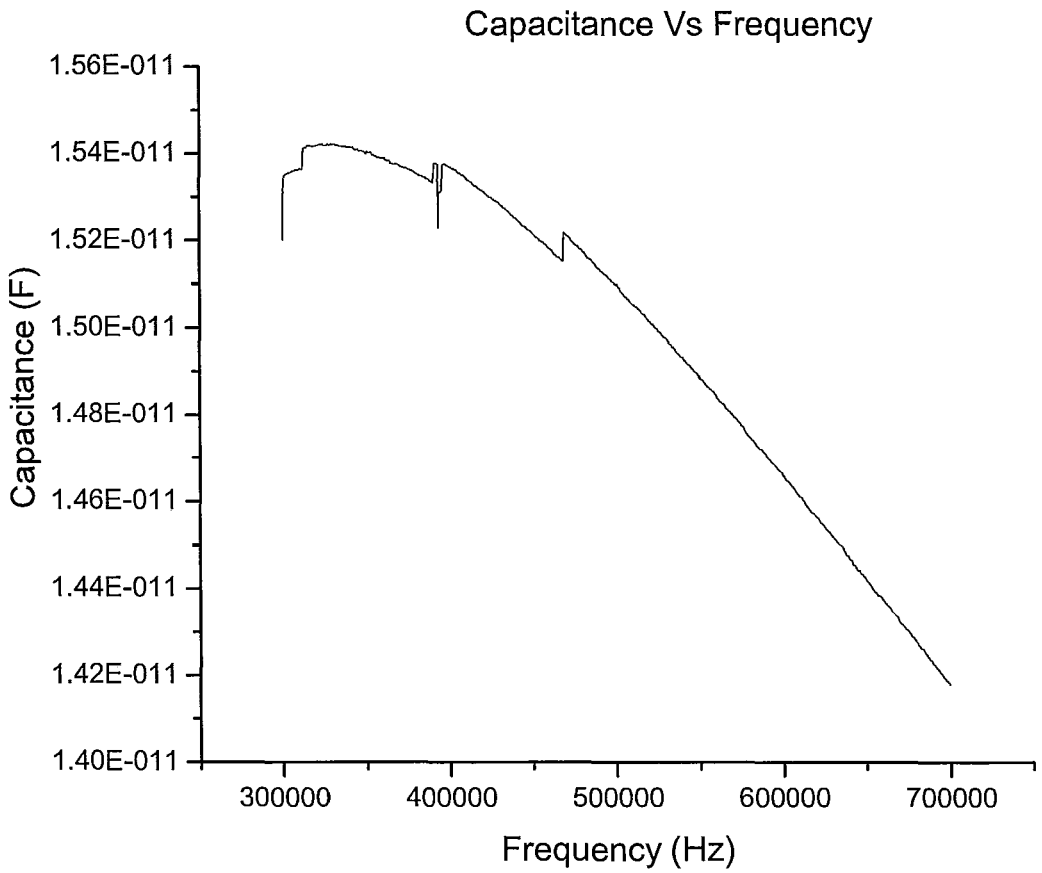

Figure 5.52: Capacitance vs Frequency for 3-Term setup

Chapter 6

Conclusion and Future work

In this research work MEMS resonators, cantilevers and bridges, using the piezoelectric effect to drive and detect fundamental resonance was presented. The piezoelectric effect is defined as materials lacking a symmetry center regarding the positive and negative ions of the crystal lattice. As a result an applied mechanical force or an electric field causing deformation results in a detectable charge. The latter is called the inverse piezoelectric effect. The type of deformation of interest is flexural and based on this a general theory relating the bending moment produced due to the piezoelectric stress was presented. Using this bending moment a general expression for deflection and charge was derived. Resonators made from $\alpha-$quartz and InP were investigated.

The quartz resonator investigated is the conventional quartz tuning fork (QTF) found in watches. This device is an example of a two-terminal parallel bimorph device with electrodes placed on either face creating equal and opposite fields. The field are produced in x-direction resulting in a flexural deformation in the x-direction or XY plane. A theoretical model was made to explain this and compared with the Ansys and experimental results for good agreement. The model assumes the tines can be treated as cantilevers. The theoretical dielectric or package capacitance is found to be an order of magnitude larger than the experimental. This is attributed to the electrodes not extending to the complete length, width and height of the tine.

The InP resonators investigated were designed and fabricated in-house using intrinsically grown MBE layers of 4.0 μm $In_{0.53}Ga_{0.47}As$, 1.67 μm InP and 100 Å $In_{0.85}Ga_{0.15}P$ on a semi-insulating InP substrate. The design was based on a three terminal device where one electrode was used to drive the device, other to detect and a third one for ground. Inorder to induce piezoelectricity a depletion width was created serving the role of an insulator. A 109.56 nm naturally occurring depletion width is created between the $InP/In_{0.85}Ga_{0.15}P$ heterojunction layer. Schottky contacts were used as electrical contacts increasing the depletion width and giving the ability to control the thickness of the depletion region or the thickness of the piezoelectric layer hence making it a monomorph piezoelectric device. The resonators fabricated were bridges having dimension of $(l \times w \times t)\,\mu m$ $100 - 150 \times 30 \times 1.68$ using standard fabrication techniques - CVD, optical lithography, metalization and wet chemical etching. Bridges were fabricated to use the three terminal design. The piezoelectric resonance was not measured due to parasitic resistances and charges. Pin holes were measured in the SiO_2 layer which is very puzzling because InP is considered to be the most promising III-V compounds for MIS device application[39]. Additionally good quality plasma oxide have been reported by[40] for the production of MIS schottky diodes. Measuring using the three terminal setup did however result in a 66.67% decrease in package capacitance from the two terminal setup. The expected deflection was to occur in the XY plane or z direction due to an applied z-directed electric field. A theoretical model was made for both cantilevers and bridges. The deflection and piezoelectric charge for a cantilever was found to be 32 and 13.7 times larger than the bridge case which is expected given the increased stiffness of a bridges. Additionally, the model took

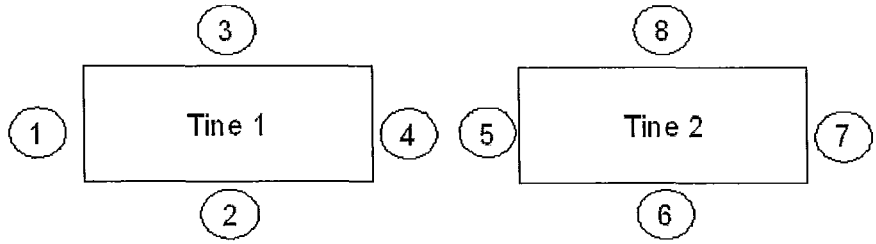

Figure 6.1: QTF electrode cross-section

into account the changing depletion width and in both the cantilever and bridge case a piezoelectric layer which is thinner than the elastic layer resulted in maximum deflection.

6.1 Future Work

6.1.1 Three terminal QTFs

A QTF is actually an eight terminal device, four electrodes, on each arms. Figure (6.1) is a cross-section of the tines with electrodes numbered from 1 to 8. In the conventional two terminal setup electodes 1, 4, 8 and 6 are connected to terminal A and electrodes 3, 2, 5 and 7 are connected to electrode B. Inorder to make this a three terminal device electrodes 3, 2, 8 and 6 are held at ground, while 1 and 7 are connected to make one terminal and 4, 5 connected to make another one. Either of these terminals can be drive and detect. The field produced in tine 1 will be opposite the field produced in tine 2 producing the same movement of tines as in figure (3.4). The advantage of this setup is the package capacitance should be four orders of magnitude lower than the two terminal case table (4.1) while the piezoelectric capacitance changes by 4.0%.

6.1.2 Passivating $In_{0.85}Ga_{0.15}P$ Surface

One of the problems with the InP MEMS resonator is the existence of pinholes making it hard to measure resonance. According to [41] a silicon layer four to ten monolayers thick can be grown on (100) GaAs and SiO_2 can deposited using PECVD technique at 275°C. During the deposition process some of this silicon is consumed to from the native oxide. Using this technique a 300 Å thick SiO_2 film is grown. At bias voltage of 30.0 V a current 0.1 μA is measured while at lower bias voltages, for example 7.5 V, a current of 1 pA is measured. The C-V curves also show the expected MOS characteristics. Perhaps using the available MBE the $In_{0.85}Ga_{0.15}P$ layer can be highly doped with silicon making it basically a silicon layer. This can then be used to grow oxides during the fabrication process. The foreseeable problems with this idea are: (a) how much of the silicon gets consumed during CVD, (b) what is the diffusion rate of silicon in $In_{0.85}Ga_{0.15}P$ and InP during the CVD process when the temperature is increased, (c) how thick a layer of silicon is required for growing oxide three times. If this technique proves to be successfull then a passivating film can be grown thereby eliminating one of the issues towards measuring the piezoelectric effect.

6.1.3 Fabrication of cantilevers or longer bridges

As shown from the calculations cantilevers or longer bridges will result in higher charges and deflection. If cantilever's are fabricated the 3-terminal method described in chapter 4 for compensation of package or dielectric capacitance cannot be used. Instead the bridge technique described in section 5.6.0.1 and 5.6.0.2 will be used.

	Quartz	GaAs	InP
Piezoelectric constant $\left(\frac{c}{m^2}\right)$	0.173	0.160	0.035

Table 6.1: Piezoelectric constants for quartz, GaAs and InP

6.1.4 Optical measurement for bridges and cantilevers deflection

Using an fabry-perot interferometric design the movement of bridges can be detected. This is done by using the air gap between the bridge and the underlying substrate, which in this case is $4\mu m$, as a reference and measuring the reflected waves off the bridge. An interference will be produced between the reflected waves and the reference. Using this technique deflection changes as low as 1.7 Å has been measured[42].

6.1.5 Optical excitation of III-V MEMS resonators

Using the direct band-gap nature of III-Vs and its piezoelectric nature perhaps the former can be used to drive the mechanical structure into resonance by using the latter. For this to occur the III-V would have to be operating in the depletion mode because this is the piezoelectric region and the charge carriers produced can be swept away from the depletion region. The optical beam used to excite the device into resonance must be chopped at the resonant frequency of the resonator therefore creating charge carriers at this frequency which produces an AC field which can be used to drive the device.

6.1.6 GaAs MEMS resonators

According to table (6.1) GaAs piezoelectric constant is comparable to quartz and is 4.5 times higher than InP. Therefore the charge detected will be 21 times higher than InP. The same ideas of controlling the depletion by creating a heterojunction, optical actuation, fabrication of bridges and cantilevers etc from InP can be transferred to the GaAs.

Appendix A

Depletion Width Calculations

$In_{0.85}Ga_{0.15}P/InP$

$$W = \left[\frac{2\varepsilon_1\varepsilon_2\varepsilon_o\left(\psi_{bi} - V_0\right)}{q\left(\varepsilon_1 N_{d_1} + \varepsilon_2 N_{d_2}\right)}\right]^{1/2}; \psi_{bi} = 4.685 - 4.65 = 0.035\ eV;\ V = 0$$

$$W = \left[\frac{2\left(12.4\right)\left(12.4\right)\left(8.85\times10^{-12}\right)\left(0.035\right)}{\left(1.6\times10^{-19}\right)\left(\left(12.4\right)\left(2.0\times10^{21}\right) + \left(12.4\right)\left(2.0\times10^{21}\right)\right)}\right]^{1/2}$$

$$W = 109.56\,nm \tag{A.1}$$

Surface States

$$W = \left[\frac{2\varepsilon_r\varepsilon_o V}{qN_{d_1}}\right]^{1/2};\ V = \varphi - \left[\frac{E_g}{2q} - \frac{k_B T}{q}\ln\left(\frac{N_{d_1}}{n_i}\right)\right]$$

$$W = \left[\frac{\left(2\right)\left(12.4\right)\left(8.85\times10^{-12}\right)}{1.6e-19}\right]^{1/2}\left(\frac{V}{N_{d_1}}\right)^{1/2}$$

$$V = 0.45 - \left[0.675 - 2.542\times10^{-2}\ln\left(\frac{2.0\times10^{21}}{7.13\times10^{12}}\right)\right]$$

$$V = 0.45 - \left[0.675 - 0.494\right]$$

$$V = 0.45 - 0.181$$

$$V = 0.269$$

$$W = \left[\frac{\left(2\right)\left(12.4\right)\left(8.85\times10^{-12}\right)}{1.6e-19}\right]^{1/2}\left(\frac{0.269}{2.0\times10^{21}}\right)^{1/2}$$

$$W = 429.53\ nm \tag{A.2}$$

Schottky Contact Metal/$In_{0.85}Ga_{0.15}P$

$$W = \left[\frac{2\varepsilon_r\varepsilon_0}{qN_D}\left(\psi_{bi} - V - \frac{kT}{q}\right)\right]^{1/2}$$

$$V_{bi} = \phi_m - \phi_s = 5.1 - 4.685 = 0.415V;\ V = 0$$

$$W = \left[\frac{(2)\,(12.4)\,(8.85e-12)}{(1.6e-19)\,(2.0e21)}\,(0.415 - 0 - 0.025)\right]^{1/2}$$

$$W = 517.20\,nm \tag{A.3}$$

Bibliography

[1] Stephen D. Senturia. *Microsystem Design.* Springer, 2000.

[2] K.E. Petersen. Silicon as a mechanical material. *Proceedings of the IEEE*, 70(5):420–457, 1982.

[3] R. Selvaganapathy. Course notes from Mechanical Engineering 752.

[4] J. Curie, P., Curie. Contractions et dilations produits par des tensions electriques dans les cristeaux hemieedres a faces inclinees, 1881.

[5] R.G. Ballas. *Piezoelectric Multilayer Beam-Bending Actuators (Microtechnology and MEMS).* Springer, 2007.

[6] M.G. Lippman. Principe de la conservation de l'electricite. *Annales de Chime et de Physique*, 5:159, 1881.

[7] Jan Soderkvist. The piezoelectric effect of GaAs used for resonators and resonant sensors. *Components*, 4:28–34, 1994.

[8] Ferdinand Beer, Jr., E. Russell Johnston, and John DeWolf. *Mechanics of Materials.* McGraw-Hill Science/Engineering/Math, 2005.

[9] W. Weaver Jr., S. P. Timoshenko, and D. H. Young. *Vibration Problems in Engineering.* Wiley-Interscience, 1990.

[10] Virgil E Bottom. *Introduction to quartz crystal unit design (Van Nostrand Reinhold electrical/computer science and engineering series).* Van Nostrand Reinhold, 1982.

[11] V. B. Braginsky and V. P. Mitrofanov. *Systems with Small Dissipation.* University Of Chicago Press, 1986.

[12] W. P. Robins. *Phase Noise in Signal Sources(Theory and Application) - IEE Telecommunications Series.* Institution of Engineering and Technology, 1984.

[13] K. L. Ekinci. Ultimate limits to inertial mass sensing based upon nanoelectromechanical systems. *Journal of Applied Physics*, 95(5):2682, 2004.

[14] K. Wang and C.T.-C. Nguyen. High-order micromechanical electronic filters. *Proceedings IEEE The Tenth Annual International Workshop on Micro Electro Mechanical Systems. An Investigation of Micro Structures, Sensors, Actuators, Machines and Robots*, pages 25–30, 1997.

[15] T D Stowe, K Yasumura, T W Kenny, D Botkin, K Wago, and D Rugar. Attonewton force detection using ultrathin silicon cantilevers. *Nanotechnology*, 71(July):288–290, 1997.

[16] M. M. Midzor, P. E. Wigen, D. Pelekhov, W. Chen, P. C. Hammel, and M. L. Roukes. Imaging mechanisms of force detected FMR microscopy. *Journal of Applied Physics*, 87(9):6493, 2000.

[17] J. Brice. Crystals for quartz resonators. *Reviews of Modern Physics*, 57(1):105–146, January 1985.

[18] H. Hida, M. Shikida, K. Fukuzawa, a. Ono, K. Sato, K. Asaumi, and Y. Iriye. Fabrication and characterization of AFM probe with crystal-quartz tuning fork structure. *IEEE International Symposium on Micro-NanoMechatronics and Human Science, 2005*, pages 90–94.

[19] Robert D Grober, Jason Acimovic, Jim Schuck, Dan Hessman, Peter J Kindlemann, Joao Hespanha, and A Stephen Morse. Fundamental limits to force detection using quartz tuning forks. *Review of Scientific Instruments*, 71(7):1–5, 2000.

[20] Dara Bayat, Terunobu Akiyama, Nicolaas F. de Rooij, and Urs Staufer. Dynamic behavior of the tuning fork AFM probe. *Microelectronic Engineering*, 85(5-6):1018–1021, 2008.

[21] K Saitoh, K Hayashi, Y Shibayama, and K Shirahama. A low temperature scanning probe microscope using a quartz tuning fork. *Journal of Physics: Conference Series*, 150(1):012039, 2009.

[22] Yuichi Naitou and Norio Ookubo. High-spatial-resolution scanning capacitance microscope using all-metal probe with quartz tuning fork. *Applied Physics Letters*, 85(11):2131, 2004.

[23] S. Momosaki, E., Kogure. The Application Of Piezoelectricity To Watches. *Ferroelectrics*, 40:203–216, 1982.

[24] David J. Griffiths. *Introduction to Electrodynamics (3rd Edition)*. Benjamin Cummings, 1999.

[25] Henry Ott. *Noise Reduction Techniques in Electronic Systems, 2nd Edition*. Wiley-Interscience, 1988.

[26] Amptek. Charge Sensitive Preamplifier.

[27] T. P. Pearsall. *Properties, Processing and Applications of Indium Phosphide (E M I S Datareviews Series)*. Institution of Electrical Engineers, 2000.

[28] Jean-louis Leclercq, Michel Garrigues, Xavier Letartre, Christian Seassal, and Pierre Viktorovitch. InP-based MOEMS and related topics. *Lightwave*, 10:287–292, 2000.

[29] C Seassal, J L Leclercq, and P Viktorovitch. Fabrication of InP-based freestanding microstructures by selective surface micromachining. 6:261–265, 1996.

[30] G. Rottner K., Helbig R. , And Müller. Piezoelectric resonators of InP. *Applied Physics Letters*, 62:352, 1993.

[31] Sladek R.J. Boyle W.F. Piezoelectric constant and conductivity relaxation in n-type InP from ultrasonic attenuation measurements. *Solid State Communications*, 16(3):323–326, 1975.

[32] D.L. Li, L. Kumar, P., Kanakraju, S., Devoe. Piezoelectric AlGaAs bimorph microactuators. *Journal of Micromechanics and Microengineering*, 16:1062–1066, 2006.

[33] Sotiris C Masmanidis, Rassul B Karabalin, Iwijn De Vlaminck, Gustaaf Borghs, Mark R Freeman, and Michael L Roukes. Multifunctional nanomechanical systems via tunably coupled piezoelectric actuation. *Science (New York, N.Y.)*, 317(5839):780–3, 2007.

[34] Review Article. Gallium arsenide as a mechanical material. 4:1–13, 1994.

[35] FS Hickernell and WR Gayton. Elastic Constants of Single-Crystal Indium Phosphide. *Journal of Applied Physics*, 37:472, 1966.

[36] Simon M. Sze. *Physics of Semiconductor Devices.* Wiley-Interscience, 1981.

[37] M. a. Matin, K. C. Song, B. J. Robinson, J. G. Simmons, and D. a. Thompson. High-responsivity InGaAs/InP-based MSM photodetector operating at 1.3-μm wavelength. *Microwave and Optical Technology Letters*, 12(6):310–313, August 1996.

[38] Shun Lien Chuang. *Physics of Optoelectronic Devices (Wiley Series in Pure and Applied Optics).* Wiley-Interscience, 1995.

[39] Inspec. *Properties of Indium Phosphide.* Institution Of Engineering And Technology, 1991.

[40] Yuhki Imai. Characteristics of InP MIS Schottky Diodes Prepared by Plasma Oxidation. *Journal of The Electrochemical Society*, 129(1):221, 1982.

[41] S. Tiwari, S.L. Wright, and J. Batey. Unpinned GaAs MOS capacitors and transistors. *IEEE Electron Device Letters*, 9(9):488–490, 1988.

[42] D. W. Carr. Fabrication of nanoelectromechanical systems in single crystal silicon using silicon on insulator substrates and electron beam lithography. *Journal of Vacuum Science & Technology B: Microelectronics and Nanometer Structures*, 15(6):2760, November 1997.